FACULTY OF SCIENCE AND TECHNOLOGY

MASTER THESIS

Study programme / specialisation: Petroleum Geosciences Engineering
The spring semester, 2022
Open

Author:

.....
Marta Pernalete

Course coordinator: Alejandro Escalona Varela

Supervisor(s): Aojie Hong and Remus Hanea

Thesis title: Implementation of Adaptive Localization for Enhancing Ensemble-Based History Matching in Hydrocarbon Reservoir Management

Credits (ECTS): 30

Keywords: Ensemble-based history matching, adaptive localization, uncertainty quantification, reservoir management.

Pages: 95

+ appendix: 116

Stavanger, June 15th, 2022

Universitetet i Stavanger

equinor

University of Stavanger

Implementation of Adaptive Localization for Enhancing Ensemble-Based History Matching in Hydrocarbon Reservoir Management

Master's Thesis
In collaboration with Equinor ASA

Industrial Tutor:
Remus Hanea

Academic Tutor:
Aojie Hong

Author:
Marta Pernalete

June 2022

Abstract

In reservoir management, the ensemble-based history matching is applied to quantify and update uncertainty in reservoir characterization with the main objective to support high quality decisions. However, the ensemble-based history matching could suffer from statistical problems that make the ensemble unable to represent probability distributions and quantify uncertainty statistically-correctly. Localization can effectively solve the ensemble-based history matching problems. Localization weights the influence degree that observations have over model parameters in the analysis step of ensemble Kalman filter-based methods. In the non-adaptive localization scheme, the influence degree is fixed in time, and unimodal distributed for all types of observations and model parameters. Unlike the non-adaptive localization scheme, the adaptive localization scheme defines the influence degrees based on causality relationships among simulated observables and model parameters, so that the influence degrees can be time-variant, multimodal distributed, and dependent of reservoir dynamics and different types of model parameters and observations. The thesis lies in the research about the practical advantage of adaptive localization over non-adaptive localization schemes for ensembled-based history matching. The thesis is developed in five sections: i) generation of the initial ensemble; ii) development of an ensemble-based history matching without localization, the benchmark case, that applies ES-MDA; iii) selection of the best non-adaptive localization case, applying distance-based studies; iv) Selection of the best adaptive localization case, applying a denoising approach; and v) Comparative analysis among updated ensembles, defining selection criteria of the best ensemble-based history matching for the Reek field.

The main conclusion from the thesis work is that the history matching with the adaptive localization scheme overperformed the history matching with the non-adaptive localization scheme and the benchmark case (i.e., no localization) for the Reek field. Therefore, adaptive localization scheme can improve uncertainty quantification and decision quality in ensemble-based reservoir management.

The novelty of the thesis is that it has investigated the practical pros and cons of applying the adaptive localization scheme for ensemble-based history matching reservoir simulation models and proposed a general workflow to guide localization implementation and evaluation. The thesis work has brought state-of-the-art and innovative workflows to best practice in Equinor for implementing non-adaptive and adaptive localization schemes. Several guidelines of recommended practice of implementing the workflows have been proposed and developed. The effectiveness of the guidelines and workflows have been tested and evaluated, which contributes to further developing and improving the theories/workflows/guidelines and integrating them in Equinor's existing workflows and software for quantitative and qualitative analysis of history matching results and for facilitating and enhancing the adaptive localization implementation in Equinor and the oil and gas industry.

Preface

The thesis work subject lies in the knowledge gap about the practical pros and cons that adaptive localization scheme has over non-adaptive localization scheme for enhancing ensemble-based history matching. The thesis scope includes the theoretical description and comparison between non-adaptive and adaptive localization schemes, the proposal of a best practice workflow for qualitative and quantitative comparison of the different localization scheme results, and the implementation of this workflow in a synthetic case, Reek field. The proposed workflow develops a benchmark case (i.e., no localization), three non-adaptive localization cases and select the best non-adaptive localization case, three adaptive localization cases and select the best adaptive localization case and, ultimately, performs a comparative analysis among the benchmark case and the best non-adaptive and adaptive cases. The aim of the thesis is to investigate the practical pros and cons of applying the adaptive localization scheme for history matching reservoir simulation models and to propose practical guidelines for implementing the adaptive localization scheme. This thesis is supervised by Professor Aojie Hong at UiS and Remus Hanea in Equinor, and it is submitted to the Faculty of Science and Technology at UiS in partial fulfilment of the requirements for the master's degree in Petroleum Geosciences Engineering, in the spring semester 2022.

The problem statement, its background theories, and the research questions for the thesis are in Chapter 1. Descriptions and theoretical limitations of non-adaptive and adaptive localization schemes are in Chapter 2. The applied methods for ensemble-based history matching with and without localization, the proposed workflow tested in the thesis, and the dataset used for implementing localization are in Chapter 3. The main history matching results, and its analysis and discussions are in Chapter 4. Complementary

history matching result are in the appendixes, which are consistent with the discussions presented in Chapter 4. The discussion with respect to the research questions, conclusions and further work are in Chapter 5. Initial ensemble coverage of observations for all wells and observation types are in Appendix A. The benchmark (i.e., no localization) ensemble coverage of observations for all wells and observation types are on Appendix B. The non-adaptive tapering maps and the non-adaptive localization history matching results for permeability are included in Appendix C. The adaptive localization history matching results for permeability are in Appendix D. The comparative analysis results for permeability and the comparison of ensemble coverage of all updated ensembles for all wells and all types of observations are in Appendix E.

Dedication

To my parents, for loving me unconditionally.

To my sister, for making the path possible.

To my son, for being my lovely source of inspiration.

Acknowledgment

Thank you to my supervisors, Remus Hanea and Aojie Hong, who continuously guided me in this research area. I heartily appreciate their support by providing access to Equinor's applications, dataset, and buildings; introducing excellent professionals for technically support; including me as a member of the research localization team in Equinor; being accessible in weekly follow up meetings, guiding with the structure of the thesis, advising for using time effectively, and helping in this learning process.

Special thanks to Oddvar Olia, Tudor Popa, from Equinor, and Kristian Fossum, from NORCE. Thank you for all the time invested in patiently supporting my learning. Thank you for all the brainstorming sessions to discuss and evaluate guidelines/workflows/results. Sincerely, the thesis would have not been possible without this support.

I would like to thank to Geir Evensen, Xiaodong Luo, Lars Hustoft, Kurt Petvipusit, Kari Bursdal, Camilo Malagon, who contributed with their experience, clearing up the doubts that emerged in my thesis.

Endless gratitude to my family for their constant encouragement and support.

Contents

List of Figures

List of Workflows

1. PROBLEM STATEMENT

1.1. Background overview

1.1.1. Ensemble-based history matching

Ensemble-based history matching brought a different approach to quantify subsurface uncertainties in reservoir engineering to support high-quality decisions. The ensemble-based history matching introduced a probabilistic approach that changed the deterministic paradigm in reservoir characterization, and the manually history matching. The deterministic approach for history matching was based on defining one geological realization as reference or base model, and manually match observations[1]. Then, the manually history matched reference model was used to forecast reservoir performance. The probabilistic approach consists of defining multiple geological realizations for assisting history matching of observations, and then use all these possible geological realizations to predict a probabilistic reservoir performance, quantify subsurface uncertainties and take better supported decisions. The ensemble-based history matching generates a set of multiple geological realizations relying on Monte Carlo simulation for representing probability distributions of model parameters[2].

Chapter 1 will introduce a brief historical review of how ensemble-based history matching started, its definition, motivation, and limitations. The ensemble-based history matching applied in the thesis is the ensemble-smoother with multiple data assimilation (ES-MDA). The description of the ES-MDA scheme is in Chapter 3.

[1] Observations mean the data that are actually measured from the reservoir, e.g., well production rates, well water cuts, well gas-oil ratio, well bottomhole pressure.
[2] Model parameters are uncertain static subsurface properties, e.g., porosity, permeability.

Brief historical review

The ensemble-based history matching method – ensemble Kalman Filter (EnKF) – was developed by Evensen (1994). After that, many variants of the method were proposed, and they (including the original EnKF) where first applied in the atmospheric and oceanographic sciences (Evensen and van Leeuwen, 2000; Houtekamer and Mitchell, 2001; Whitaker and Hamill, 2002; Nævdal et al., 2003; Aanonsen et al., 2009). In these applications, large scale non-linear forward models[3] were used, and only state variables[4] were updated given additional information/data for weather forecasting.

Early applications of the ensemble-based history matching in petroleum reservoir engineering appeared in the 2000s (Nævdal et al., 2003; Evensen et al., 2007), where both model parameters and state variables were updated simultaneously. Nævdal et al. (2003) applied the ensemble Kalman filter (EnKF) for updating dynamic reservoir model state variables (such as pressure and saturations), and static geological model parameters (such as permeability) of a 2D reservoir model. The 2D reservoir model was history-matched to production rates and bottom hole pressure data. Later studies (Gu and Oliver, 2004; Wen and Chen, 2005; Zafari and Reynolds, 2005; Gao et al., 2006) included the update of other types of geological model parameters (such as porosity, fluid contacts, and fault transmissibility) in synthetic models. Bianco et al. (2007), Evensen et al. (2007), and Haugen et al. (2008) presented history matching studies in three real fields located in the west of Africa and in the North Sea, in which EnKF was applied and gave better match of observations and predictive capability of the reservoir models than the obtained by manual history matching. Emerick and Reynolds (2013) compared manually history-matched results with ES-MDA and EnKF ensemble-based history matching results in a

[3] Forward models mean numerical models to calculate predictions, e.g., reservoir numerical simulator.
[4] State variables are uncertain dynamic properties, e.g., fluid saturations, reservoir pressure.

turbidite reservoir located in the Campos Basin, Brazil. Emerick and Reynolds (2013) observed that both ensemble-based history matching methods resulted in significant improvements in the observation matches from the manual history matching results, and generated more realistic geological models with better predictions. These referenced studies demonstrates that the ensemble-based history matching can achieve promising results in synthetic and real cases.

Definition

Ensemble-based history matching is a statistical and Bayesian approach to quantifying and updating uncertainty in reservoir characterization and production forecast when additional information/data (e.g., observations) become available (Zafari and Reynolds, 2005; Chen and Oliver, 2011). Ensemble-based history matching applies Monte Carlo simulation to perform Bayesian inference for updating a prior ensemble of geological realizations that represents the prior uncertainties of model parameters, given new information (Evensen, 2003; Aanonsen et al., 2009). Thus, the output of the ensemble-based history matching is an updated/posterior ensemble of geological realizations that represents the posterior uncertainties of the model parameters.

In general, the ensemble-based history matching consists of three steps (Gu and Oliver, 2004; Evensen et al., 2007; Aanonsen et al., 2009):

I. Initialization step: A prior ensemble is generated from randomly sampling over the probability distributions of the model parameters, given the current knowledge.

II. Forecast step: Forward modelling is then performed on the prior ensemble to simulate observables[5].

III. Analysis step: The model parameters of the prior ensemble are adjusted according to the mismatch between the simulated observables and actual observations. In the history matching context, this mismatch is called innovation. The geological realizations with the adjusted model parameters constitute the posterior ensemble.

Fig. 1 shows a simplified view of the forecast step and the analysis step of the ensemble-based history matching. The forecast step is starting from the prior ensemble (grey squares in the left panel of Fig. 1). The space of simulated observables is generated by numerical simulation (green arrows and dotted line in the left panel of Fig. 1). The analysis step calculates the mismatch (innovation) between the simulated observables and actual observations, and it uses a linear combination scheme to calculate the posterior ensemble. The linear combination scheme will be explained in more details in Chapter 3, section 3.1.

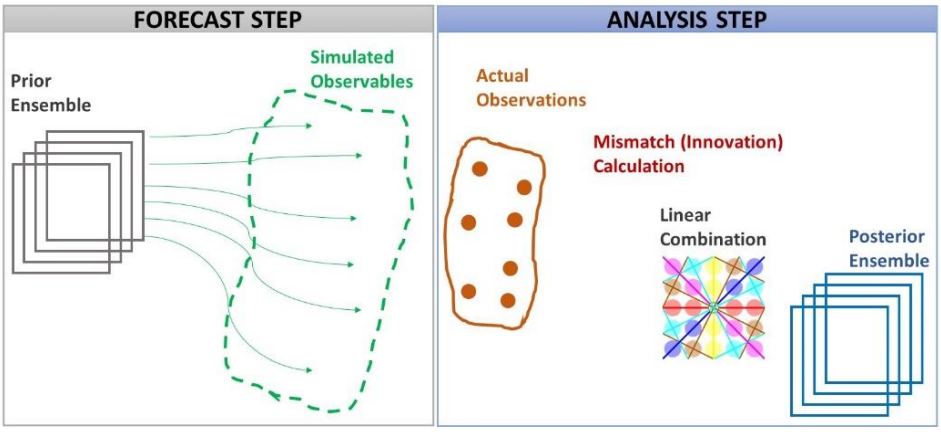

Fig. 1 Simplified view of the forecast and analysis steps in the ensemble-based history matching

[5] Observables are variables than can be observed or measured, e.g., well fluid rates, well water cuts, well gas-oil ratio, well bottomhole pressure. Notice that simulated observables are different from observations. Observations are observables that have been actually observed/measured, whilst simulated observables are calculated using forward modelling.

Motivation and limitations

The ensemble-based history matching has caused a cultural change from using a deterministic reservoir characterization towards a probabilistic reservoir characterization as a result of history matching. The ensemble-based history matching introduced the concept of updating multiple geological realizations to match the observation history. Therefore, ensemble-based history matching allows to quantify uncertainty of the material model parameters[6] to generate probabilistic forecasts; it generates a range of production forecasts that embrace the reservoir characterization uncertainty; and it supports decision makers with a better understanding of possible outcomes. Thus, the main motivation for applying ensemble-based history matching focuses on supporting high-quality decisions that can lead to a greater chance of getting desired outcomes. In addition, ensemble-based history matching allows to combine a non-linear forward model to represent the nonlinearity of reservoir dynamics, with a linear and Gaussian uncertainty updating, while projecting the whole model parameter uncertainty space in the space of the ensemble dimension. Such a combination can significantly mitigate the computational intensiveness for Bayesian updating when a computation demanding forward model is involved. Thus, the ensemble-based history matching is more efficient and assertive for quantifying reservoir characterization uncertainties than the traditional manually history matching, performed by trial and error, in an iterative process, in which the users analyzed the difference between simulated observables and actual observations, chose one or few model parameters to change manually at a time to improve the history matching.

A main limitation of ensemble-based history matching refers to the use of an ensemble with a small number (usually, ≤ 100) of realizations, which brings probability distribution

[6] Material model parameters are those whose different possible values could drive to different decisions.

sampling errors[7], and rank deficiency or insufficient degrees of freedom[8]. These statistical problems can lead to spurious correlation, filter divergence, and/or ensemble collapse; and consequently, an ensemble loses its ability to statistically-correctly represent probability distributions and quantify uncertainty given additional observations (Aanonsen et al., 2009; Emerick and Reynolds, 2010; Sakov and Bertino, 2010; Luo et al., 2019). Spurious correlations are correlations among observations and model parameters that do not have a physical relationship or causation. Spurious correlations make the ensemble diverge, which is known as filter divergence. When ensemble diverges, the ensemble is getting updated wrongly, its uncertainty quantification is not reliable, and could drive to an ensemble collapse (right panel of Fig. 2 shows an illustration of an ensemble collapse). At this point, the posterior model parameter distributions suffer the loss of their variance (σ^2). Consequently, all the realizations give similar value of simulated observables.

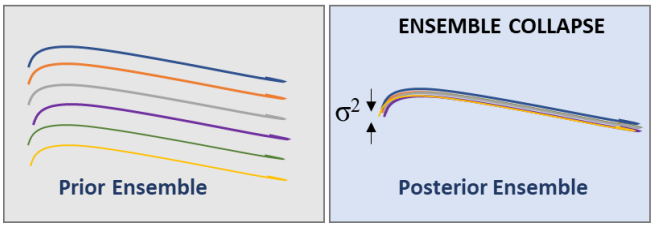

Fig. 2 Illustration of ensemble collapse.

Chen and Oliver (2017) performed ensemble-based history matching in a synthetic 2D water flooding model, and pointed out filter divergence and spurious correlation in an small ensemble when updating the log-permeability field. Chen and Oliver (2017) compared the history matching results between a small and large ensemble. Fig. 3(a)

[7] Sampling errors are statistical errors that occurred when randomly sampling (Monte Carlo) the model parameters distribution with a small ensemble size.
[8] Rank deficiency or insufficient degrees of freedom refers to the inability of a small ensemble to solve the assimilation algorithms for large number of independent data, when they are greater than the number of ensemble members.

shows the truth log-permeability field. Fig. 3(b) and Fig. 3(d) illustrate respectively the ensemble mean and the standard deviation of the log-permeability field obtained with a small ensemble of one hundred members ($N_e = 100$). Fig. 3(c) and Fig. 3(e) display respectively the mean and the standard deviation achieved with a large ensemble of two thousand members ($N_e = 2000$). The scale for the mean of the log-permeability maps is the same. The scales for the standard deviation for the small and large ensembles are different. The scale for the small ensemble, in Fig. 3(d), ranges in the interval (0, 0.04), and the scale in the large ensemble, in Fig. 3(e), ranges in the interval (0, 1.4). The initial ensemble average mean and average standard deviation of the log-permeability are 2.5 and 1.2, respectively (both values highlighted with a dashed line over the respective color scale). The dark grey squares over the log-permeability mean maps in Fig. 3(a), Fig. 3(b), and Fig. 3(c) are used in the thesis for highlighting differences among the Truth model, and the history-matched models from the small and large ensemble.

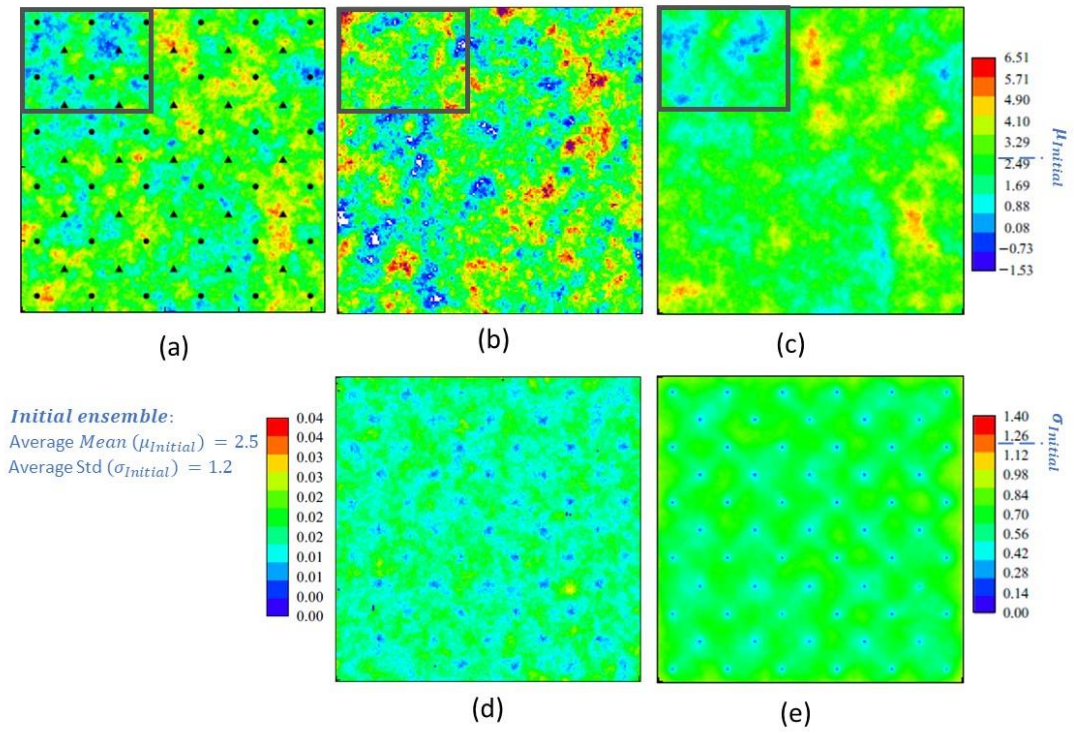

Fig. 3 Example of spurious correlation, filter divergence and ensemble collapse in a synthetic 2D water flooding field, edited from Chen and Oliver (2017).

Chen and Oliver (2017) showed the effect of sampling error and insufficient degree of freedom that a small ensemble suffered and resulted in filter divergence, spurious correlation and tendency to ensemble collapse. In the small ensemble, the log-permeability mean values (Fig. 3(b)) are spatially more heterogenous than the log-permeability mean values of the Truth (Fig. 3(a)). This larger spatial heterogeneity is observed with greater proportion of areas colored in dark red and dark blue in Fig. 3(b) than in Fig. 3(a). Therefore, the resulted small ensemble got updated wrongly, it suffered of filter divergence and spurious correlation. Opposite to the small ensemble, the large ensemble shows log-permeability values colored in lighter red and lighter blue in Fig. 3(c) that represent less spatial heterogeneity, which is more alike to the spatial heterogeneity observed in the Truth model. The dark grey boxes over the log-permeability mean maps (Fig. 3(a), Fig. 3(b), Fig. 3(c)) are useful to highlight the filter divergence and spurious correlation observed in the framed area in the update of log-permeability field by the small ensemble. The filter divergence and spurious correlation in the small ensemble are observed by reddish areas inside the dark grey box in Fig. 3(b) that are not observed inside the dark grey box over the Truth model, Fig. 3(a). These reddish areas in Fig. 3(b) represent high values of log-permeability which are not observed inside the dark grey box over the truth. Opposite to the small ensemble, the large ensemble does not show reddish colors inside the dark grey box in Fig. 3(c) and matches better the log-permeability spatial distribution observed in the Truth model in Fig. 3(a) (notice that the blueish and greenish colors inside the dark grey box are alike between the large ensemble and the truth model). Furthermore, the small ensemble suffered a larger reduction of the ensemble log-permeability standard deviation than the large ensemble did. In Fig. 3(d), the log-permeability standard deviation values range mostly in the interval (0.01, 0.02), and they are significantly smaller than the log-permeability standard deviation values of

the large ensemble in Fig. 3(e), which range mostly in the interval (0.42, 0.84). Chen and Oliver (2017) reported that the average initial ensemble standard deviation was 1.2. In Fig. 3(d), the resulted average standard deviation of the small ensemble can be observed to be approx. 0.017. In Fig. 3(e), the resulted average standard deviation of the large ensemble can be observed to be approx. 0.70. In the small ensemble, the larger reduction of the ensemble log-permeability standard deviation after history matching (from an initial ensemble average of 1.2 to 0.017) means that the small ensemble lost its spread abruptly, and it was tending to ensemble collapse. Unlike the small ensemble, the large ensemble kept the spread of the ensemble after history matching (from an initial ensemble average of 1.2 to 0.70). The example presented by Chen and Oliver (2017) illustrated some of the challenges that ensemble-based history matching experiences when using small ensembles, limiting their effectiveness to quantify the uncertainty in reservoir characterization, to make reliable models, to predict production profiles and consequently, to support high-quality decisions.

1.1.2. Localization Concept

Definition

Localization is an approach for enhancing ensemble-based history matching of large amounts of data. Localization mitigates the ensemble-based history matching problems caused by sampling errors and insufficient degree of freedom of small ensembles. Localization regulates the analysis step during the history matching process by defining the degree of influence that observations have over the update of different model parameters. There are different types of localization schemes to tackle both rank deficiency and sampling errors, such as tapering the Kalman-gain matrix, or splitting observations in groups in order to do local analysis (Sakov and Bertino, 2010; Chen and

Oliver, 2017; Luo et al., 2019). The localization scheme selected and used for this thesis work is the local analysis scheme. Local analysis selects which observations are used and their degree of influence over the model parameters for computing the updated ensemble. Chen and Oliver (2017) explained the local analysis localization concept using a 2D example, illustrated in Fig. 4, where the dots are the location of the observations in the field, the grey square represents the model parameters to be updated in a grid model, and the circle represents the virtual window or region for selecting which observations are considered to have influence on the update of the model parameters in the grey cell. The size of the circle is a user input and is determined based on the user's domain knowledge. Only the observations inside the circle (the red dots) are used for computing the update of the model parameters in the grey cell. The observations outside the circle (the black dots) are not used for updating the model parameters in the grey cell.

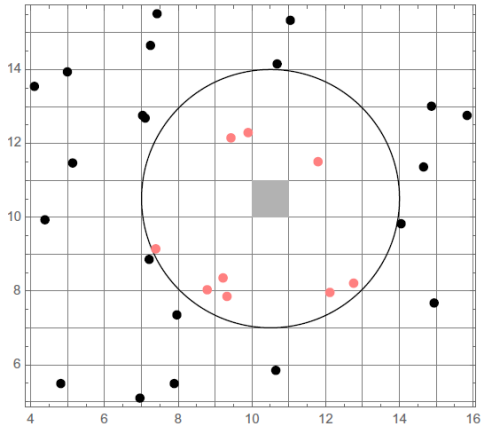

Fig. 4 Local analysis scheme example for performing the update of the model parameters in a single cell from Chen and Oliver (2017).

In addition, localization can weight gradually the influence degree that observations have over the update of model parameters inside the virtual window or defined region. Therefore, some observations could have stronger influence than others inside the circle. Fig. 5, right panel, shows a circle (virtual window) around well P28 painted with a color scale. This color scale illustrates a gradual decrease of influence that observations have

for the update of model parameters in the grid cell where well P28 stands. Observations that are in the red-reddish area have stronger influence, those in the yellowish-greenish area have moderate influence, those found in blueish area have week influence, and finally, those observations in the white area of the 2D space in Fig. 5, right panel, which are out of the critical radius defined by the virtual window, do not have any influence over the update of the model parameters in the grid cell where well P28 exists.

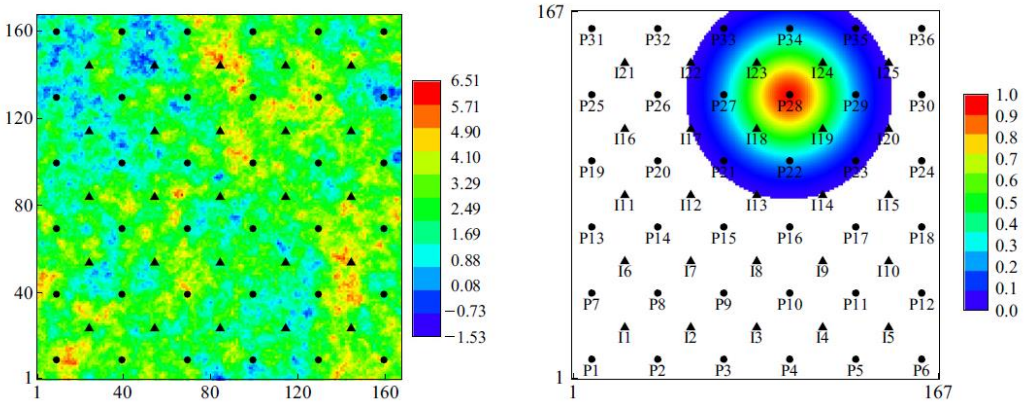

Fig. 5 Local analysis example of observation selection and their influence degree (tapering function) over model parameters update from Chen and Oliver (2017).

Localization can effectively eliminate unrealistic correlations over long-distance by reducing the amount of data used for history matching at a specific location. As a result, localization solves the ensemble-based history matching problems or limitations: spurious correlation, filter divergence and ensemble collapse (Aanonsen et al., 2009; Emerick and Reynolds, 2010; Sakov and Bertino, 2010; Luo et al., 2019).

Non-adaptive and adaptive localization brief overview

The influence degree that observations have over model parameters updates could be defined either based on a non-adaptive or adaptive localization scheme. The traditional localization scheme for history matching has been non-adaptive, which defines the influence degree of observations over model parameters update based on the physical

distance between observations and the model parameters coordinates in the geological model space. In the non-adaptive localization scheme, the influence degree relations among observations and model parameters are fixed in time, and are independent of the type of observations or model parameters that are related to each other during the analysis step (Sakov and Bertino, 2010; Chen and Oliver, 2017; Silva Neto et al., 2021). Unlike the non-adaptive localization scheme, the adaptive localization scheme defines the influence degree of observations over model parameters based on causality relations among them, which are represented by correlation coefficients that are calculated based on reservoir simulation results. Model parameters and simulated observables that have stronger dynamic causality in reservoir simulation generate stronger correlation coefficients among the corresponding model parameters and observations (Emerick and Reynolds, 2010; Luo and Bhakta, 2019; Luo et al., 2019; Silva Neto et al., 2021). The correlation coefficients that relate observations and model parameters in the adaptive localization scheme can change over time when reservoir dynamics changes, and the correlation coefficients can be different for different types of observations and model parameters.

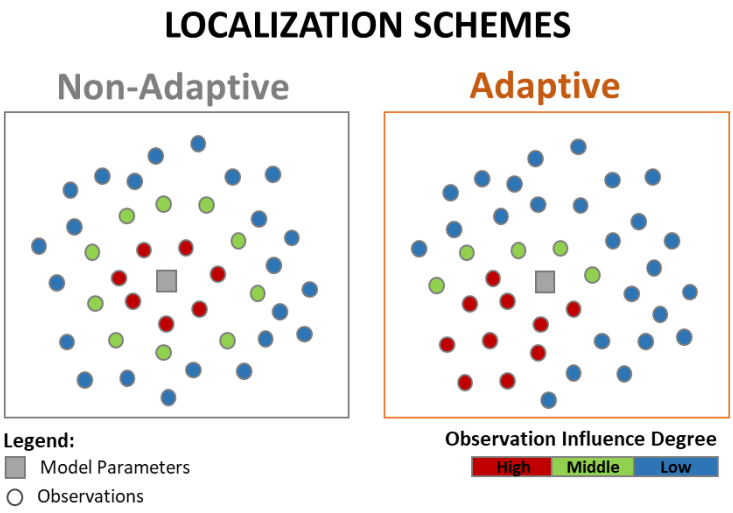

Fig. 6 Non-adaptive and adaptive localization scheme illustration, highlighting different influence degrees of the same set of observations over model parameters in the grey cell.

Fig. 6 illustrates the differences between non-adaptive and adaptive localization schemes regarding the influence degree of the same set of observations over the update of model parameters located in the grey cell. The non-adaptive localization scheme is distance or region based. Thus, it assigns stronger influence degrees to those observations that are closer to the grey cell (left panel in Fig. 6). In contrast, the adaptive localization scheme is reservoir dynamics correlation based. Therefore, the correlation coefficients among observations and model parameters to govern the analysis step is defined based on the reservoir dynamics causation among model parameters and simulated observables. This means that closer observations to the grey cell can have weaker influence degrees that farther observations, depending on correlations among observations and model parameters (right panel in Fig. 6). The adaptive localization scheme selects only those observations that have stronger causal relationships, based on reservoir dynamics, with the model parameters to be updated in the analysis step.

Further localization scheme discussions and descriptions are in Chapter 2 and Chapter 3, respectively.

1.2. Knowledge gap

The knowledge gap of the study lies in the research about the practical advantage of adaptive localization over non-adaptive localization schemes for ensembled-based history matching. Theoretically, adaptive localization schemes should be more representable of the reservoir dynamics and its heterogeneities. However, their applications have not been extensively tested in different settings to conclude their practical advantage over the non-adaptive localization schemes.

1.3. Aim of the study

The aim of the thesis is to investigate the practical pros and cons of applying the adaptive localization scheme for history matching reservoir simulation models, and to propose practical guidelines for implementing the adaptive localization scheme. The thesis applies the ensemble-based history matching study in a synthetic field, Reek field, which is described later in Chapter 3, section 3.6.

1.4. Research questions

The thesis will answer the following research questions:

- Does the application of localization techniques achieve a better history matching than the case without applying any localization technique in ensemble-based history matching, for the Reek Field?
- Does the adaptive localization scheme enhance history matching over the non-adaptive localization scheme for the Reek Field?
- What are the advantages and limitations of using non-adaptive and adaptive localization schemes in practice?
- What are the recommended practices of implementing non-adaptive and adaptive localization schemes?

2. LOCALIZATION SCHEME DISCUSSION

Localization is an approach for addressing the challenges in the ensemble-based history matching. In Chapter 1, the definition of localization is in section 1.1.2., and the ensemble-based history matching limitations or challenges are in section 1.1.1. There are two common localization methods being applied in reservoir engineering, Kalman-gain or covariance localization and local analysis. Both methods use tapering coefficients[9] to perform the Schur product[10] of the Kalman Gain ensemble matrix and regulate the updating of the model parameters. The covariance localization regulates the analysis step globally, by multiplying the Kalman gain matrix elementwise by a distance-based correlation matrix (matrix with all the tapering coefficients) to generate a localized covariance estimate (Aanonsen et al., 2009; Sakov and Bertino, 2010; Chen and Oliver, 2017). The local analysis decomposes a reservoir model into several local domains so that the model parameter update of each domain is performed by selecting observations within a critical distance or region from the model parameters, and by weighting the influence degree of those observations with tapering coefficients (Aanonsen et al., 2009; Sakov and Bertino, 2010; Chen and Oliver, 2017). The Kalman-gain or covariance localization method is beyond the scope of this thesis. The thesis applies localization with the local analysis method, which is referred to as the non-adaptive localization scheme in the rest of the thesis.

[9] Tapering coefficients are scaling coefficients to weighting the degree of influence that observations have over a space of model parameters in the analysis step. The tapering coefficients can follow a hard rule, ranging in the discrete interval {0,1}, or they can follow a smooth rule, ranging in the continuous interval [0, 1]. Strong influence degrees are represented by coefficient's values near or equal to one (1). Week influence degrees are represented by coefficient's values near or equal to zero (0).

[10] The Schur product is an elementwise product of matrices. Operation that takes two matrices of the same dimension to produce a matrix of the same dimension, where each resulted element i,j is the product of element i,j of the original two matrices.

The rest of Chapter 2 will discuss the main features and limitations of the non-adaptive and adaptive localization schemes. The detailed description of the ensemble-based history matching method (ES-MDA), the non-adaptive and adaptive localization schemes applied in the thesis are in Chapter 3.

2.1. Non-adaptive localization scheme

Main features

The non-adaptive localization scheme is the most adopted scheme for ensemble-based history matching, and many studies have demonstrated the benefit of using the non-adaptive localization scheme over the history matching without localization (Emerick and Reynolds, 2010; Sakov and Bertino, 2010; Chen and Oliver, 2013, 2017; Luo et al., 2017, 2019; Luo and Bhakta, 2019; Silva Neto et al., 2021). However, there are limitations of using the non-adaptive localization scheme, as will be discussed later. The non-adaptive localization scheme is a distance-based or region-based scheme to define the influence of observations over model parameter updates. The region-based localization scheme consists of defining polygons in the space of the reservoir model and governing the update of the model parameters inside each polygon with the observations physically located in the polygon. The influence degree of an observation/datum over model parameters can be represented with a value equal to either one (1) or to zero (0), which is called in the rest of the thesis as discrete tapering coefficients. If the observation is taken in the update, then the influence degree is one (1). Otherwise, the influence degree is zero (0), which means that the observation is not taken in the update of those model parameters. The non-adaptive localization scheme can also apply continuous tapering coefficients to define smooth influence degrees (values from 0 to 1 instead of either 0 or 1) of observations over model parameters. Either the discrete or continuous tapering coefficients are computed

based on the physical closeness between an observation and a model parameter in the geological models. Therefore, closer observations to a model parameter have stronger influence on the model parameter than farther observations. The influence degree of observations over model parameters can be defined with discrete or continuous tapering coefficients. Unimodal tapering functions[11] are commonly used to govern the observations influence degrees over model parameters, when choosing continuous tapering coefficients in the non-adaptive localization scheme.

Luo et al. (2019) showed an example of a distance-based unimodal tapering coefficients for the observations in the well B-2H in the Norne Field (Fig. 7). Luo et al. (2019) introduced a yellow to blue color scale to illustrate B-2H observations influence degrees over model parameters updates in the Norne Field. In Fig. 7, the yellowish color represents the area where B-2H observations have stronger influence degrees, smoothly reducing to weaker influence degrees farther from B-2H towards the blueish area. The non-adaptive localization schemes are characterized by setting the same tapering coefficients in the space and time domain for each type of observations over each type of model parameters during history matching. Thus, the unimodal tapering coefficients map that is illustrated in Fig. 7 was kept fixed for all types of observations in B-2H (water, gas and oil production rates) over the update of model parameters (porosities and permeabilities) in Layer 10 of the Norne Field during the nine years of history matching performed by Luo et al. (2019).

[11] "Unimodal tapering functions" refers to the functions that generate continuous tapering coefficients that decreases smoothly and continuously from the physical location of the observations.

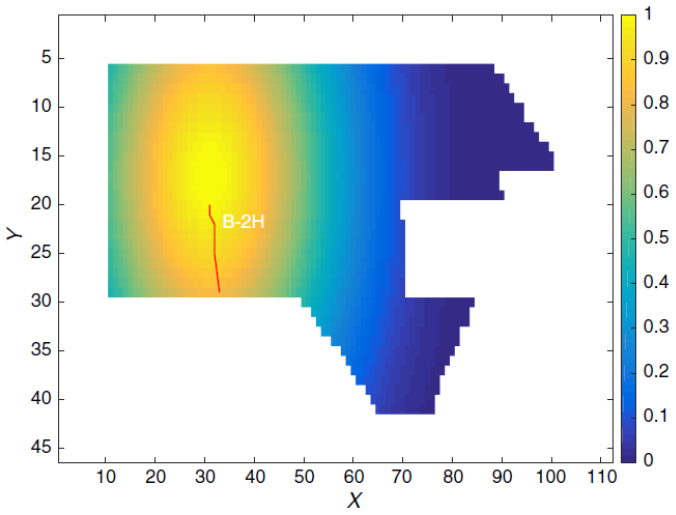

Fig. 7 Unimodal tapering function for non-adaptive localization scheme in the Norne field from Luo et al. (2019).

Limitations

Luo and Bhakta (2019) summarized the non-adaptive localization scheme shortcomings for history matching. A major drawback occurs when it is needed to handle non-local observations which are observations that are not linked to a physical coordinate in the 3D geological model space (e.g., leading wavelet coefficients of 4D-seismic data (Luo et al., 2017), because the non-adaptive localization scheme depends on the availability of physical locations for both the observations and the model parameters. Additionally, the non-adaptive localization scheme does not consider that the observations influence degrees over model parameters may change over time due to reservoir dynamic changes through production life. Furthermore, the non-adaptive localization scheme does not consider different influence degrees among observations and model parameter types. Therefore, the same tapering coefficients maps are applied to all type of observations which share the same physical location in the 3D geological model space to govern the update of model parameters. In addition, another limitation of the non-adaptive localization scheme refers to unimodal distributed tapering coefficients which update model parameters based on distance instead of reservoir dynamics relations among observations and model parameters.

2.2. Adaptive localization scheme

Main features

The adaptive localization scheme is designed to mitigate the limitations of the non-adaptive localization that is based on distance or regions. The first attempts for adaptive localization schemes were based on streamlines (Arroyo-Negrete et al., 2008) or drainage areas (Emerick and Reynolds, 2010). These attempts considered reservoir dynamics (streamlines or drainage radius) to define the influence degree regions of well observations over model parameters, but the localization scheme still depended on physical location of observations and model parameters; the tapering coefficients maps were unimodal distributed, did not change over time during history matching, and did not consider different physical relations among observation and model parameter types. Luo et al. (2019) introduced an adaptive localization scheme based on correlation coefficients among model parameters and the simulated observables. The adaptive localization scheme introduced by Luo et al. (2019) held the principle that if an simulated observable showed a physical causal relation with a specific model parameter, then the observation needed to be used in that model parameter update. Otherwise, that observation should not be considered in the update of the specific model parameter. The physical causal relation is quantified in term of the magnitude of the correlation coefficient between a model parameter and a simulated observable because the correlation coefficient is related to the physics modelled in the reservoir simulation model. The correlation coefficients can have multimodal[12] distribution, can be sensitive to different physical relations among observation and model parameter types, and can vary in the time domain. Fig. 8 and Fig.

[12] The term of multimodal distributions means that the correlation coefficients between model parameters and simulated observables could have different spatial trends based on the physical causality among model parameters and simulated observables, modelled with reservoir simulation.

9 illustrate different correlation coefficients maps of the adaptive localization scheme (Luo et al., 2019).

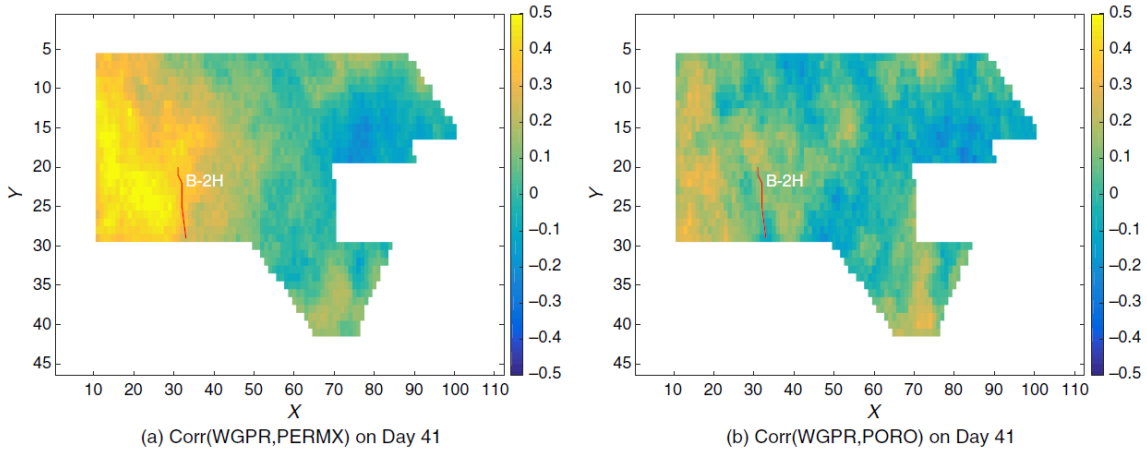

Fig. 8 Correlation coefficients between B-2H gas production rate (WGPR) and two model parameters, permeability (PERMX) and porosity (PORO) in the Norne field study on Day 41 of reservoir simulation, from Luo et al. (2019).

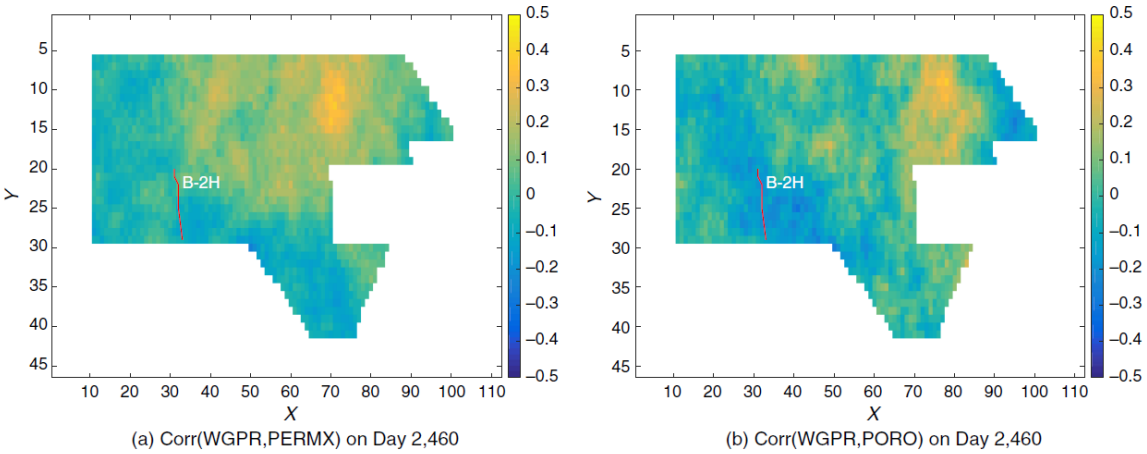

Fig. 9 Correlation coefficients between B-2H gas production rate (WGPR) and two model parameters, permeability (PERMX) and porosity (PORO) in the Norne field study on Day 2,460 of reservoir simulation, from Luo et al. (2019).

Fig. 8 shows different correlation coefficients maps among gas production rates and two different model parameters, permeability (PERMX) and porosity (PORO) at Day 41 of reservoir simulation. The differences in the correlation coefficients maps between Fig. 8(a) and Fig. 8(b) demonstrate that the adaptive localization scheme can provide different correlation coefficients among different type of observations and model parameters. In addition, Fig. 9 shows the correlation coefficients between gas production rates and the

same two model parameters (permeability and porosity) at a different date than Fig. 8, Day 2,460. The correlation coefficients in Fig. 8 are different than those in Fig. 9. The adaptive localization scheme can define different correlation coefficients maps based on the physical causation relation among model parameters and simulated observables at different times.

The adaptive localization scheme introduced by Luo at al. (2019) defined observations influence degrees over model parameters with discrete tapering coefficients[13]. The adaptive localization calculates tapering coefficients to regulate the history matching update based on correlation coefficients among model parameters and simulated observables, and it applies a positive correlation-threshold value. The adaptive localization scheme introduced by Luo at al. (2019) proposed that if the absolution value of the correlation coefficient between a simulated observable and a model parameter was greater than the correlation-threshold value, the tapering coefficient had a value of one (1), and then the observation was taken for updating the model parameter. Otherwise, the tapering coefficient had a value of zero (0), and the observation was excluded during the history matching. The application of positive correlation-threshold values allows to only include the observations that have strong causal relations with the model parameters, in history matching.

The adaptive localization explained by Luo and Bhakta (2019) identified two problems in the adaptive localization scheme introduced by Luo at al. (2019) and proposed an alternative method to compute a positive correlation-threshold value. The two problems identified by Luo and Bhakta (2019) were, first, the application of a user-defined

[13] Discrete tapering coefficient means that the tapering coefficient only can have the value of either zero (0) or one (1).

(empirical) tuning factor to compensate the assumption that sampling errors in the correlation fields were white Gaussian noise[14]; and second, the application of discrete tapering coefficient to update model parameters that may induce discontinuities in the updated geological realizations, and could neglect some observations that may be slightly lower than the positive correlation-threshold value, but may have still-influential degree in the model updates. Luo and Bhakta (2019) proposed a more efficient workflow for the estimation of noise levels that were used for computing a positive correlation-threshold value, and the application of a continuous tapering rule for defining the tapering coefficients that govern the model parameter's updates.

Furthermore, as the adaptive localization scheme introduced by Luo at al. (2019) and Luo and Bhakta (2019) were based on the magnitudes of correlation coefficients instead of being based on the magnitudes of physical distances between observations and model parameters, the adaptive localization scheme allows to handle non-local observations, which can be available in seismic data history matching problems (e.g., leading wavelet coefficients of 4D-seismic data (Luo et al., 2017)). However, in the case study of this thesis, only the observations with a physical location (e.g., well water cut, well gas-oil ratio, well block average pressure) are considered.

Limitations

The discrete tapering coefficients maps proposed by Luo at al. (2019) could have isolated speckles depending on the way how the tapering coefficients were calculated from the correlation coefficients and the correlation-threshold value, which could make the tapering coefficient maps to look discontinuous in space. Fig. 10 illustrates the tapering

[14] White Gaussian noise means that the sampling errors are assumed to have a zero-mean normal distribution with variance or noise, S, ($N(0, S)$).

coefficients for B-2H gas production over permeability and porosity (the left and right panel in Fig. 10, respectively) on simulated Day 41. The illustrated tapering coefficients are chosen from the discrete interval {0,1}. There are examples of isolated speckles in Fig. 10(a), where yellow-colored gridcells are isolated within the blue area. Fig. 10(b) illustrates the lack of transitions or smoothness among blue-colored and yellow-colored gridcells in the model space due to discrete tapering coefficients. The use of discrete or discontinuous tapering coefficients could make abrupt model parameters update in space, generating that the reservoirs models in the ensemble could lose the representable geological continuities.

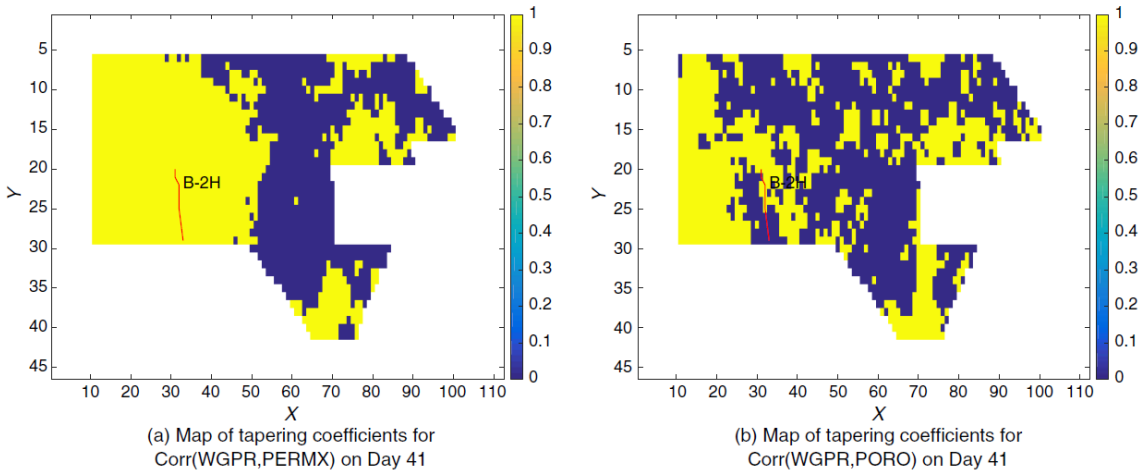

Fig. 10 Tapering coefficients calculated from the correlation coefficients in the Norne Field by Luo et al. (2019)

Furthermore, the adaptive localization scheme could be more computational demanding than the non-adaptive localization scheme because of additional computations required for calculating the correlation coefficients among model parameters and simulated observables.

3. METHODS AND DATA

3.1. Ensemble smother with multiple data assimilation

The ensemble smoother with multiple data assimilation (ES-MDA) is an iterative ensemble-based method that consists of performing the assisted history matching (AHM) multiple times (user-defined number of iterations), with the same set of observations, for gradually control the changes in the model parameters during history matching. ES-MDA makes smaller changes in the model parameters at early iterations and then gradually makes larger changes in the model parameters at later iterations. The motivation of applying the ES-MDA lies in its advantages over other ensembled-based history matching methods used in reservoir engineering, e.g., ensemble Kalman filter (EnKF) (Aanonsen et al., 2009) and ensemble smoother (ES) (Skjervheim et al., 2011). ES-MDA performs better than EnKF and ES in highly non-linear systems: ES-MDA achieves better data matches, more reliable uncertainty quantification of model parameters and production forecasts, and it runs with comparable computational costs (Gu and Oliver, 2007; Emerick and Reynolds, 2012, 2013). In the ES-MDA, the spread of the observation error's covariance is increased gradually with inflating factors over each iteration. The sum of the inversed inflating factors used in each ES-MDA iteration is equal to 1, Equation (*2*). Emerick and Reynolds (2013) introduced the algorithms to perform the three history matching steps (initialization, forecast and analysis) in the ES-MDA, which are summarized in Workflow 1.

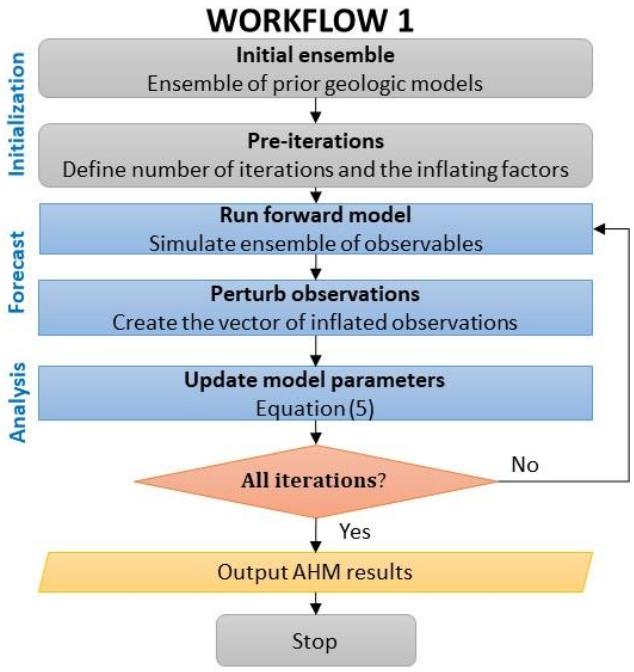

Workflow 1 Perform ensemble-based history matching with ES-MDA

The details in each history matching steps (initialization, forecast and analysis) are described as follows:

Initialization step:

- **Initial ensemble:** Sample N_e members from the prior distributions of the uncertain model parameters (m) of the reservoir dynamic system,

$$\{m_n^0\}_{n=1}^{N_e} \quad (1)$$

where subscript, n , denotes the index of an ensemble member that ranges from 1 to N_e, and the superscript, 0, indicates that the ensemble of model parameters is the initial ensemble, based on prior knowledge.

- **Pre-set iterations:** Define the number of iterations, N_a, and the inflating factors α_{l+1} for $l = 0,1, \ldots, N_a - 1$ to be used in each iteration. The values of α_{l+1} are commonly defined as decreasing with l, and they must satisfy the following condition

$$\sum_{l=0}^{N_a-1} \frac{1}{\alpha_{l+1}} = 1 \quad (2)$$

Forecast step:

FOR $l = 0$ to $N_a - 1$ ($l = 0$ indicates that the forecast step in the first iteration is starting from the initial ensemble. Consequently, the forecast step in the last iteration, N_a, starts with the ensemble corresponding to $l = N_a - 1$)

- **Run forward model:** Simulate the vector of observables, d_n^l , by running the forward model (i.e., a numerical reservoir simulator, Eclipse in this thesis) for the entire time of observations,

$$d_n^l = g(m_n^l), \text{ for } n = 1,2, \dots, N_e, \quad (3)$$

  where $g(\cdot)$ represents the forward or simulation model, and d_n^l is the vector of simulated observables throughout the observation history, containing the observables simulated with the model parameters m_n^l.

- **Observation perturbation:** Create the vector of inflated observations $d_{uc,n}^l$, based on the vector of actual observations d_{obs}, the covariance matrix of observation measurement errors C_D, and the inflating factors α_{l+1}, using

$$d_{uc,n}^l = d_{obs} + \sqrt{\alpha_{l+1}} {C_D}^{1/2} z_d, \text{ for } n = 1,2, \dots, N_e; \quad (4)$$

  where z_d is a vector of random values generated from the normal distribution, $N(0, I_{N_d})$, with I_{N_d} being the identity matrix of size equal to the total number of actual observations in the entire history (N_d).

Analysis step:

- **Analysis step:** Update the model parameter vector using the linear combination calculated in the following equation,

$$m_n^{l+1} = m_n^l + C_{MD}^l \left(C_{DD}^l + \alpha_{l+1} C_D\right)^{-1} \left(d_{uc,n}^l - d_n^l\right), \text{ for } n = 1,2,\dots,N_e; \quad (5)$$

  where C_{MD}^l is the cross-covariance matrix between model parameters and simulated observables, C_{DD}^l is the auto-covariance matrix of simulated observables. Both covariance matrices C_{MD}^l and C_{DD}^l are calculated for each iteration in the same way as the ensemble smoother (ES) is used, based on the ensemble $\{m_n^l, d_n^l\}_{n=1}^{N_e}$ (Skjervheim et al., 2011).

END FOR $l = 0$ to $N_a - 1$ (history matching loop is repeated for N_a number of iterations).

In the thesis, the number of iterations $N_a = 3$, and the inflating factors, $\alpha_{l+1} = 7, 3.5, 1.75$ for $l = 0,1,2$, respectively, are used.

3.2. Localization in ensemble smoother with data assimilation

Luo et al. (2019) explained that the role of localization was to modify the degree of the observation's influence on model parameters. The way how localization modifies the analysis step is summarized as followed:

- In the analysis step of ES-MDA history matching, the updated model parameters are calculated using Equation (5) for $n = 1,2,\dots,N_e$, and for $l = 0,1,\dots,N_a - 1$.

- Equation (5) can be re-expressed using Equation (6) and Equation (7) to ease later discussions.

$$K^l = C_{MD}^l \left(C_{DD}^l + \alpha_{l+1} C_D\right)^{-1}, \quad (6)$$

where K^l is a Kalman-gain-like matrix in iteration *l*,

$$\Delta d^l = \left(d_{uc,n}^l - d_n^l\right), \quad (7)$$

where Δd^l is the innovation with respect to the prior m_n^l,

$$m_n^{l+1} = m_n^l + K^l \Delta d^l \quad (8)$$

- Let $m_{p,n}^{l+1}$ stands for the *p*th model parameter variable (p = 1, 2, …, m) of the updated model vector m_n^{l+1}. In the same way, $m_{p,n}^l$ represents the *p*th model parameter variable (p = 1, 2, …, m) of the prior model vector m_n^l. Then, Equation (8) can be re-write as:

$$m_{p,n}^{l+1} = m_{p,n}^l + \sum_{s=1}^{N_d} K_{ps}^l \Delta d_s^l, \quad (9)$$

where K_{ps}^l denotes the element of K^l at the *p*th row and *s*th column, and Δd_s^l is the *s*th element of Δd^l, for the observations s = 1, 2, …, N_d.

- Equation (9) implies that each innovation element, Δd_s^l, contributes to the update of the *p*th model parameter , $m_{p,n}^{l+1}$, and the degree of contribution is governed by the element of the Kalman-gain-like matrix, K_{ps}^l.
- Localization modifies the degree of influence that each innovation element, Δd_s^l, has over the update of the *p*th model parameter, $m_{p,n}^{l+1}$, by introducing scalar coefficients,

$c_{ps} \in [0,1]$ that multiplies the element of the Kalman-gain-like matrix, K_{ps}^{l}. Then, the analysis step equation with localization can be expressed as:

$$m_{p,n}^{l+1} = m_{p,n}^{l} + \sum_{s=1}^{N_d} (c_{ps} K_{ps}^{l}) \Delta d_s^{l}, \quad (10)$$

where $(c_{ps} K_{ps}^{l})$ represents the element-wise product (Schur product) that weights the degree of influence that observations have over model parameters.

The inclusion of localization in the ES-MDA only modifies the analysis step of the ensemble-based history matching. The workflow to perform ES-MDA with localization is summarized in Workflow 2. The difference between Workflow 1 and Workflow 2 is the equation used in the analysis step. Equation (10) requires the definition of the tapering coefficients, c_{ps}, to perform the update of the model parameters $m_{p,n}^{l+1}$. The following sections will include the equations to compute the tapering coefficients for field and free parameters[15], and for non-adaptive and adaptive localization schemes.

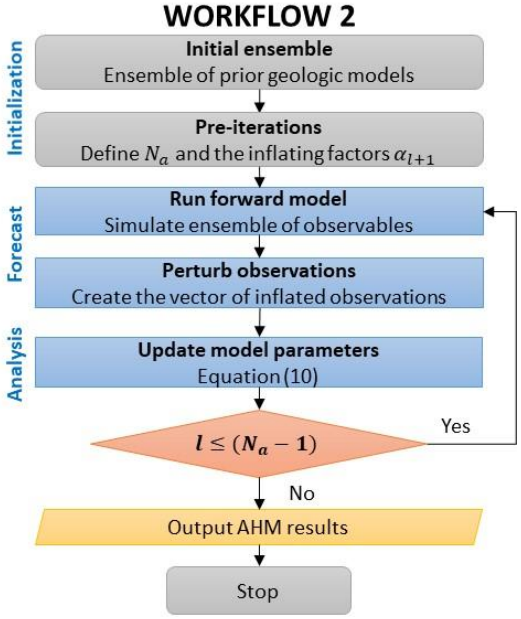

Workflow 2 Perform ensemble-based history matching with ES-MDA and localization

[15] Field parameters are model parameters with a coordinate location, e.g., porosity, permeabilities. Free parameters are those without a coordinate location, e.g., fault multipliers, relative permeabilities.

3.3. Tapering coefficients in non-adaptive localization scheme

The non-adaptive localization scheme is distance or region based as explained in Chapter 1 and Chapter 2. The non-adaptive localization method presented by Luo et al. (2019) consists of defining the tapering coefficients, c_{ps}, in Equation (10) as a function of the distance between the location of model parameters and observations. Luo et al. (2019) exemplified the distanced-based tapering coefficients computation by considering a 2D layered-reservoir model, a model parameter element located in the 2D cartesian coordinate $A = (x_A, y_A)$ and an observation located in the 2D cartesian coordinate $B = (x_B, y_B)$, then the distance-based tapering coefficients can be computed by:

$$c_{ps} = f\left[\widetilde{dist}^{*}(A, B)\right], \quad (11)$$

where $f(\cdot)$ is a tapering function that exits in the positive real values domain, ranging in the interval [0, 1]; $\widetilde{dist}^{*}(A, B)$ is the physical horizontal distance between A and B in the reservoir model. In addition, Luo et al. (2019) explained that in practical implementation of distanced-based localization, an elliptical region is used for representing the influence area that observations have over model parameters instead of a circular region. The elliptical regions allow to extend localization regions based on reservoir anisotropies. Emerick and Reynolds (2010) illustrated an elliptical influence region with an internal color scale, calculated by applying a tapering function based on Gaspari and Cohn (1999) to compute the tapering coefficients, c_{ps}, in Fig. 11. Furthermore, Emerick and Reynolds (2010) introduced different methods that have been implemented to define the influence regions among observations and model parameters, such as the studies developed by Devegowda et al (2007) and Arroyo-Negrete et al. (2008), which used streamlines to define the influence regions and the tapering coefficients, c_{ps}. Arroyo-Negrete et al.

(2008) performed a covariance localization with EnKF in a nine-spot waterflooding reservoir model. Arroyo-Negrete et al. (2008) defined the observations-model parameters influencing areas by taking all the gridblocks crossed by streamlines from injectors to each producer. Fig. 12 shows all the gridblocks crossed by streamlines arriving at the producer P8. Left and center panel in Fig. 12, show ensemble member 15 and 73, respectively. The right panel in Fig. 12 shows the region resulted after stacking all the ensemble members. The resulted region (right panel in Fig. 12) became to be the influencing area that observations located in P8 coordinates has over model parameters. In the study presented by Arroyo-Negrete et al. (2008) the use of streamline defined the gridblocks of the entire-ensemble that were included in the cross-covariance calculation, and the tapering coefficient, c_{ps}, ranged in the discrete interval [0,1].

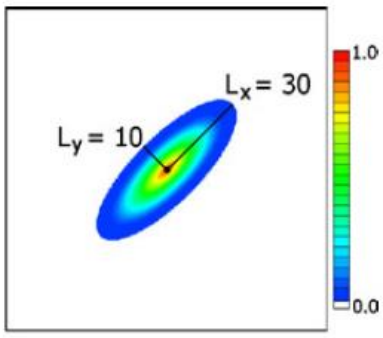

Fig. 11 Illustration of elliptical influence area among an observation element and the model parameters in the analysis step (from (Emerick and Reynolds, 2010))

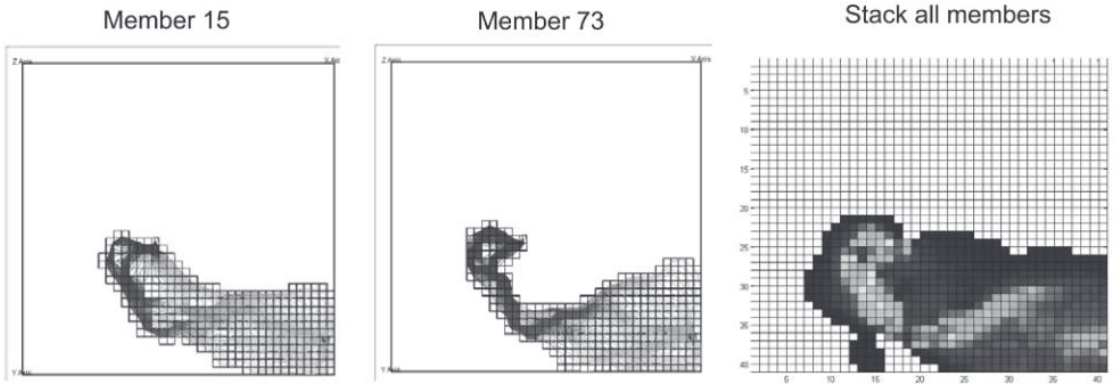

Fig. 12 Example of observation influence region defined by streamline simulation in a waterflood reservoir model (from (Arroyo-Negrete et al., 2008))

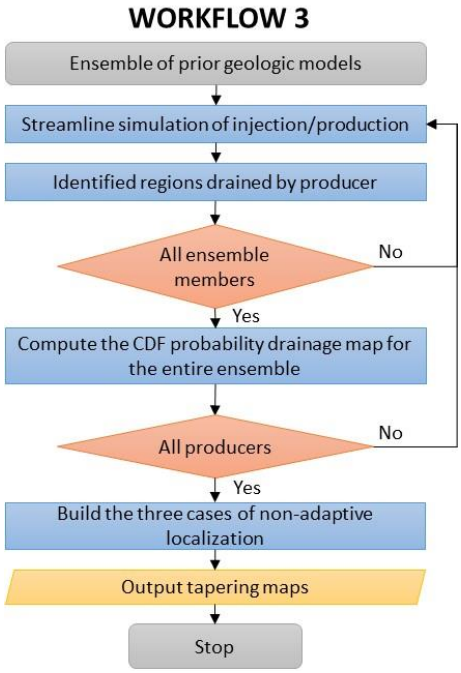

Workflow 3 Define the tapering coefficients in the non-adaptive localization scheme.

In this thesis, the implemented method to compute the tapering coefficients in the non-adaptive localization scheme is based on the introduced studies of Devegowda et al.(2007), Arroyo-Negrete et al.(2008), Emerick and Reynolds (2010), and Luo et al. (2019). The process used to define the non-adaptive localization regions and the tapering coefficients is summarized in Workflow 3. The streamline simulation is run for every ensemble member, considering all the injectors active and one producer active at a time. The streamline simulation identifies all the gridblocks that are drained by the active producer in each ensemble member. Then, the results of all the ensemble members are outlined in a drainage probability map for the active producer, using cumulative distribution function (CDF) in each gridblock. The drainage probability map for the active producer has a value in each gridblock that ranges in a continuous interval [0,1], and this value represents the probability that the gridblock is drained by the active producer. The mentioned steps of Workflow 3 are repeated for all the producer wells to generate the

non-adaptive tapering coefficient maps for each producer well. In this thesis, three non-adaptive cases are defined based on different tapering maps, as followed:

I. Non_adapt_00 case: This case includes the CDF probability drainage maps computed with Workflow 3 for each producer. In these tapering maps, all gridblocks that have a probability to be drained larger than zero will be taking as part of the influence area for all observations in the specified well location, and the tapering coefficients, c_{ps}, are equal to the CDF value in each gridblock.

II. Non_adapt_50 case: This case applies a cut off to the CDF probability drainage maps computed with Workflow 3 for each producer. The tapering maps in the non_adapt_50 case only include the gridblocks that have a CDF probability of being drained equal or larger than 50%. In this case, the tapering coefficients, c_{ps}, are equal to the tapering coefficients in non_adapt_00 case where the gridblocks have a CDF probability of being drained equal or larger than 50%. Otherwise, the tapering coefficients are equal to zero. However, smoothing (weighted averaging) technique is performed with the geomodelling software (RMS) to solve abrupt changes of the tapering maps in the nearest gridblocks where the tapering coefficients change from being equal to the CDF probability (when the CDF probability of being drained is equal or larger than 50%) to zero (when the CDF probability of being drained is less than 50%), (Nagle, 2010; von Harten et al., 2021).

III. Non_adapt_80 case: In the same way than the non_adapt_50 case, the non_adapt_80 case applies a cut off to the CDF probability drainage maps computed with Workflow 3 for each producer. The tapering maps in the non_adapt_80 case only include the gridblocks that have a probability of being

drained equal or larger than 80%. In this case, the tapering coefficients, c_{ps}, are equal to the tapering coefficients in the non_adapt_00 case where the gridblocks have a CDF probability of being drained equal or larger than 80%. Otherwise, the tapering coefficients are equal to zero. Like non_adapt_50 case, non_adapt_80 case uses smoothing technique to solve abrupt changes of the tapering maps in the nearest gridblocks where the tapering coefficients change from being equal to the CDF probability (when the CDF probability of being drained is equal or larger than 80%) to zero (when the CDF probability of being drained is less than 80%), (Nagle, 2010; von Harten et al., 2021).

The tapering maps to be developed with Workflow 3 are kept fixed for all type of observations in a specific well location, model parameters (porosity and permeability), during the entire observation history, and in each of the ES-MDA iterations.

In respect to the free parameters (parameters without a coordinate location e.g., fault multipliers), the tapering coefficients, c_{fs}, follow a discrete tapering function, ranging in the discrete interval [0,1]. If the drainage area computed with streamlines for each active producer and the cut off considered in each non-adaptive localization case, crosses the faults, then the c_{fs} has a value of one. Otherwise, c_{fs} has a value of zero.

3.4. Tapering coefficients in adaptive localization scheme

The adaptive localization scheme follows a different method to define the tapering coefficients that regulate the update step during history matching. For the adaptive scheme, the tapering coefficients, c_{ps}, in Equation (10) are computed following the procedure explained by Luo et al. (2019) and Luo and Bhakta (2019), using

$$c_{ps} = \mathcal{J}\left[abs(\rho_{ps}) > \theta_{Gs}\right], \text{ for all } p \in G \quad (12)$$

where $\mathcal{I}(\cdot)$ is the indicator function, which have a value equal to the unity when there is a correlation that satisfy the condition $abs(\rho_{ps}) > \theta_{Gs}$, and a value equivalent to zero otherwise; $abs(\cdot)$ returns the absolute value of the input, ρ_{ps} denotes the correlation coefficient between a model parameter and a simulated observable; and θ_{Gs} is a positive threshold value to mitigate the correlation noise between model parameters and simulated observables, when either the correlation is weak or there is no actual correlation. In the context of ensemble-based history matching methods with a relatively small ensemble size because of sampling errors, ρ_{ps} might not be exactly zero when the pair of simulated observable and model parameter element are uncorrelated; p represents a specific model parameter (e.g., porosity or permeability); and G represents the group of the same type of petro-physical parameters. The use of θ_{Gs} in Equation (12) instead of a threshold value, θ_{ps}, for each model parameter $m_{p,n}^{l}$ is a practical implementation to reduce the complexity of the adaptive localization scheme.

The threshold value, θ_{Gs}, could be estimated, as proposed by Luo and Bhakta (2019), using an image-denoising-based method that is suitable to model parameters that are distributed over the reservoir gridblocks (called in this thesis as field parameters), such as permeability and porosity,

$$\theta_{Gs} = \sqrt{2ln(\#\rho_{Gs})}\sigma_{Gs} \quad (13)$$

$$\sigma_{Gs} = \frac{median(abs(\varepsilon_{Gs}))}{0.6745} \quad (14)$$

where $\#\rho_{Gs}$ denotes the number of elements of the correlation field ρ_{Gs}, which is a set of correlation coefficients between a fixed observable element and a group of model

parameters denoted by G; σ_{Gs} represents the noise level when treating the correlation field ρ_{Gs} as an image to be denoised because of ensemble sampling errors; ε_{Gs} is the field sampling error associated with ρ_{Gs}. The noise level in the adaptive localization scheme is estimated based on the workflow developed by Luo and Bhakta (2019) that uses the random-shuffle approach to approximate σ_{Gs}. Instead of directly estimate ε_{Gs}, the workflow developed by Luo and Bhakta (2019) estimates another set of noise fields $\tilde{\varepsilon}_{Gs}$, which are induced by sampling errors in an environment similar to the one that caused ε_{Gs}. The objective is to make that an estimated noise level $\tilde{\sigma}_{Gs}$, when using $\tilde{\varepsilon}_{Gs}$ in Equation (14), would be a reasonably good approximation to σ_{Gs}, which can be used to calculate θ_{Gs} in Equation (13).

For computing the threshold values for free parameters, θ_{fs}, which are not distributed spatially in the reservoir gridblocks, such as fault multipliers, an empirical threshold value is introduced,

$$\theta_{fs} = 3\sigma_{fs} \tag{15}$$

$$\sigma_{fs} = \frac{1}{\sqrt{N_e}} \tag{16}$$

where σ_{fs} is the sampling error noise level approximation assuming that the joint distribution of model parameter-observation pairs is Gaussian (Luo and Bhakta, 2019) . Thus, the correlation coefficient for free parameters, c_{fs}, can be computed by editing Equation (12), where ρ_{fs} represents the correlation between the simulated observable and the free parameter.

$$c_{fs} = \mathcal{J}\left[abs(\rho_{fs}) > \theta_{fs}\right] \tag{17}$$

The adaptive localization correlation coefficients in Equations (12) and (17) are resulted from the indicator function $\mathcal{I}(\cdot)$, which represents a hard tapering function, because it generates correlation coefficient in the discrete interval [0,1]. Luo and Bhakta (2019) proposed a continuous tapering function, f_{GC}, based on a Gaspari and Cohn (1999) function, that can be used for computing both c_{ps} and c_{fs},

$$f_{GC} = \begin{cases} -\frac{1}{4}z^5 + \frac{1}{2}z^4 + \frac{5}{8}z^3 - \frac{5}{3}z^2 + 1, & if\ 0 \le z \le 1 \\ -\frac{1}{12}z^5 - \frac{1}{2}z^4 + \frac{5}{8}z^3 + \frac{5}{3}z^2 - 5z + 4 - \frac{2}{3}z^{-1}, & if\ 1 < z \le 2 \\ 0, & if\ z > 2 \end{cases} \quad (18)$$

$$z = \frac{1 - abs(\rho_{ps})}{1 - \theta_{Gs}} \quad (19)$$

Then c_{ps} and c_{fs} can be expressed as:

$$c_{ps} = f_{GC}\left(\frac{1-abs(\rho_{ps})}{1-\theta_{Gs}}\right), \text{ for all } p \in G \quad (20)$$

$$c_{fs} = f_{GC}\left(\frac{1 - abs(\rho_{fs})}{1 - \theta_{fs}}\right) \quad (21)$$

In the thesis, the implemented method to compute the tapering coefficients in the adaptive localization scheme is based on the introduced studies of Luo et al. (2019), and Luo and Bhakta (2019). The process to define the adaptive localization regions and the tapering coefficients is summarized in Workflow 4. The prior ensemble of geologic models is simulated to generate the ensemble of simulated observables. The random-shuffle approach (Luo and Bhakta, 2019) is applied to estimate the sampling error $\tilde{\varepsilon}_{Gs}$, approximate σ_{Gs} with Equation (14), and calculate θ_{Gs} with Equation (13). In the case

of free parameters, the random-shuffle approach (Luo and Bhakta, 2019) is not applied. The noise level, σ_{fs}, and θ_{fs} are calculated with Equation (16) and Equation (15), respectively. The tapering coefficients for the field parameters, c_{ps}, and the tapering coefficients for the free parameters c_{fs}, are calculated based on the selected tapering function, which are discussed later when describing the adaptive cases. Workflow 4 computes correlation coefficients and tapering coefficients for each type of observations, at each observation time step, for each model parameter (porosity, permeability, and fault multipliers). In the thesis, the correlation coefficients are recomputed in every ES-MDA iteration. Therefore, the correlation coefficients for field model parameters and free model parameters can be rewrite as ${c_{ps}}^{l}$ and ${c_{fs}}^{l}$, respectively. The random-shuffle approach (Luo and Bhakta, 2019) requires independence among the reservoir realizations in the ensemble to generate reliable correlation fields. Recomputing the correlation coefficient in every ES-MDA iteration (${c_{ps}}^{l}$, ${c_{fs}}^{l}$) could make unreliable correlation fields, because the updated reservoir models become correlated after history matching observations in each iteration. However, this thesis uses a software (PIPT) that recomputes the correlation coefficient in every ES-MDA iteration and has conveyed to good history matching in previous studies.

In the thesis, using Workflow 4, three adaptive cases are defined. The cases differ in the type of tapering function used for calculating the tapering coefficients. The cases are the followings:

I. Adapt_hard case: In this case, the tapering coefficients are computed with a discrete tapering function (indicator function). Therefore, the tapering coefficients, ${c_{ps}}^{l}$ and ${c_{fs}}^{l}$, are computed with Equations (12) and (17), respectively, for each ES-MDA iteration.

II. Adapt_soft case: In this case, the tapering coefficients are computed with a continuous tapering function. Therefore, the tapering coefficients, $c_{ps}{}^{l}$ and $c_{fs}{}^{l}$, are computed with Equation (20) and Equation (21), respectively, for each ES-MDA iteration.

III. Adapt_sigm case: This case is like adapt_hard case but applying smoothing technique (Nagle, 2010; von Harten et al., 2021) in the nearest gridblocks where the hard tapering coefficients changes in the discrete interval [0,1].

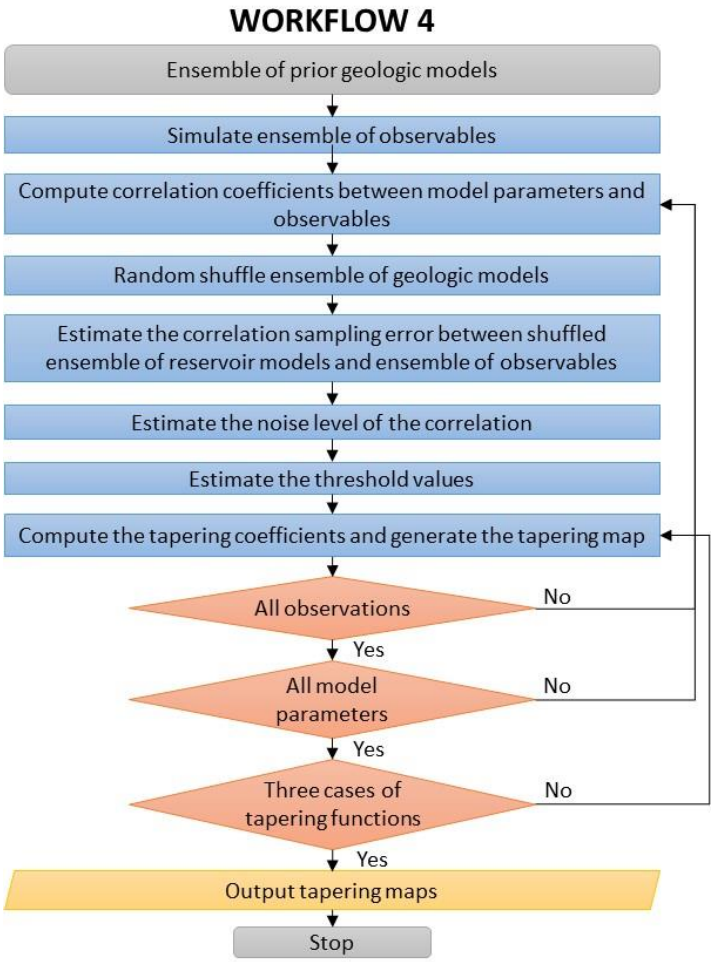

Workflow 4 Define the tapering coefficients in the adaptive localization scheme

3.5. General workflow

The general workflow of the thesis is formed by five sections:

Section i. Generation of the initial ensemble:

In this section, the initialization step of ensemble-based history matching, described in Chapter 1, is done. The model parameters to be updated are defined. In the thesis, the model parameters selected to be updated are porosity and permeability fields, and fault multipliers as scalar parameters. The initial ensemble with 100 geological realizations is generated and its coverage to the observation is evaluated qualitatively.

Section ii. Development of the benchmark case:

The benchmark case applies the ES-MDA without localization to the dataset. Specifically, the benchmark case is developed with Workflow 1.

Section iii. Selection of the best non-adaptive localization case:

The three non-adaptive cases of tapering coefficient maps (section 3.3), are computed, using Workflow 3. Then, the dataset is history matched with ES-MDA and non-adaptive localization, using Workflow 2, for each of the non-adaptive cases of tapering coefficient maps. The selection of the best non-adaptive localization case is based on the significant difference among the updated ensembles and their representativity of the Truth. The latter is a geological model that is used to simulate the observations, and it is not included in the prior ensemble. The significant difference among the updated ensembles is evaluated computing the ensemble mean $mean_{i,j}$ and standard deviation $Std_{i,j}$, Equation (25) and Equation (26), respectively. The updated ensemble representativity of the Truth is estimated computing the root mean square

deviation (RMS) of the updated ensemble against the Truth for the field parameters and the observations. For the field parameters, the RMS is reported in a 2D field map ($RMS_{i,j}$). Considering a geological realization of the ensemble with model parameters $p_{i,j,k}$, the vertical average $\bar{p}_{i,j}$ is computed for each member of the updated ensemble. Similarly, considering the Truth model with model parameters $P_{i,j,k}$, the vertical average $\bar{P}_{i,j}$ is computed. Then, the $RMS_{i,j}$ is calculated by

$$RMS_{i,j} = \sqrt{\frac{\sum_{n=1}^{N_e}(\bar{p}_{i,j,n} - \bar{P}_{i,j})^2}{N_e}} \quad (22)$$

where N_e is the number of ensemble members, n indicates the index of a member in the ensemble. For the observations, the RMS is reported as a unique value for each type of observation, o, for the entire production history, $RMS_{hist,o}$, and separately, for the prediction period, $RMS_{pred,o}$. The RMS values are computed as follow:

$$RMS_{hist,o} = \sqrt{\frac{\sum_{w=1}^{w_t}\sum_{t=1}^{t_{hist}}\sum_{n=1}^{N_e}\left(Observable_{o,n,t,w} - Observation_{o,t,w}\right)^2}{w_t * t_{hist} * N_e}} \quad (23)$$

where $Observable_{o,n,t,w}$ means the simulated observable, type o, for each ensemble member n at a time step t and for well w; $Observation_{o,t,w}$ is the observation, type o, to be generated with the Truth model at time t for well w; and w_t is the total number of wells, t_{hist} is the total number of time steps in the production history;

$$RMS_{pred,o} = \sqrt{\frac{\sum_{w=1}^{w_t}\sum_{t=1}^{t_{pred}}\sum_{n=1}^{N_e}\left(Predictible_{o,n,t,w} - Prediction_{o,t,w}\right)^2}{w_t * t_{pred} * N_e}} \quad (24)$$

where $Predictible_{o,n,t,w}$ means the simulated forecast, type *o*, for each ensemble member *n* at a time step *t* and for well *w*; $Prediction_{o,t,w}$ is the forecast, type *o*, to be generated with the Truth model at time *t* for well *w*; and w_t is the total number of wells, t_{pred} is the total number of time steps in the prediction period.

Section iv. Selection of the best adaptive localization case:

The three adaptive cases of tapering coefficient maps (section 3.4), are computed, using Workflow 4. Then, the dataset is history matched with ES-MDA and adaptive localization, using Workflow 2, for each of the adaptive cases of tapering coefficient maps. Similarly to section iii, the selection of the best adaptive localization case is based on its representativity of the Truth. In this section, the $RMS_{i,j}$, Equation (22); the $RMS_{hist,o}$, Equation (23); $RMS_{pred,o}$, Equation (24); $mean_{i,j}$ Equation (25); and standard deviation $Std_{i,j}$, Equation (26) are computed for each adaptive localization case.

Section v. Comparative analysis among updated ensembles

The three ensemble-based history matching cases results (benchmark, best non-adaptive localization, best adaptive localization) are compared based on the following criteria:

Updated ensemble mean for field properties

Considering a geological realization with model parameters $p_{i,j,k}$, the vertical average $\bar{p}_{i,j}$ is computed for each member of the updated ensemble. Then, the ensemble mean is reported in a 2D field map. For each updated ensemble, the $mean_{i,j}$ in each gridblock is calculated by

$$mean_{i,j} = \frac{\sum_{n=1}^{N_e} \bar{p}_{i,j,n}}{N_e}$$

(25)

Updated ensemble standard deviation for field properties

Considering a geological realization with model parameters $p_{i,j,k}$, the vertical average $\bar{p}_{i,j}$ is computed for each member of the updated ensemble. Then, the ensemble standard deviation is reported in a 2D field map. For each updated ensemble, the $Std_{i,j}$ in each gridblock is calculated by

$$Std_{i,j} = \sqrt{\frac{\sum_{n=1}^{N_e} (\bar{p}_{i,j,n} - mean_{i,j})^2}{N_e}}$$

(26)

Updated ensemble RMS values against the Truth

Compute the $RMS_{i,j}$, Equation (22), the $RMS_{hist,o}$, Equation (23), $RMS_{pred,o}$, Equation (24) for each ensemble-based history matching case. In addition RMS against the Truth can be computed for production rates and production cumulated volumes, during production history and prediction period, with Equations (23) and (24), respectively, substituting the type of observation *o* by keywords for production rate and production cumulated volumes.

$$RMS_{hist,r\_v} = \sqrt{\frac{\sum_{w=1}^{w_t} \sum_{t=1}^{t_{hist}} \sum_{n=1}^{N_e} \left(Observable_{r\_v,n,t,w} - Observation_{r\_v,t,w}\right)^2}{w_t * t_{hist} * N_e}}$$

(27)

$$RMS_{pred,r\_v} = \sqrt{\frac{\sum_{w=1}^{w_t} \sum_{t=1}^{t_{pred}} \sum_{n=1}^{N_e} \left(Predictible_{r\_v,n,t,w} - Prediction_{r\_v,t,w}\right)^2}{w_t * t_{pred} * N_e}}$$

(28)

where the subscript r_v represents the keywords for production rate and production cumulated volumes for oil, gas, and water. In this thesis, the production data are well

water production rate (WWPR), well oil production rate (WOPR), well gas production rate (WGPR), well water total production (WWPT), well oil total production (WOPT), and well gas total production (WGPT). In this thesis, the production data are different to the observations defined in section 3.6 (WBP9, WWCT, WGOR). The observations are used for conditioning the history matching, but the production data are not. In this thesis, the RMS_{hist,r_v} and RMS_{pred,r_v} are calculated to evaluate the updated ensemble capacity to predict data that have not being used for conditioning the ensemble in the history matching.

Updated ensemble RMS values against the initial ensemble

Compute the root mean square deviation of the updated ensemble against the initial ensemble for field model parameters $RMS_{i,j,initial}$. Analogously to $RMS_{i,j}$, $RMS_{i,j,initial}$ is reported in a 2D field map. Considering a geological realization of the ensemble with model parameters $p_{i,j,k}$, the vertical average $\bar{p}_{i,j}$ is computed for each member of the updated ensemble. Considering a geological realization of the initial ensemble with model parameters $p_{i,j,k,initial}$, the vertical average $\bar{p}_{i,j,intial}$ is computed for each member of the initial ensemble. Then, the $RMS_{i,j,initial}$ is calculated by

$$RMS_{i,j,initial} = \sqrt{\frac{\sum_{n=1}^{N_e}(\bar{p}_{i,j,n} - \bar{P}_{i,j,n\ initial})^2}{N_e}}$$

(29)

Updated ensemble coverage of observations and measurement errors

Better updated ensemble coverage of the observations and their measurement errors means better quantification of the model parameter uncertainties by the updated ensemble. Fig. 13 shows an example of production rate vs time plot, including simulated observables and observations for a study case developed by Evensen (2021). The green lines represent the initial ensemble, the magenta lines stand for the updated ensemble, the

black dots are the observations, and the black vertical lines are the spread of the measurement errors. Commonly, a black vertical line represents the P10-P90 interval or P5-P95 interval of the measurement error. Fig. 13 shows that the spread of the updated ensemble (magenta ensemble) is smaller than the spread of the initial ensemble (green ensemble) and is covering the observations and their measurement errors during history. The history matching achieved with the updated ensemble (the magenta ensemble) is an example of good coverage to the observations and their measurement errors.

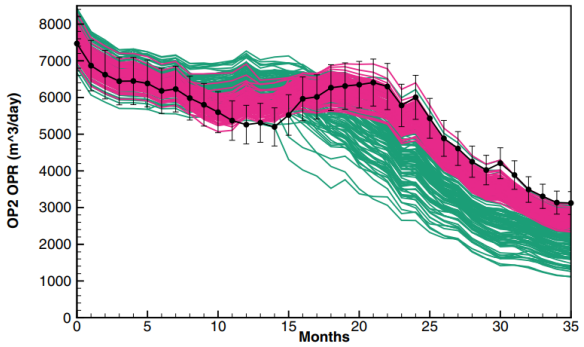

Fig. 13 Example of final ensemble coverage analysis plot from Evensen (2021).

Updated ensemble free parameter distribution

For each free model parameter, the updated ensemble probability distribution is illustrated with a boxplot to be qualitatively compared against the value of the Truth model.

The comparative analysis section can be summarized with Workflow 5, where the Truth model, initial ensemble and updated ensembles are inputs of the process; all the comparative criteria described in this section are applied, and the best ensemble-based history matching scheme (AHM) is selected for the studied dataset.

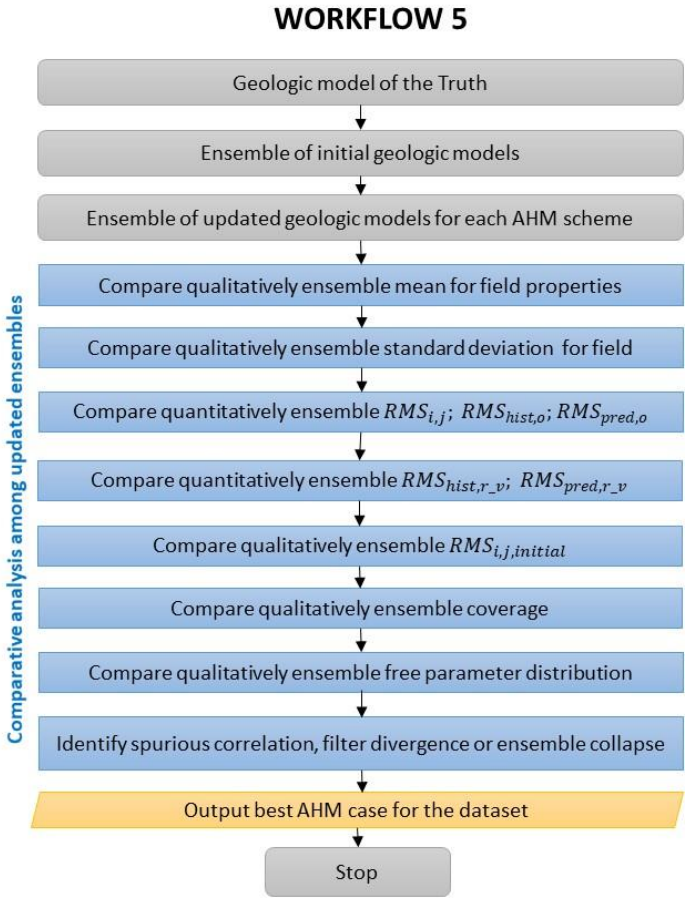

Workflow 5 Perform comparative analysis among updated ensemble members

Tools to support the general workflow

The general workflow uses a fast update modelling workflow developed by Equinor ASA, which integrates different tools, such as: ERT ("Welcome to ERT's documentation! — ERT 2.30.0rc1.dev46+g6ccfc183 documentation," n.d.), Eclipse ("ECLIPSE Industry Reference Reservoir Simulator," n.d.), and RMS ("Products by Emerson E&P Software," n.d.). Additionally, the ensemble-based history matching with adaptive localization is executed with Python Inverse Problem Toolbox (PIPT), which is an internal tool developed under collaboration agreement between Equinor ASA and NORCE ("About us - Norce," n.d.). In the thesis, different python scripts were created for pre-processing and post-processing data. Fig. 14 summarizes the main tools to apply in each section of the general workflow. In the lower part, in Fig. 14, every tool is assigned to a color box.

The white boxes stack the five sections of the general workflow. The semicircles located at the left in Fig. 14 are connected to each section of the general workflow, and they are filled with the colors of the tool's boxes. Most of the semicircle are colored with a gradient fill of two colors, corresponding to the main tools applied in that section. In addition, Fig. 14 includes a bullet list with the main job to be done in each section and the workflows to apply.

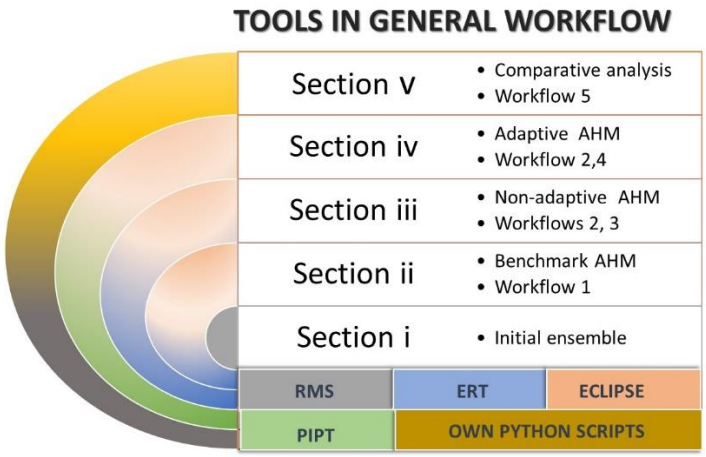

Fig. 14 Color diagram to illustrate the main tools in each section of the general workflow

3.6. Dataset

The dataset corresponds to a synthetic field, named Reek. The Truth geological realization is not included in the initial ensemble, and it is used to simulate the observations to be used for history matching, and the predictions for evaluating the updated ensembles prediction power. General features about the structural, facies, petrophysics, and well modelling of the Reek field will be described in this section as follow:

Structural modelling

Reek field has a horst-and-graben structural style. It consists of one formation with fourteen layers. The formation tops range from 1550m to 1960m. Six normal faults cut

the formation (F2, F3, F4, F5, F6, F7). Vertical fault's displacements limit lateral communication but make no isolated compartments. Fault locations, depth of formation tops and Truth model fault multipliers (MULTFLT) for each fault are displayed in Fig. 15. The fault multipliers are the only uncertain structural parameters in the Reek model; their uncertainties are modelled using log-uniform distributions with possible values ranging in the continuous interval [0.001, 1]. Formation tops and fault displacements are kept fixed in each initial ensemble member. In the thesis, the structure is not updated during the ensemble-based history matching.

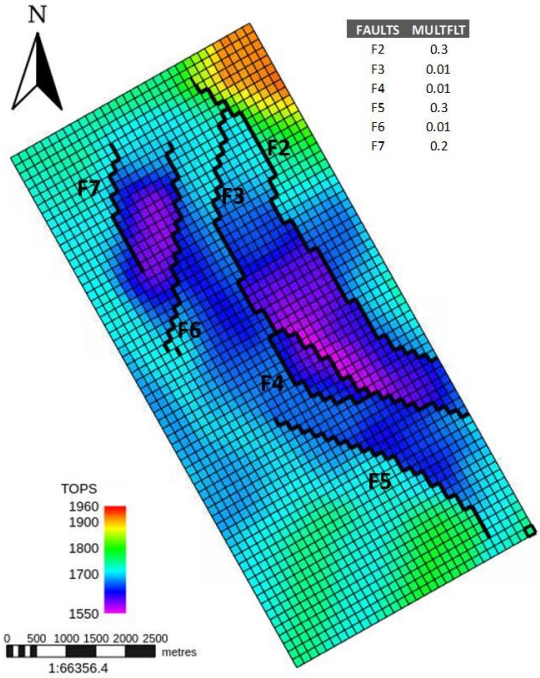

Fig. 15 Structural modelling of the Reek model.

Facies modelling

In the thesis, the Reek model is a simple reservoir model that does not have facies modelling described. Therefore, the initial ensemble does not include uncertainties in facies modelling.

Petrophysics modelling

The porosity and permeability vertical average of the Truth model are shown in the left and in the right panel of Fig. 16, respectively. The Reek reservoir model includes uncertainties in porosity and permeability. In the thesis, the Reek reservoir model is provided with an initial ensemble of porosity. The porosity values range in a continuous interval [0.001,0.5]. The initial ensemble of permeability is built with a stochastic perm-porosity transform that is illustrated in Fig. 17.

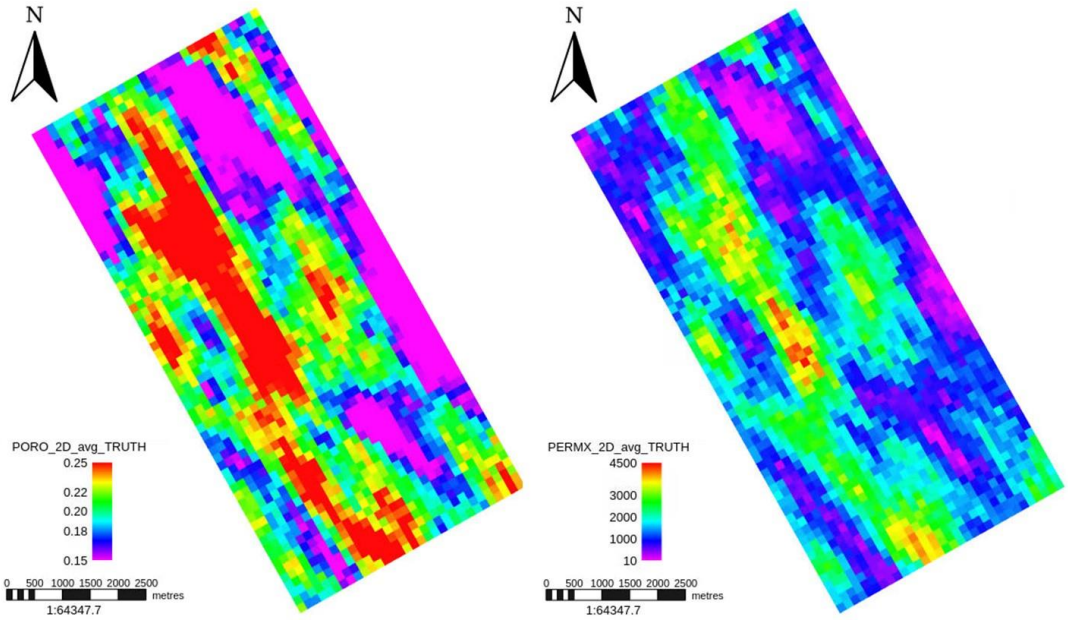

Fig. 16 Porosity and permeability vertical average of the Truth model.

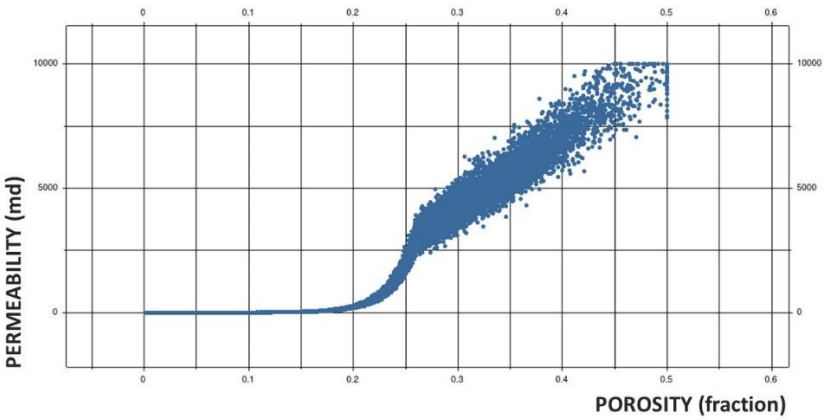

Fig. 17 Permeability – porosity transform to build the permeability initial ensemble.

Well modelling

Reek reservoir model includes five producer wells and three injector wells. The wells' locations are illustrated in Fig. 18. The available observations are monthly well water cut (WWCT), well gas-oil ratio (WGOR), and well-9-blocks-average pressure (WBP9) which represents the average pressure of the nine surrounding and connected gridblocks to a given well. The whole production dataset has seven years in total, and it was split into a history-matching period and a prediction period. The production history lasts three years from February 2000 until January 2003. The prediction period lasts four years from February 2003 until January 2007. The first three producers (OP_1, OP_2, OP_3) are active during the entire production and prediction history. Producers OP_4 and OP_5 start production a year later than OP_1, OP_2 and OP_3, January 2001. The injector wells WI_1, WI_2 and WI_3 start injection in April 2000, Jun 2000, and March 2001, respectively.

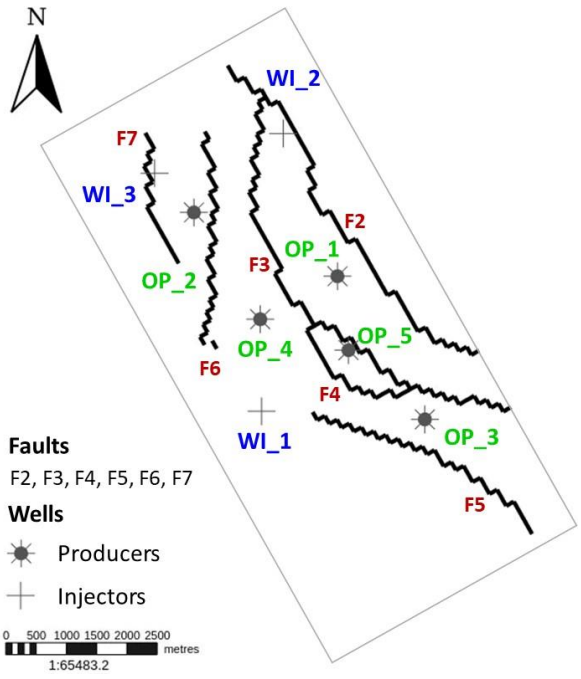

Fig. 18 Producer and injector wells in Reek reservoir model

4. RESULT ANALYSIS

4.1. Initial ensemble

The initial ensemble was generated with a prior knowledge for porosity, permeability, and fault multipliers. The ensemble $mean_{i,j}$ for each field property (each model parameter) are shown in Fig. 19. The porosity uncertainty is modelled using a Gaussian distribution, and the permeability uncertainty is modelled using a lognormal distribution. Both maps in Fig. 19, porosity $mean_{i,j}$ at the left panel, and natural logarithmic of the permeability $mean_{i,j}$ at the right panel, show smooth variation of the $mean_{i,j}$ values in the 2D space of Reek reservoir model. The fault multiplier uncertainty is modelled using a lognormal uniform distribution. The initial fault multiplier distributions are outlined in Fig. 20.

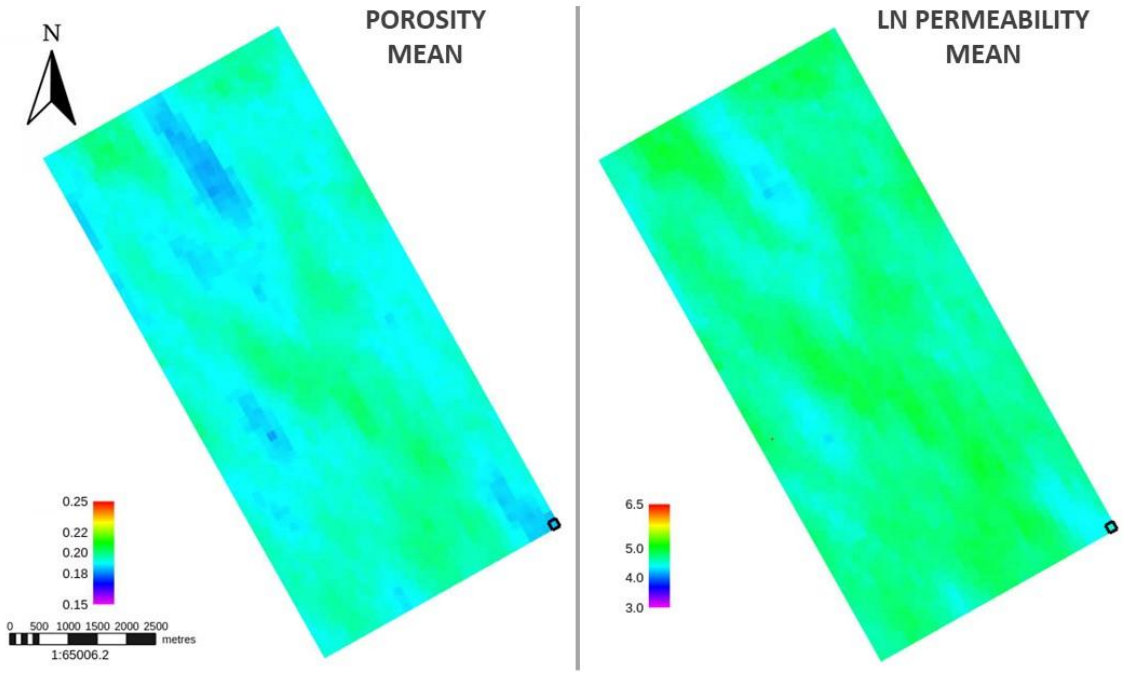

Fig. 19 Porosity and permeability mean map of the initial ensemble.

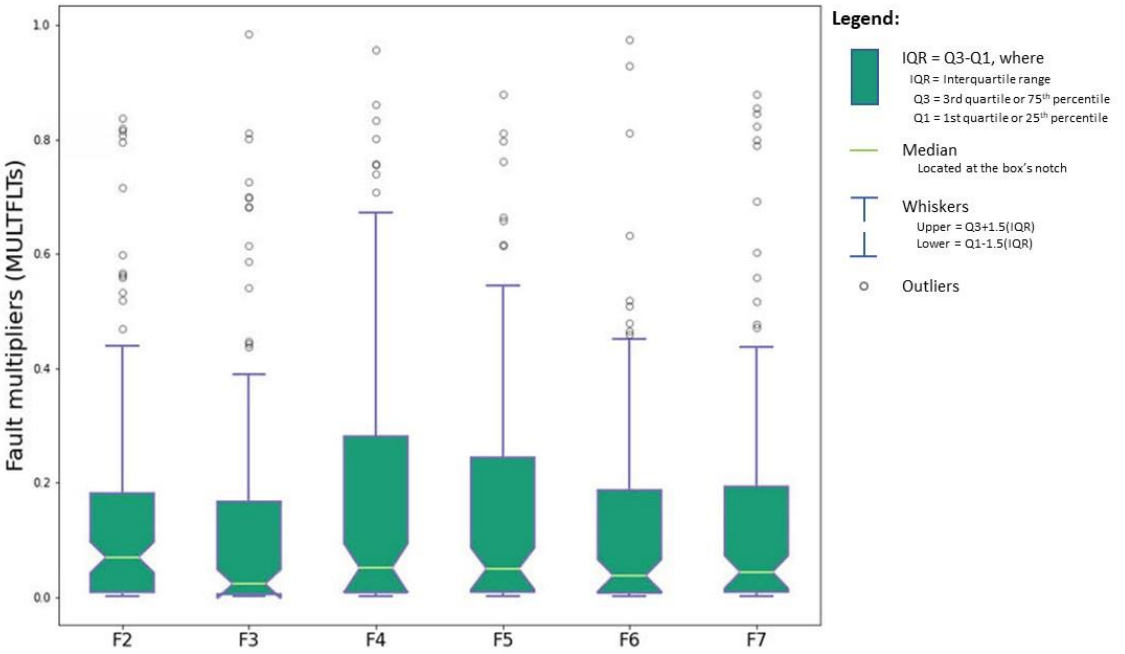

Fig. 20 Fault multipliers distribution of the initial ensemble.

The initial ensemble coverage in wells OP_1 and OP_2 for well-9-blocks-average pressure (WBP9) observations are shown in Fig. 21. The initial ensemble spread between its minimum and maximum value for each time step is illustrated in blue. The observations in the production history (Feb 2000 to Jan 2003) are illustrated with a continuous black line, and their measurement errors (error bars) are illustrated with vertical lines. The observations are only those points with error bars, they are not continuous, but for easy the visualization of the observation and prediction plots, the observations are illustrated with a continuous line. The Truth model prediction is plotted with a black dash line in Fig. 21 for both wells. The initial ensemble spread covers the observations (WBP9, WWCT, WGOR) and their measurement errors (see Appendix A for other wells and type of observations).

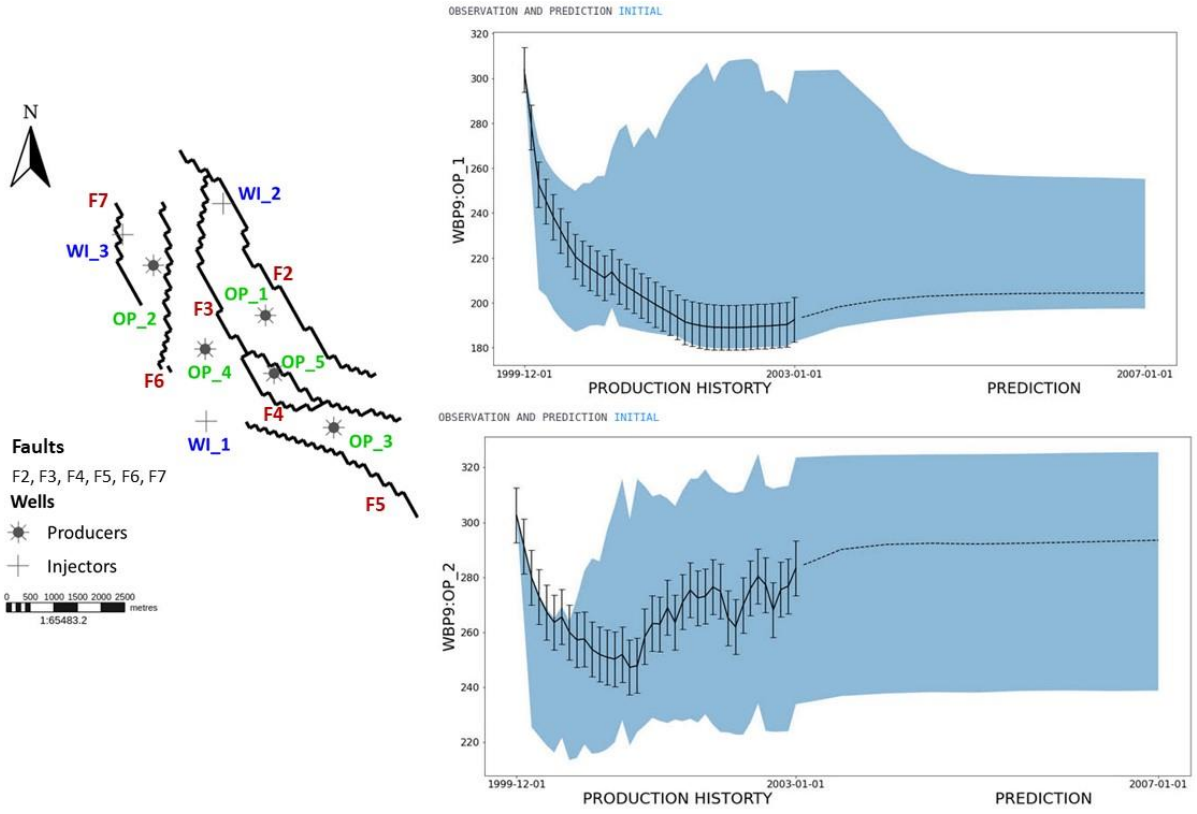

Fig. 21 Initial ensemble coverage of WBP9 observations in wells OP_1 and OP_2.

4.2. Benchmark case

In the benchmark case, the porosities, log-normal permeabilities and fault multipliers were updated with ES-MDA without localization. The vertical average values ($mean_{i,j}$) for porosities and for the lognormal permeabilities are illustrated in Fig. 22. The updated porosities and lognormal permeabilities are correlated in the 2D space of the reservoir model. The correlation between porosity and permeability is due to the permeability-porosity transformation applied when developing the initial ensemble (Fig. 17). Areas with greater porosity values tend to have greater permeability values (green areas in the maps at left and right panels in Fig. 22); and areas with lower porosity values tend to have lower permeability values (dark blue and magenta areas in the maps at left and right panels in in Fig. 22).

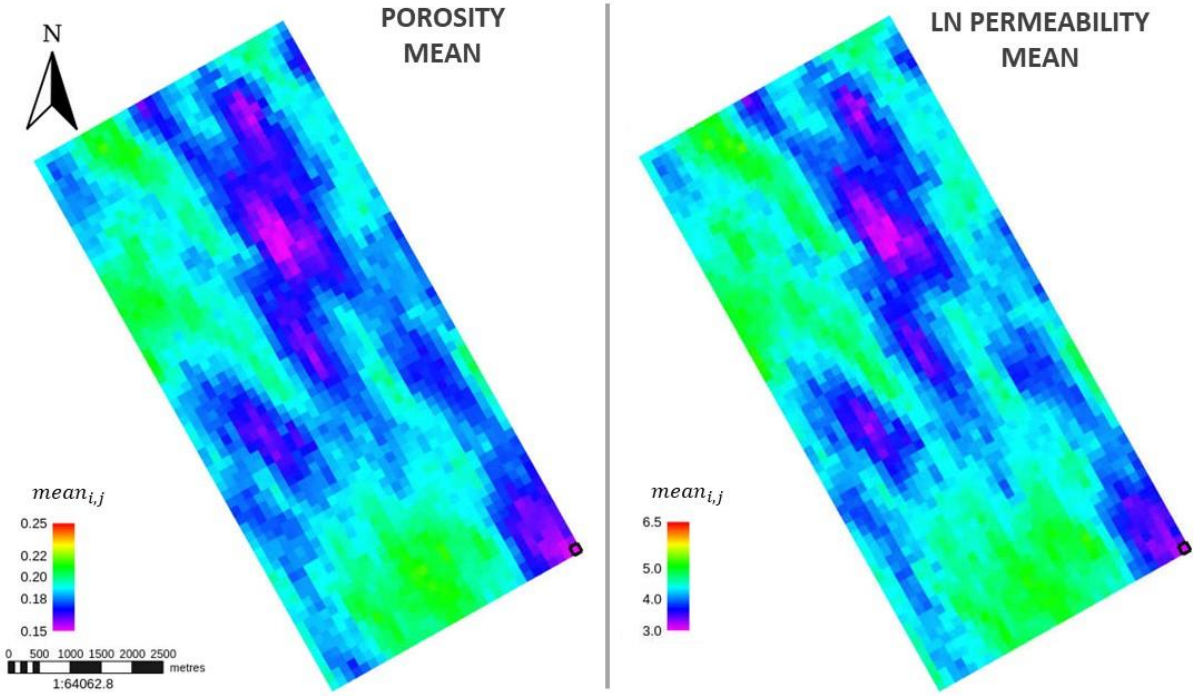

Fig. 22 Porosity and permeability mean maps of the updated benchmark ensemble.

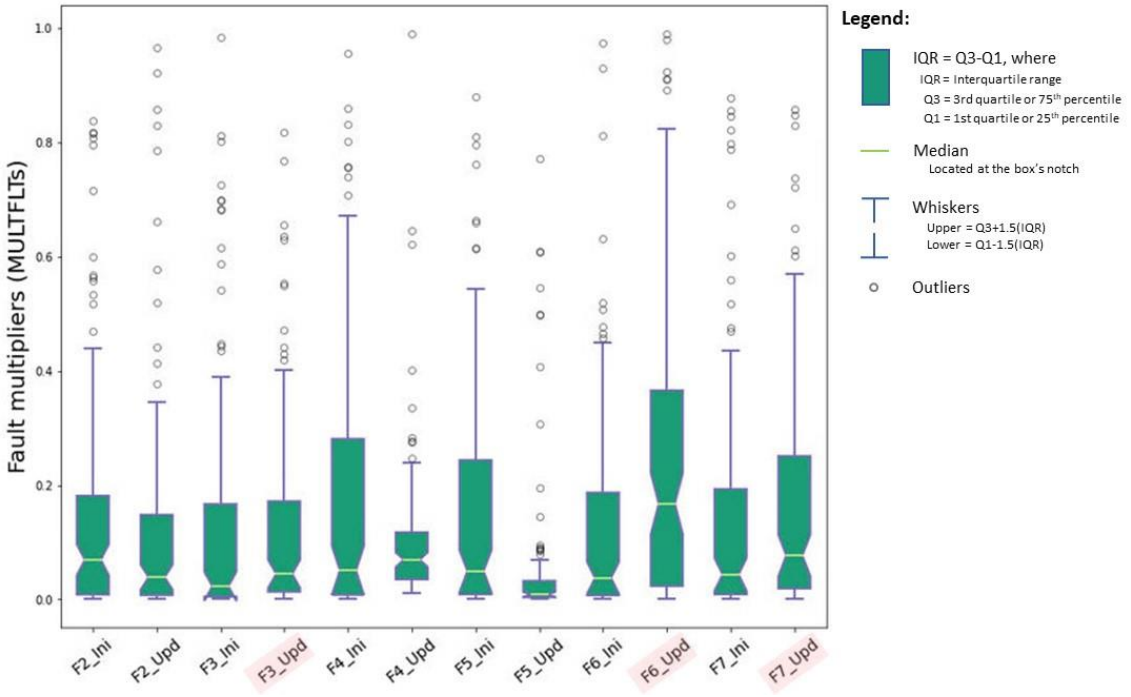

Fig. 23 Fault multipliers distribution of the initial and updated benchmark ensemble.

The initial and updated benchmark fault multiplier distributions are outlined in Fig. 23.

The fault multiplier standard deviation of the benchmark ensemble increased in F3, F6

and F7 (faults highlighted in Fig. 23). This means that the uncertainty of these three faults increased after benchmark history matching. The rest of the fault multipliers distributions show a reduction of their standard deviation after history matching.

In general, the updated benchmark ensemble has a narrower ensemble spread of simulated observables than the initial ensemble does, and it has a good coverage of the observations, because the benchmark ensemble spread covers the observations and their measurement errors in the entire history. In Fig. 24, the updated benchmark ensemble min-max interval is illustrated in green for WBP9 observables in wells OP_1 and OP_2, and it is overlapped over the initial ensemble. Fig. 24 shows an example of the benchmark good coverage over observations. However, in two wells, the benchmark updated ensemble for the simulated WWCT and WGOR observables shows a wider ensemble spread than the initial ensemble. In Fig. 25, an example of the updated benchmark ensemble spread increment over the initial ensemble is illustrated for WWCT and WGOR observations in well OP_3. The increment in the updated benchmark ensemble spreading might be caused by spurious correlation and filter divergence. Also, it is noticed that water breakthrough does not occur during the history matching period in well OP_3 (upper panel in Fig. 25) and OP_5 (last panel in Fig. B- 2). Late water breakthrough (approximate during the last year of history) occurs in all the wells (see Appendix B for updated benchmark ensemble coverage in other wells and over other type of observations).

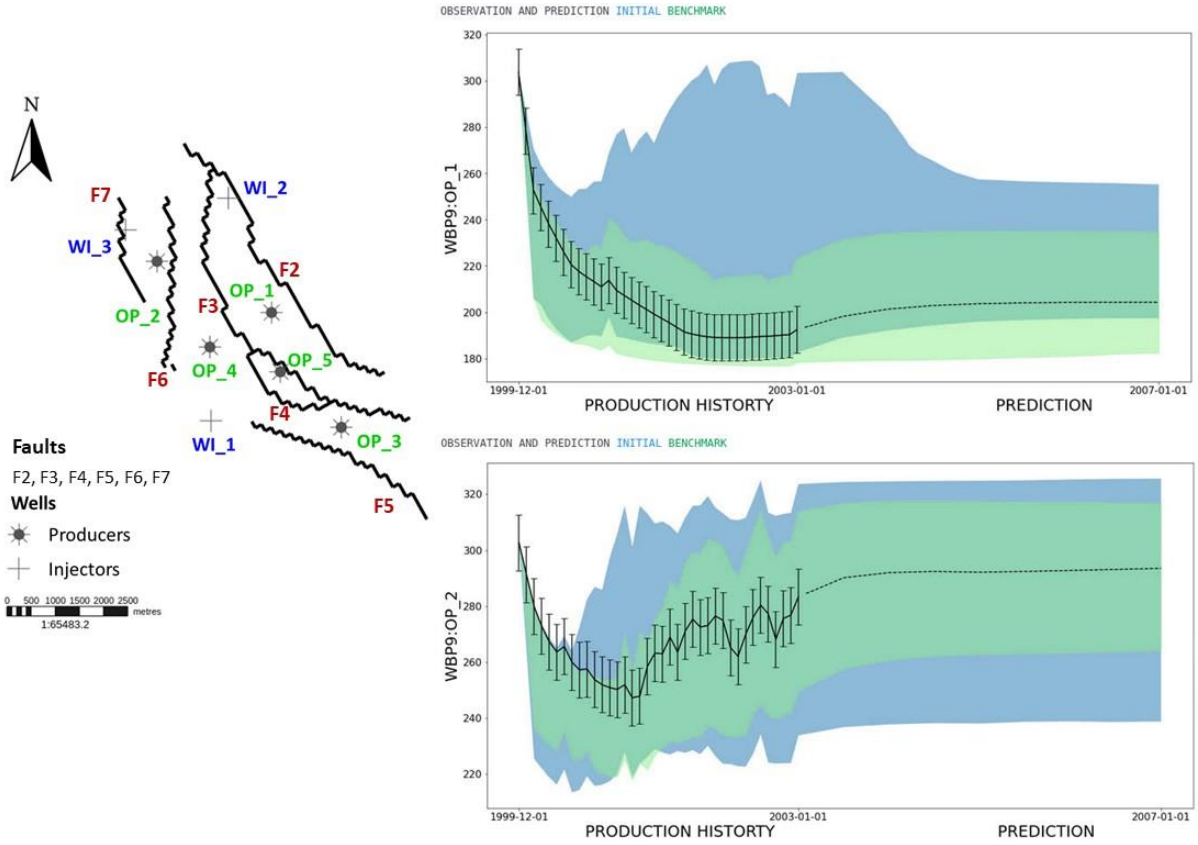

Fig. 24 Initial and updated benchmark ensemble coverage of WBP9 observations in wells OP_1 and OP_2.

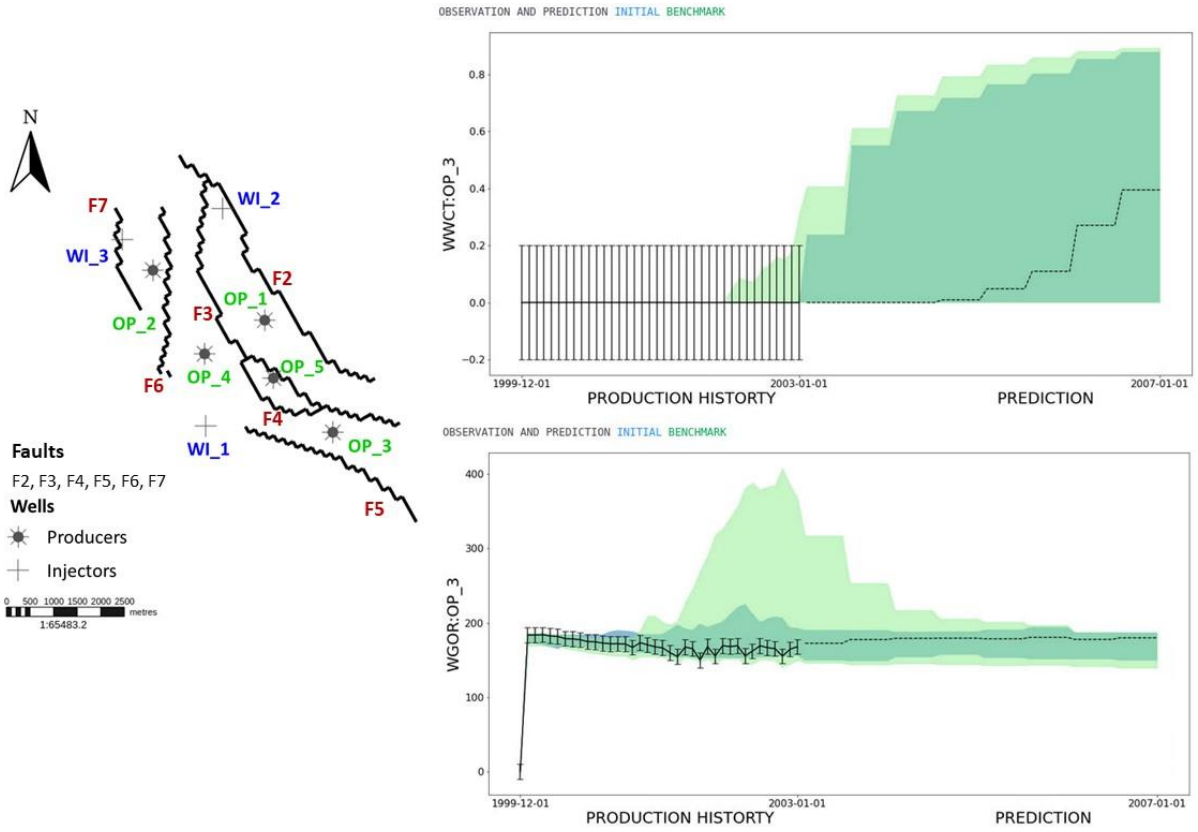

Fig. 25 Initial and updated benchmark ensemble coverage of WWCT and WGOR, well OP_3.

4.3. Best non-adaptive localization case

Workflow 3 was applied to compute the tapering coefficients in the non-adaptive localization scheme. Fig. 26 shows the tapering coefficients of observations in OP_1 for each non-adaptive localization case. The tapering coefficients range in the continuous interval [0,1], being either one or closer to one in the proximity to OP_1 location and decreasing smoothly as farther they get from OP_1. The updating influence area that the OP_1 observations have over model parameters is larger in the non_adapt_00 case, where all the gridblocks that are drained by OP_1, based on streamlines, have a tapering coefficient larger than zero. In the non_adapt_50 and non_adapt_80 cases, the updating influence area of observations in OP_1 gets truncated based on the selected probability cut-off and the smoothing (explained in section 3.3). The non_adapt_80 case has an updating influence area similar to the practical elliptical approach for distance-based localization proposed by Emerick and Reynolds (2010) and Luo et al. (2019), (see Appendix C for the tapering coefficient of observations in other wells).

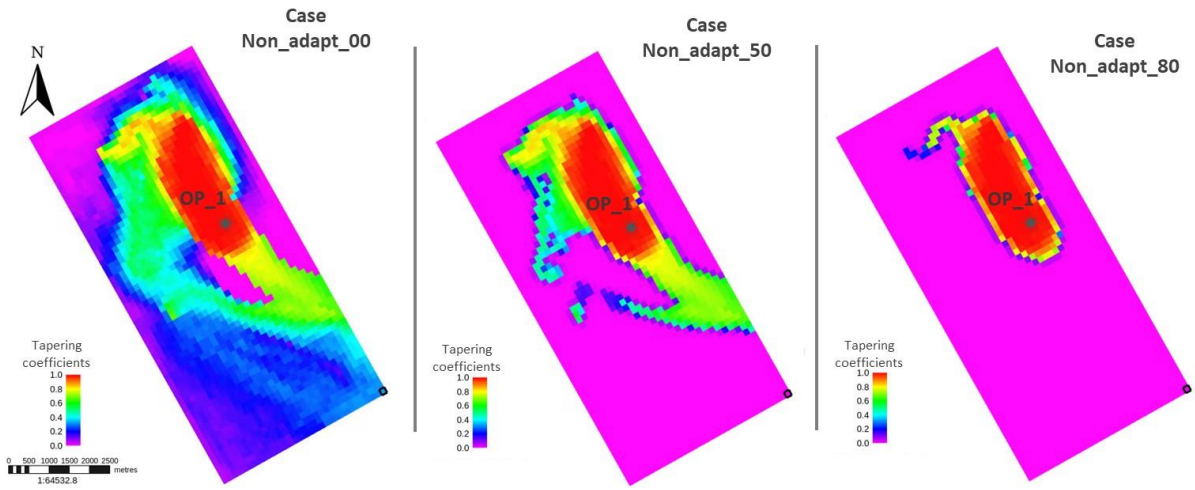

Fig. 26 OP_1 observation tapering coefficients for the three non-adaptive cases.

In this section of the thesis, the objective is to choose the best non-adaptive localization case among the three non-adaptive cases by analyzing the results based on the criteria

explained in Chapter 3, section 3.5. The porosity $mean_{i,j}$ of the updated non-adaptive ensembles are illustrated in Fig. 27. The three non-adaptive cases show similar property patterns. The three non-adaptive cases make good-quality rock channels and poor-quality rock areas more visually obvious, compared to the quality rock observed in the initial ensemble in Fig. 19. This good-quality-rock channels for each non-adaptive cases are illustrated in Fig. 27 where red, yellow, and green colors stand for good porosity values and illustrate a streak or channel shape, oriented NW-SE. The red, yellow, and green colors indicate good-quality-rock channels in the non-adaptive updated ensembles. Similarly, in the three non-adaptive cases, poor-quality-rock reservoir is updated in the same areas of the reservoir model, represented in magenta and blue colors in Fig. 27. The porosity standard deviation $Std_{i,j}$ of the updated non-adaptive ensembles are illustrated in Fig. 28, where larger $Std_{i,j}$ are coloured yellowish or reddish, and smaller $Std_{i,j}$ are presented with greenish and bluish colours. The three non-adaptive localization cases perform stronger updates in the central area of the model, reducing the ensemble standard deviation (i.e., spread) in this area, and differ in the way how the update is performed closer to the edges of the model. Neither of the three non-adaptive localization cases present ensemble collapse, which means that the $Std_{i,j}$ values for the three cases are larger than zero. In the case of ensemble collapse, the $Std_{i,j}$ are equal to zero and would be colored in magenta in a similar plot to Fig. 28. In the non_adapt_00 case, the $Std_{i,j}$ values tend to be smaller towards the reservoir model edges in comparison with the non_adapt_50 and non_adapt_80 cases. Unlike the non_adapt_00 case, in the non_adapt_50 and non_adapt_80 cases, the updates are governed and limited to a less extended space. However, the ensemble $Std_{i,j}$ differences among the three non-adaptive cases are insignificant.

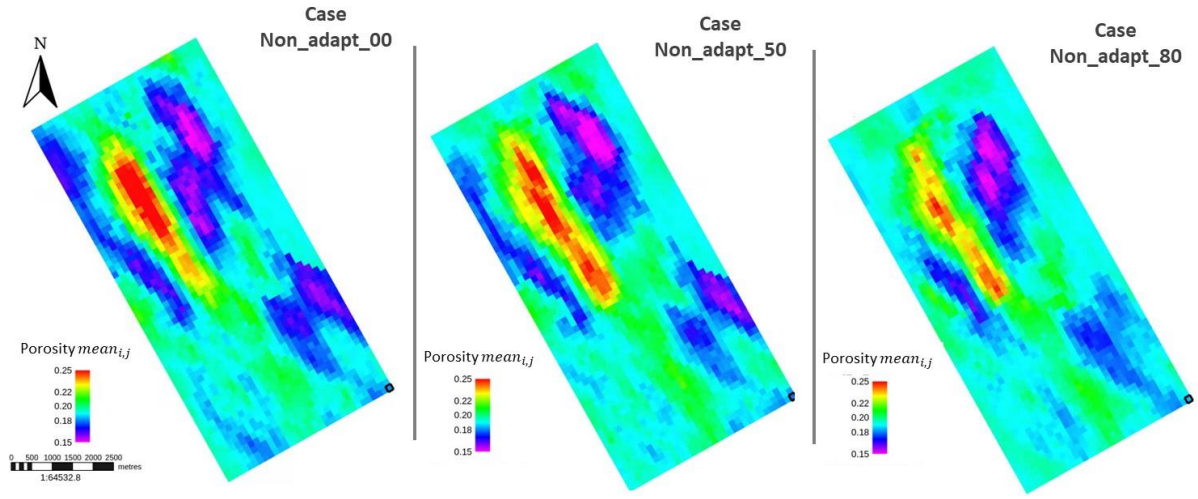

Fig. 27 Updated ensemble porosity mean for the three non-adaptive cases.

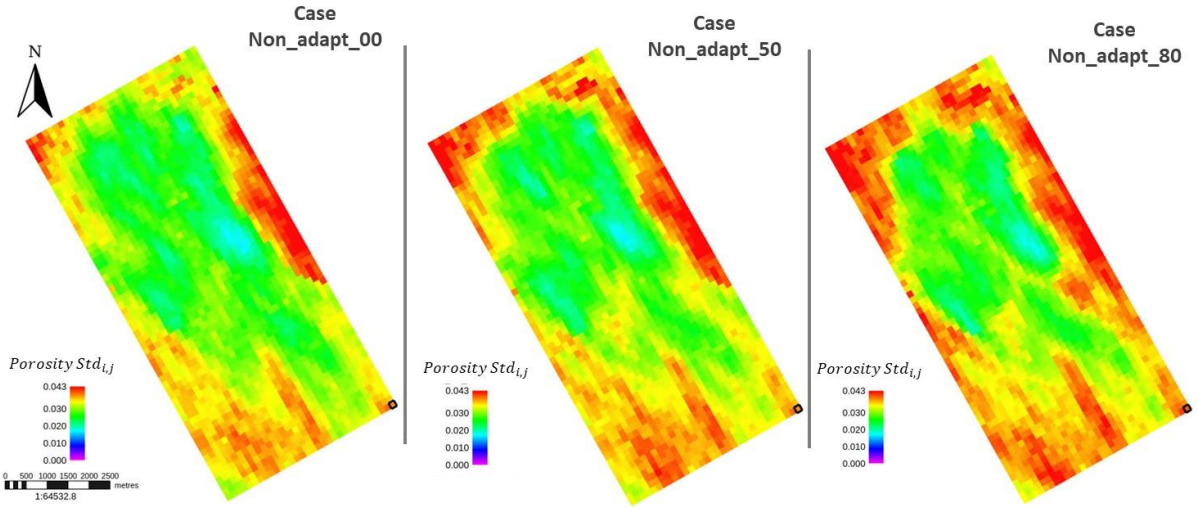

Fig. 28 Updated ensemble porosity standard deviation for three non-adaptive cases.

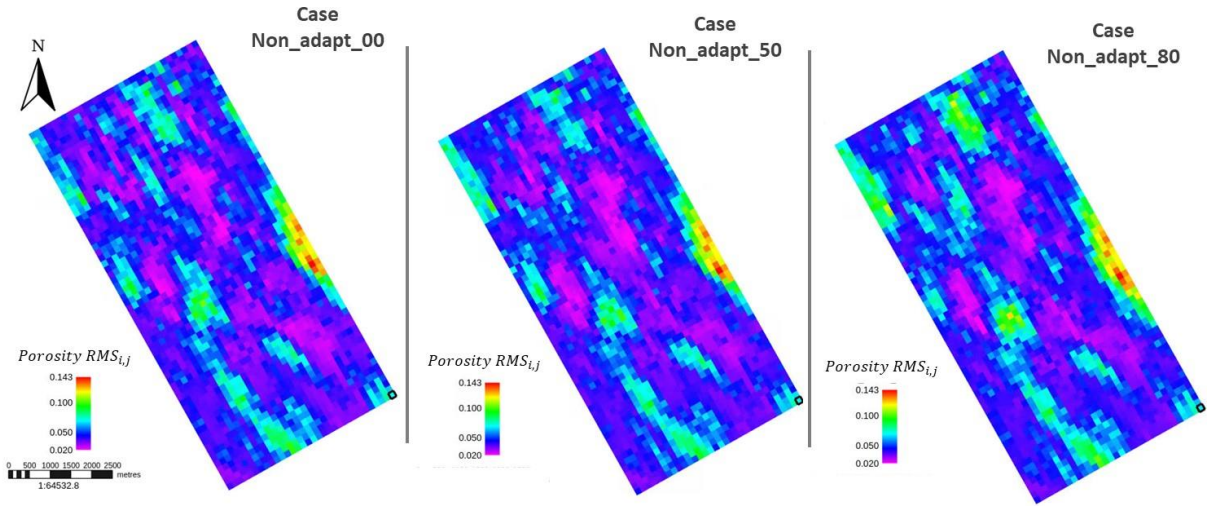

Fig. 29 Updated ensemble porosity RMS for three non-adaptive cases.

In addition, the porosity $RMS_{i,j}$ against the Truth for each of the three non-adaptive cases are illustrated in Fig. 29. The $RMS_{i,j}$ results of the three non-adaptive cases are alike. Lower and larger $RMS_{i,j}$ values are occurring in approximately the same areas among the three non-adaptive cases (see Appendix C for the updated non-adaptive ensemble permeability results). The $RMS_{hist,o}$ and $RMS_{pred,o}$ for the initial, benchmark, and the three non-adaptive cases are summarized in Fig. 30. As explained in Chapter 3, section 3.6, the production history lasts three years from February 2000 until January 2003, and the prediction period lasts four years from February 2003 until January 2007. The application of ensemble-based history matching (without localization and with non-adaptive localization) reduces the RMS values during history and prediction, which indicates that the updated ensembles can predict production in terms of WBP9, WWCT and WGOR with a higher accuracy than the initial ensemble. The non_adapt_00 case achieves smaller RMS values against the Truth than the benchmark, non_adapt_50 and non_adapt_80 cases do for WBP9 observations during production and prediction period. For the WWCT observations, the non_adapt_00 case achieves RMS values against the Truth like the non_adapt_50 and non_adapt_80 cases do and smaller to the benchmark case does during production and prediction period. For WGOR observations, the non_adapt_00 case achieves RMS values against the Truth smaller than the benchmark case does and smaller or equal than the non_adapt_50 and non_adapt_80 cases do, respectively, during prediction period.

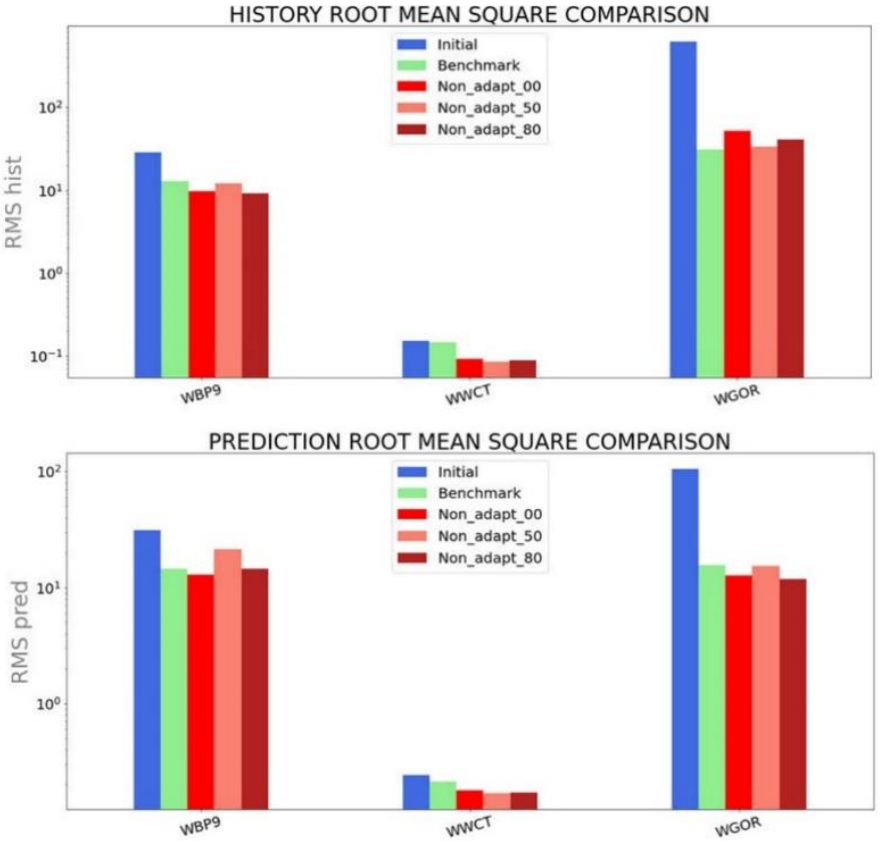

Fig. 30 RMS non-adaptive cases for production history and prediction period.

In summary, the comparative results analysis of the property $mean_{i,j}$, Fig. 27, indicates that the three non-adaptive cases generate alike patterns on the spatial distribution of the field model parameters (porosities and permeabilities). The comparative evaluation of the property $Std_{i,j}$, Fig. 28, indicates that the three non-adaptive cases are reducing the uncertainty in the field model parameters without suffering of ensemble collapse. The comparative results analysis of $RMS_{i,j}$, Fig. 29, indicates that there are not significant changes in the achieved RMS values among the three non-adaptive cases for field model parameters. The $RMS_{hist,o}$ and $RMS_{pred,o}$ results, Fig. 30, for the three non-adaptive cases, indicate that the history matching cases with non-adaptive localization achieve better prediction accuracy than the initial ensemble does. Based on the results analysis discussed for $mean_{i,j}$, $Std_{i,j}$, $RMS_{i,j}$, $RMS_{hist,o}$, $RMS_{pred,o}$, the three non-adaptive

localization cases perform history matching without significant differences among them. The non-adaptive localization history matching results for permeability are in Appendix C, and they are consistent with the discussed history matching results for porosity. In the thesis, the non_adapt_00 case was selected as the best non-adaptive case. The main reason for the selection was that the tapering coefficients in non_adapt_00 case are purely physically defined by streamline simulations, without including a user-defined cut off for reducing the observation influence area over model parameters.[16] In addition, it is observed that the non_adapt_00 case has a better predictivity power (predictivity accuracy) than the benchmark case does for all type of observations (WBP9, WWCT, WGOR), which is illustrated with smaller $RMS_{pred,o}$ in Fig. 30.

4.4. Best adaptive localization case

Workflow 4 was applied to compute the tapering coefficients in the adaptive localization scheme. The adaptive tapering coefficient maps are sensible to the type of observation, model parameter, time step and ES-MDA iteration. For illustration of the tapering rule differences among adaptive cases, the tapering coefficient maps for the three type of OP_1 observations (WBP9, WWCT and WGOR) over permeability are illustrated in Fig. 31, Fig. 32, and Fig. 33, respectively, for Feb 1st 2000. The adaptive tapering coefficients range in the interval [0,1] for each of the adaptive cases. However, the adapt_soft tapering coefficients are smaller and smoother than the tapering coefficients in adapt_hard and adapt_sigm cases. The adapt_soft tapering coefficients are represented with colors mostly blueish and greenish, which means than the tapering coefficients are

[16] We do not see any theory to support what the optimal cut-off probability should be, and thus, defining the cut-off probability is purely subjective. In practice, we recommend minimizing the number of user-defined inputs/parameters for minimizing the impact of subjectiveness (i.e., human factors) on history-matching results.

dominantly between 0.4 and 0.6. Unlike the adapt_soft case, the adapt_hard and adapt_sigm cases show larger heterogeneity in the spatial distribution of the tapering coefficients, represented with a wider tapering coefficients range, from magenta to red colors. Also, it is observed that the adapt_sigm case presents the same trend of tapering coefficient as the adapt_hard case does but including smoothness at the edges. The comparison of the tapering coefficients maps among Fig. 31, Fig. 32, and Fig. 33 exemplifies how the tapering coefficients with the adaptive localization scheme, change for different type of observations in each tapering rule (soft, hard and sigm). Thus, the adaptive localization scheme calculates tapering coefficients sensitive to different physical correlations among simulated observables and model parameters. For illustration of the adaptive tapering coefficients sensitivity to reservoir dynamics (which means that the tapering coefficients can change in time), the tapering coefficient maps for the three type of OP_1 observations (WBP9, WWCT and WGOR) over permeability are illustrated in Fig. 34, Fig. 35, and Fig. 36, respectively, for Feb 1st 2002. The adaptive tapering coefficients sensitivity to reservoir dynamics is observed when comparing the tapering coefficient map of the same observation type in Feb 1st, 2000, with the tapering coefficient map in Feb 1st, 2002. Adaptive tapering coefficient differences are observed in Fig. 31, Fig. 32, and Fig. 33 vs Fig. 34, Fig. 35, and Fig. 36, respectively. In addition, the user criteria have low influence in the calculation of the adaptive tapering coefficients. Unlike the non-adaptive tapering coefficients, the adaptive tapering coefficients are calculated automatically based on the chosen tapering rule (soft, hard or sigm), and the reservoir-dynamics correlations among the simulated observables and the model parameters. In PIPT, the user can apply a tuning factor to modifies the positive threshold, θ_{Gs} , and can choose the tapering rule (soft, hard or sigm). In this thesis, the tuning factors used were 0.1, 0.1, and 1 for the adapt_soft, adapt_hard, and adapt_sigm, respectively.

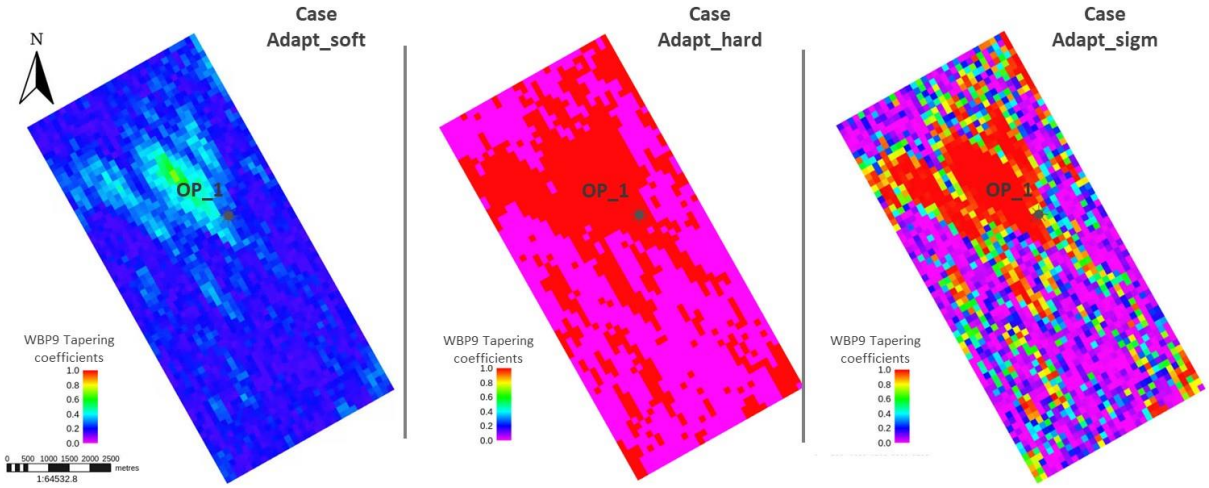

Fig. 31 OP_1 WBP9 tapering coefficients over permeability, the three adaptive cases, first iteration, Feb 1st, 2000.

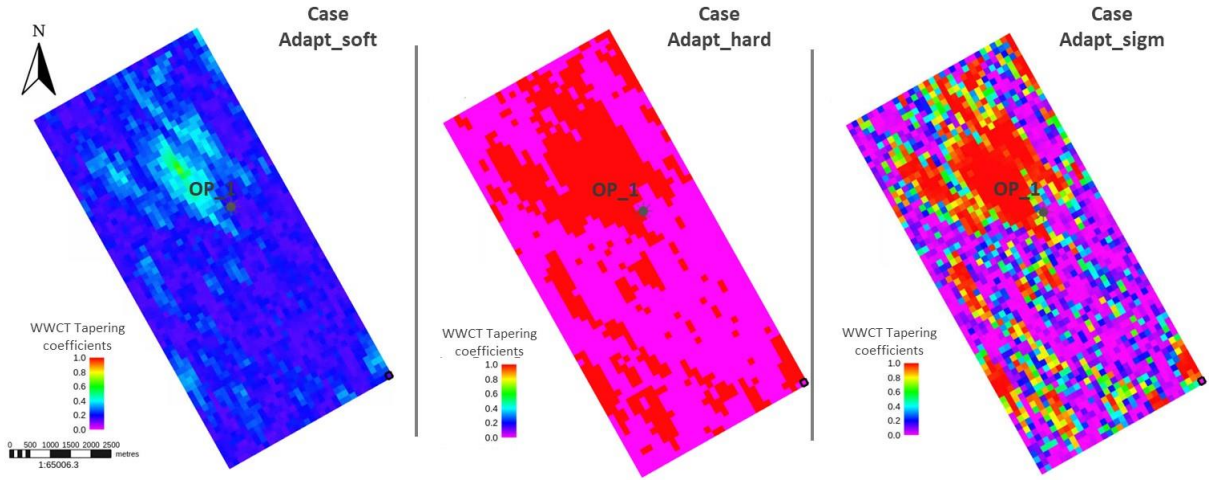

Fig. 32 OP_1 WWCT tapering coefficients over permeability, the three adaptive cases, first iteration, Feb 1st, 2000.

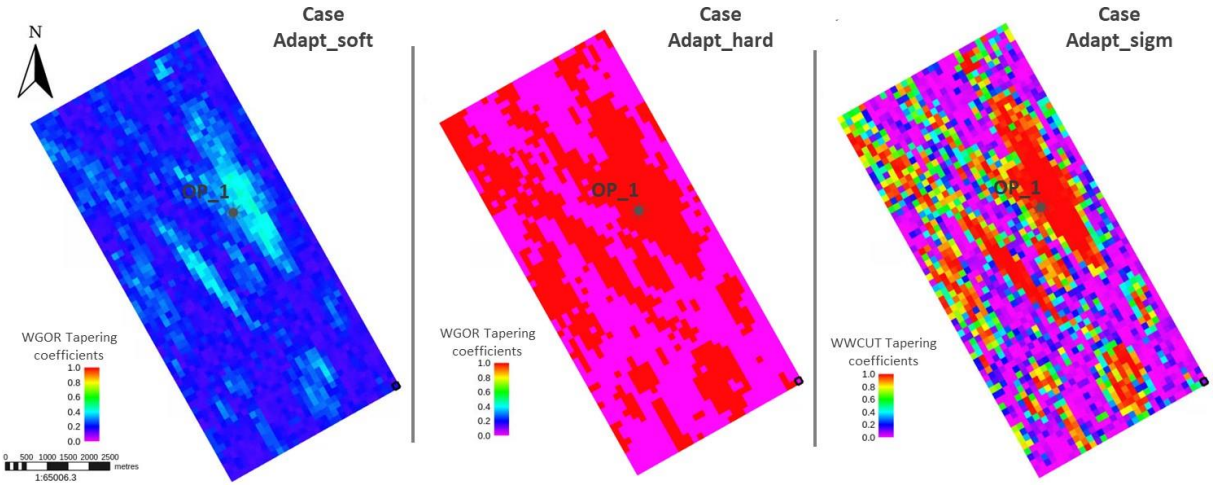

Fig. 33 OP_1 WGOR tapering coefficients over permeability, the three adaptive cases, first iteration, Feb 1st, 2000.

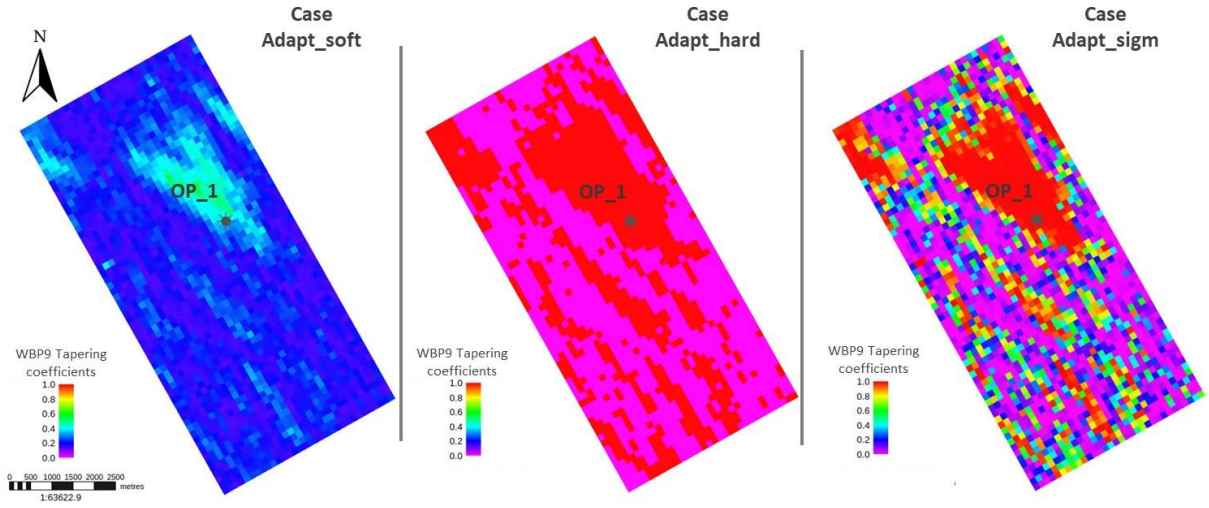

Fig. 34 OP_1 WBP9 tapering coefficients over permeability, the three adaptive cases, first iteration, Feb 1st, 2002.

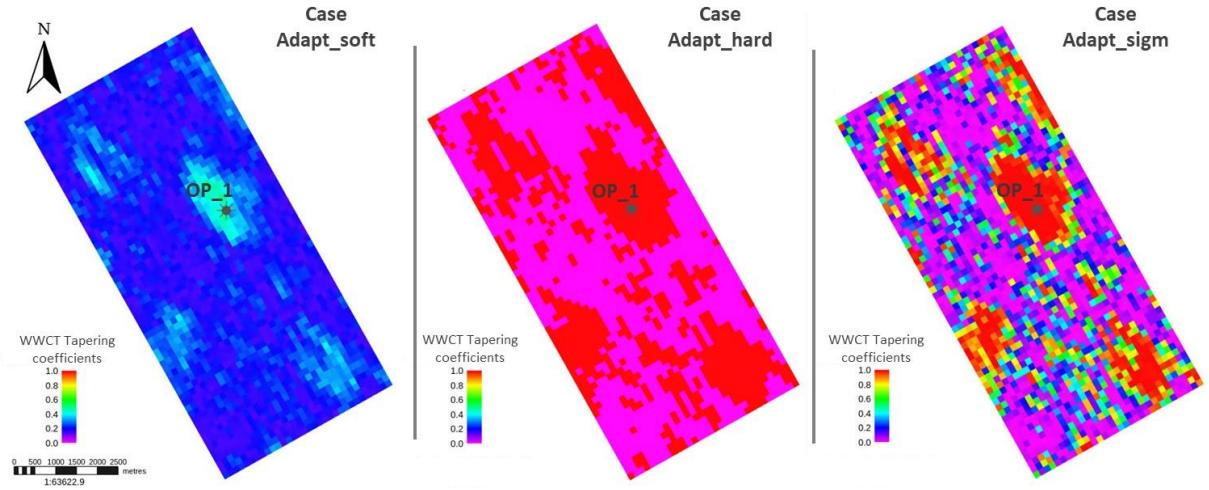

Fig. 35 OP_1 WWCT tapering coefficients over permeability, the three adaptive cases, first iteration, Feb 1st, 2002.

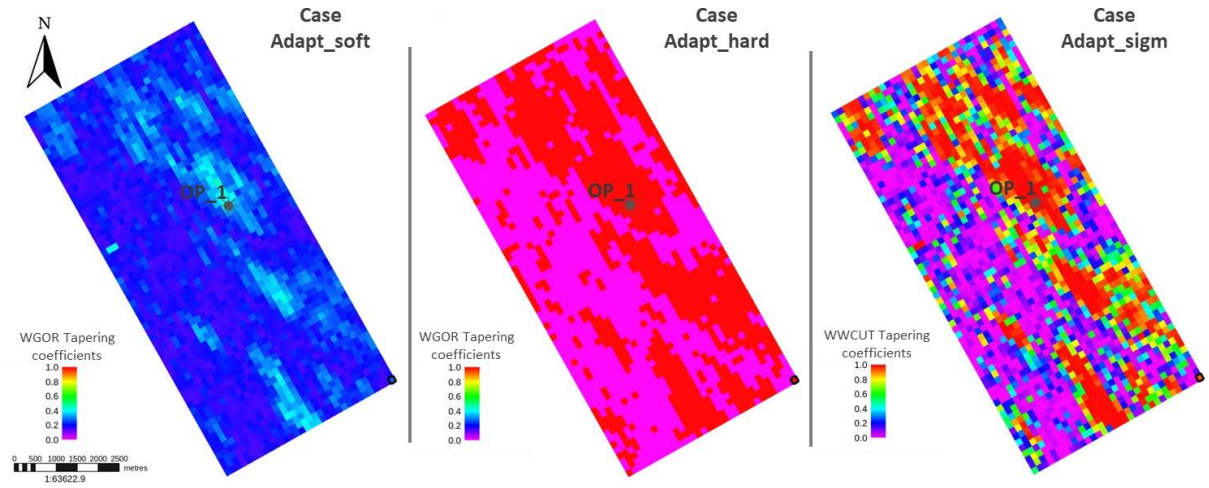

Fig. 36 OP_1 WGOR tapering coefficients over permeability, the three adaptive cases, first iteration, Feb 1st, 2002.

The porosity $mean_{i,j}$, standard deviation $Std_{i,j}$, and $RMS_{i,j}$ of the updated adaptive ensembles are reported in Fig. 37, Fig. 38, and Fig. 39, respectively. The results obtained for the adapt_hard and the adapt_sigm cases are alike. The spatial distribution of the ensemble property $mean_{i,j}$ follows a similar trend in the adapt_hard and the adapt_sigm cases. Fig. 37 shows that the color patterns in the adapt_hard and adapt_sigm cases are like each other. The ensemble property standard deviation, $Std_{i,j}$, reduces more in the adapt_hard and the adapt_sigm cases than in the adapt_soft case (Fig. 38), because the influence degrees of observations over model parameter updates in the adapt_soft case are smoother than the influence degrees of observations in the adapt_hard and adapt_sigm cases. These differences in influence degrees among adapt_soft, adapt_hard and adapt_sigm cases are observed in the tapering coefficient maps in Fig. 31, Fig. 32, and Fig. 33, where the adapt_soft case has smaller tapering coefficients than the adapt_hard and adapt_sigm cases do. The ensemble property standard deviation values, $Std_{i,j}$, for the three adaptive cases (adapt_soft, adapt_hard and adapt_sigm) are larger than zero, which means that none of the adaptive cases present ensemble collapse. In Fig. 38, the reddish, greenish, and blueish colors illustrate areas where the $Std_{i,j}$ values are larger than zero (which would be coloured with magenta). The ensemble porosity $RMS_{i,j}$ values for the three adaptive cases are illustrated in Fig. 39. The ensemble property $RMS_{i,j}$ in the adapt_hard and the adapt_sigm cases are smaller than the $RMS_{i,j}$ values in the adapt_soft case, which means that the adapt_hard and adapt_sigm cases are closer to or more representable of the Truth (Fig. 39) (see Appendix D for the $mean_{i,j}$, $Std_{i,j}$, and $RMS_{i,j}$ adaptive history matching results for permeability).

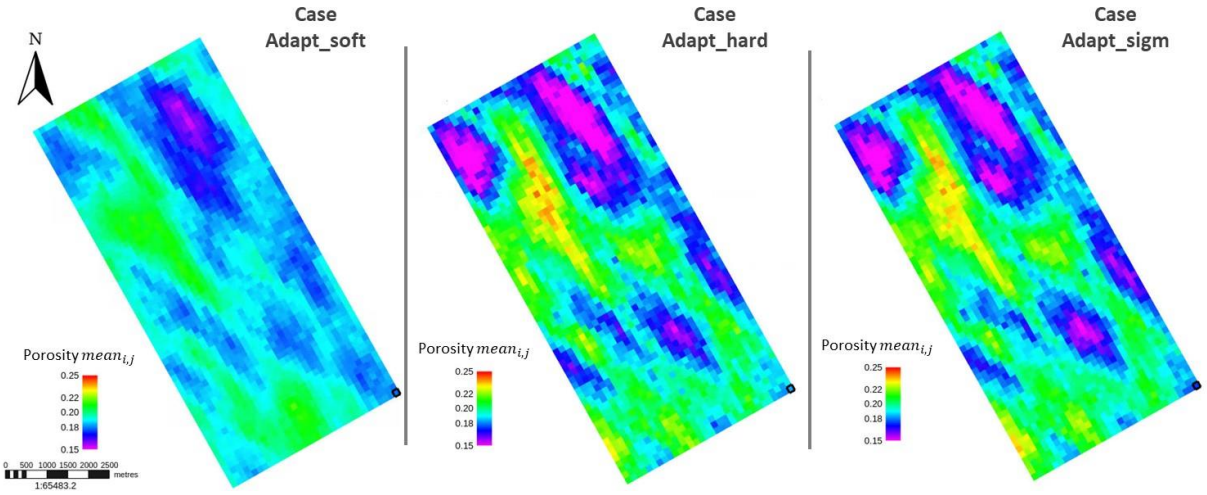

Fig. 37 Updated ensemble porosity mean for three adaptive cases.

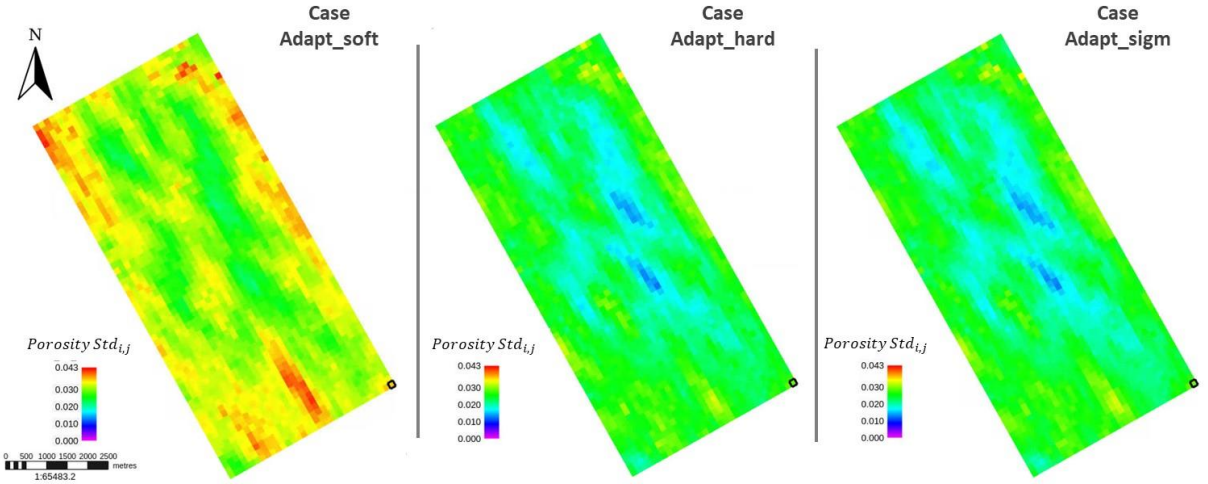

Fig. 38 Updated ensemble porosity standard deviation for three adaptive cases.

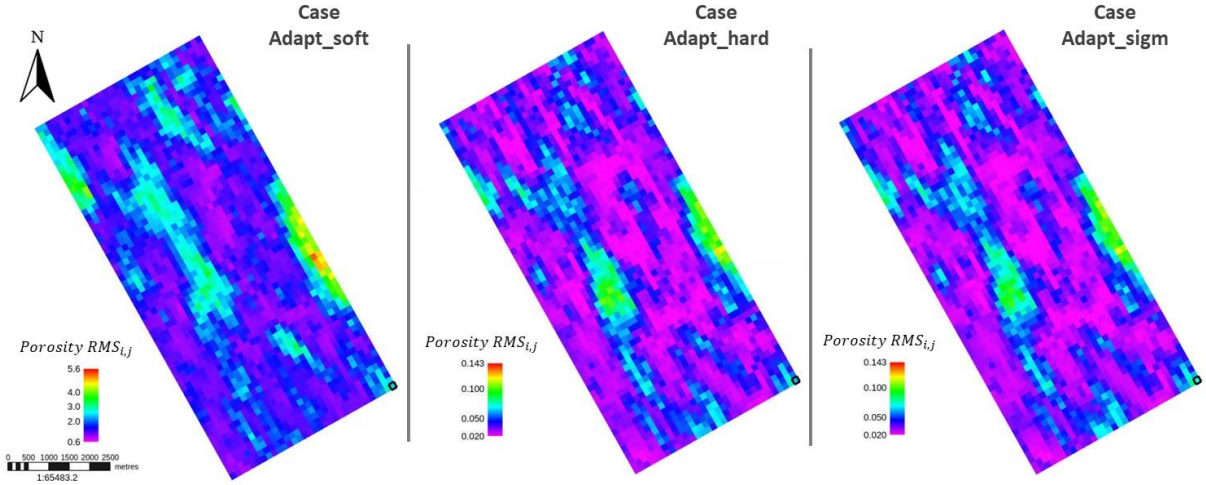

Fig. 39 Updated ensemble porosity RMS for three adaptive cases.

The $RMS_{hist,o}$ and $RMS_{pred,o}$ for the initial, benchmark, and the three adaptive cases are summarized in Fig. 40. The RMS differences between the adapt_hard and the adapt_sigm cases are subtle, and they overperform the benchmark and the adapt_soft cases for all type of observations during history and prediction periods. This is reflected by smaller $RMS_{hist,o}$ and $RMS_{pred,o}$, Fig. 40, for the adapt_hard and the adapt_sigm cases than for the benchmark and the adapt_soft cases.

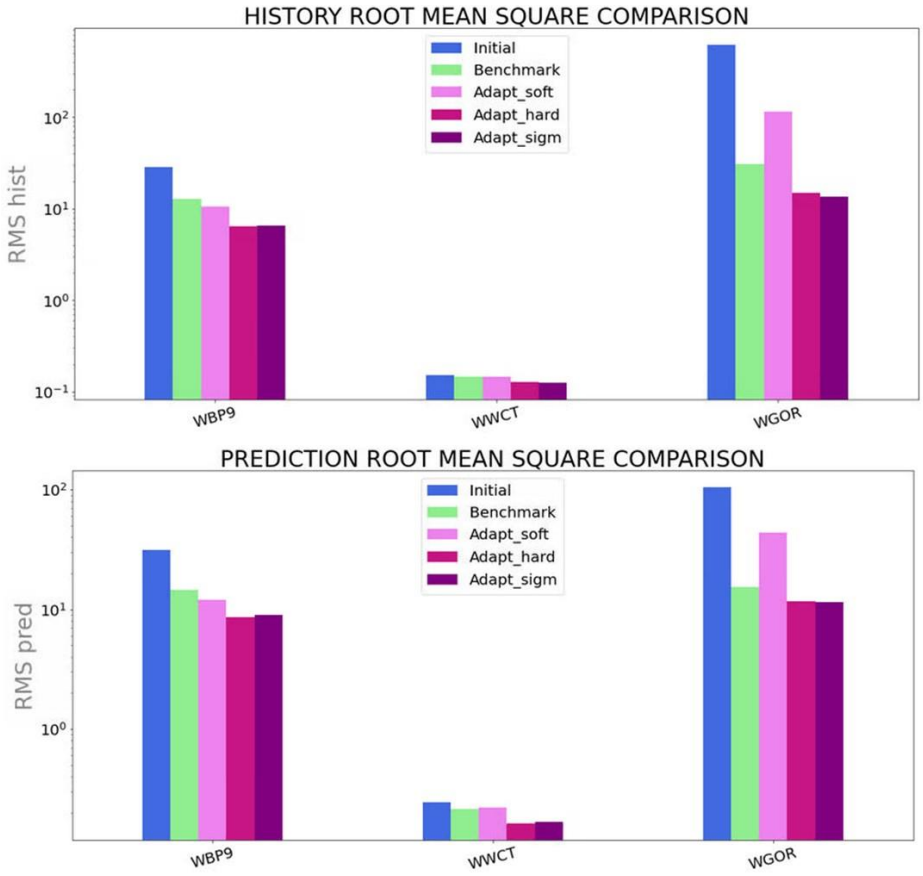

Fig. 40 RMS adaptive cases for production history and prediction period.

In summary, the comparative result analysis of the property $mean_{i,j}$, Fig. 37, indicates that the patterns of the spatial distribution of the model parameters are very alike for the adapt_hard and adapt_sigm cases. The comparative evaluation of the property $Std_{i,j}$, Fig. 38, indicates that the three adaptive cases are reducing the uncertainty in the field model parameters without suffering of ensemble collapse. The comparative result analysis of

$RMS_{i,j}$, Fig. 39, indicates that the adapt_hard and adapt_sigm cases are more representable of the Truth. The $RMS_{hist,o}$ and $RMS_{pred,o}$ results, Fig. 40, for the three adaptive cases, indicate that the adapt_soft underperforms in Reek model, and the other two adaptive cases (the adapt_hard and adapt_sigm) show equal predictivity accuracy for the WBP9, WWCT and WGOR observations. The adaptive localization history matching results for permeability are in Appendix D, and they are consistent with the discussed history matching results for porosity. Based on the results analysis of $mean_{i,j}$, $Std_{i,j}$, $RMS_{i,j}$, $RMS_{hist,o}$, $RMS_{pred,o}$, the selection of the best adaptive localization case stands between the adapt_hard and the adapt_sigm cases. In the thesis, the adapt_sigm case was selected as the best adaptive localization case. The main reason for the selection was that the adapt_sigm case brings the advantage over the adapt_hard case of avoiding discontinuities in the geology due to a hard-tapering rule update, as introduced by Luo and Bhakta (2019). Therefore, the adapt_sigm case is selected as the best adaptive localization case and is recommended both theoretically and practically.

4.5. Comparative analysis of cases

The comparative analysis among the updated ensembles without localization, non-adaptive localization and adaptive localization is performed following the general workflow criteria in Chapter 3, section 3.5. The porosity field and fault multiplier results are outlined in the main body of the thesis' report. The permeability field results are consistent with the porosity field results, and they are included in Appendix E.

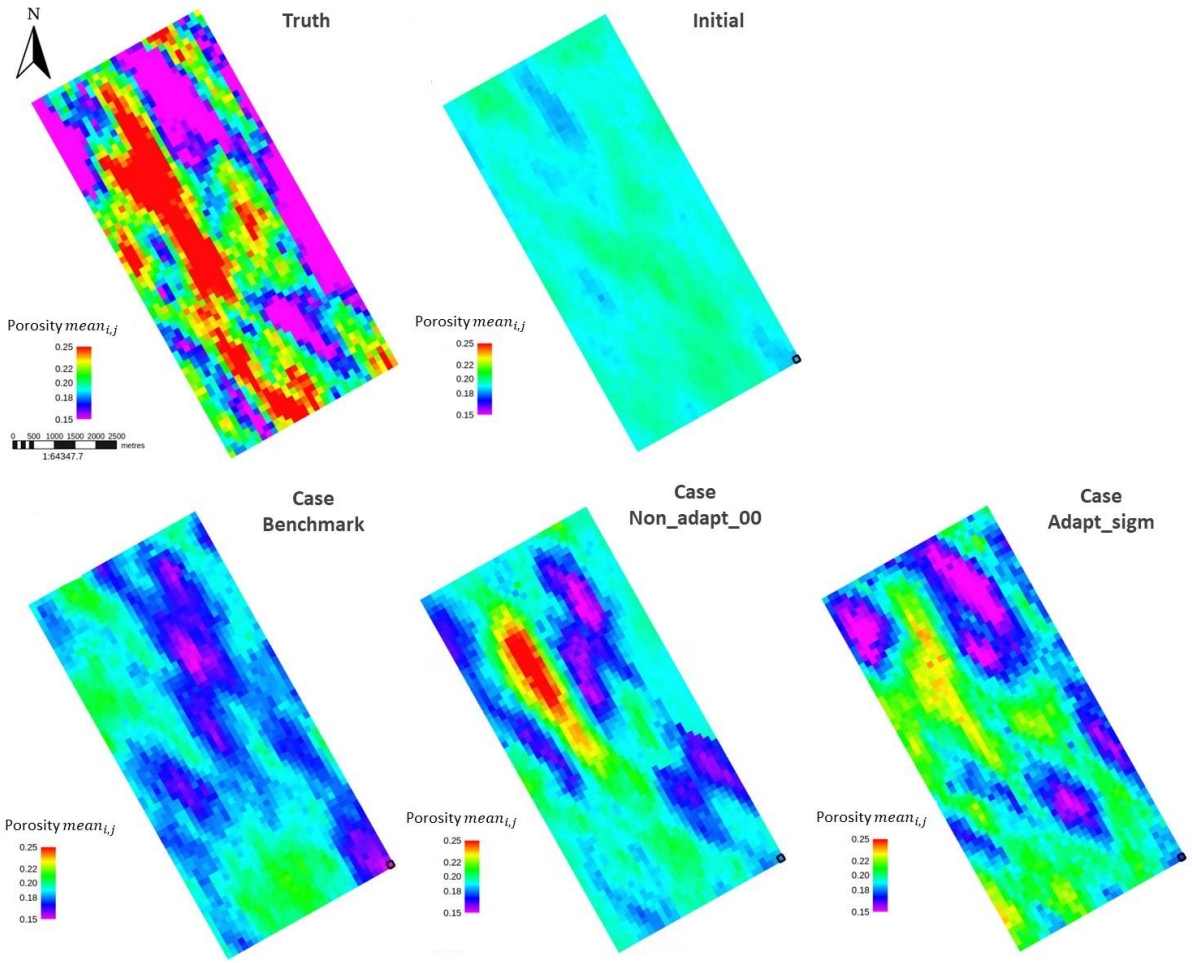

Fig. 41 Comparative analysis of the updated ensemble porosity mean.

Updated ensemble mean for porosity.

The porosity $mean_{i,j}$ for the Truth, initial and the updated ensembles are outlined in Fig. 41. The application of localization, both non-adaptive or adaptive, generates updated porosities with a spatial trend or pattern closer to the Truth than the benchmark case does. The adapt_sigm case overperforms the non_adapt_00 case, because its porosity $mean_{i,j}$ spatial distribution (patterns) are visually more similar to the reservoir spatial distribution of the Truth. This is easily observed while comparing the greenish and magenta areas between the adapt_sigm case and the Truth, which represent the areas of good and poor-quality rock (porosities), respectively. The benchmark case underperforming in this criterion is an indication that it is suffering of filter divergence and spurious correlations.

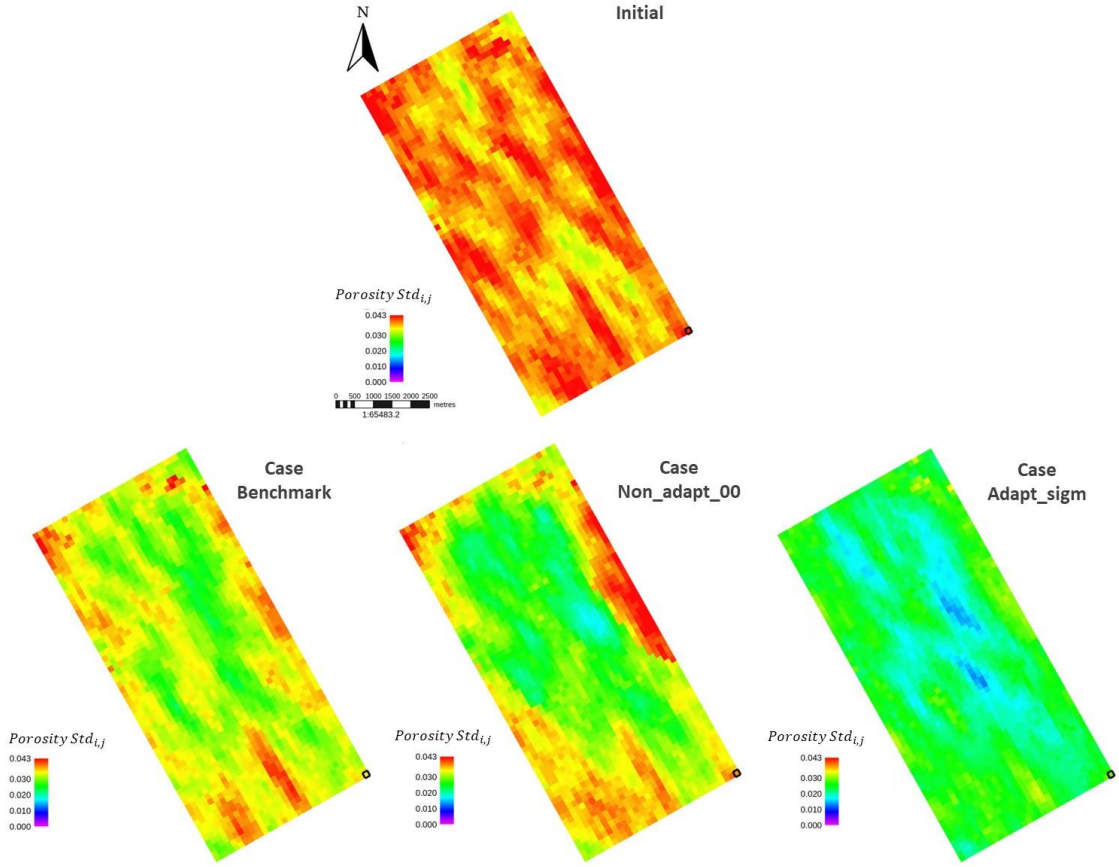

Fig. 42 Comparative analysis of the updated ensemble porosity standard deviation.

Updated ensemble standard deviation for porosity.

The porosity $Std_{i,j}$ for the initial and each of the updated ensembles are outlined in Fig. 42. In general, the ensemble standard deviation values, $Std_{i,j}$, get smaller after history matching. In Fig. 42, the initial ensemble shows more proportion of reddish and yellowish areas than the updated ensembles, which represent larger values of $Std_{i,j}$. The benchmark case performs updates in all gridblocks of the model. The non_adapt_00 case focuses the updates in the central area of the reservoir model and keeps edges of the model with minor or none updates. The adapt_sigm case distributes the updates in all the space of the reservoir model as the benchmark case does, but with a different influence degree of observations over model parameters. The $Std_{i,j}$ in the adapt_sigm case are smaller than in the benchmark case. None of the updated ensembles shows an ensemble collapse

($Std_{i,j} = 0$), which might be represented with magenta color in Fig. 42. An important difference between the non-adaptive and adaptive localization schemes refers to their performance for honoring geological/spatial correlations among properties at different locations. The non-adaptive localization ignores spatial correlations between the model parameters inside and outside the localization regions because it considers only to update the regions with flows/streamlines, whilst the adaptive localization considers spatial correlation in the entire model, because it is a correlation-based method. Unlike the non-adaptive localization, the adaptive localization performs updates in locations without flow that have strong correlation with locations with flows. This is reflected by that the $Std_{i,j}$ are reduced along the edges in the adaptive localization case (the adapt_sigm) in Fig. 42.

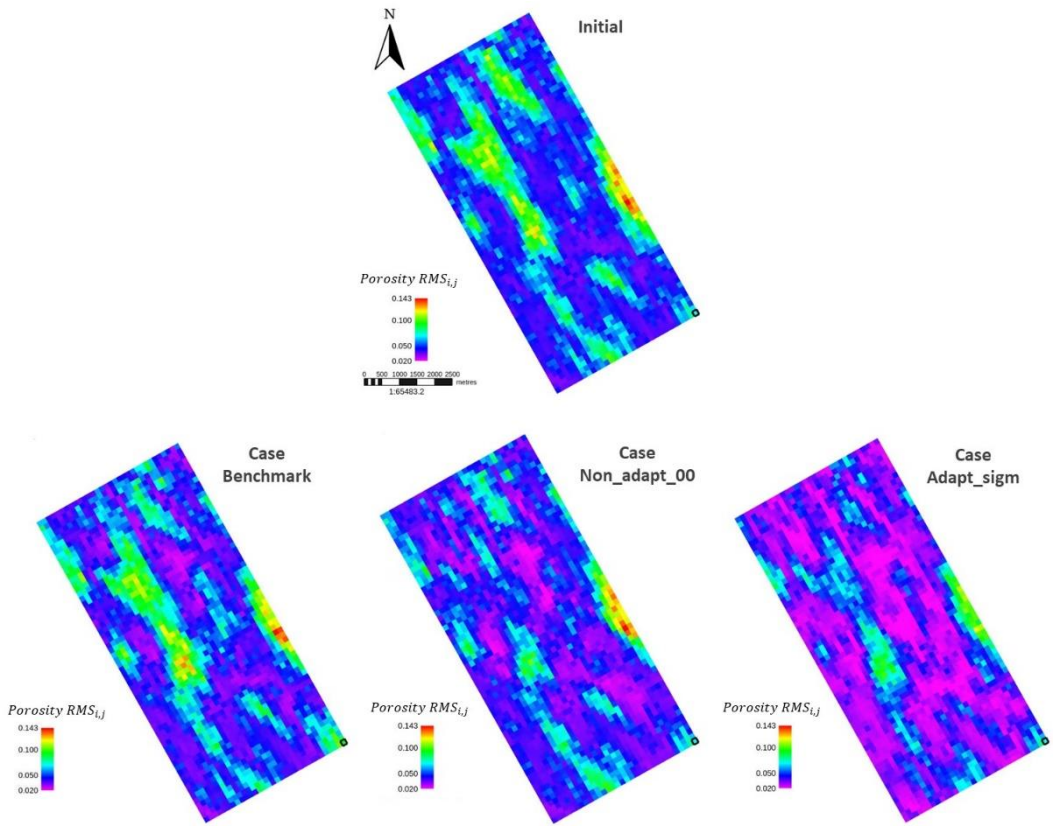

Fig. 43 Comparative analysis of the updated ensemble porosity RMS.

Updated ensemble RMS values against the Truth

The $RMS_{i,j}$ results for the initial and updated ensembles are reported in Fig. 43. Larger proportion of magenta and dark blue colors in the maps represents smaller differences between the updated ensemble and the Truth. Both localization schemes perform better than the benchmark case does. In this criterion, the adapt_sigm case overperforms the non_adapt_00 case with smaller $RMS_{i,j}$, which is represented with larger proportion of magenta color in its $RMS_{i,j}$ map in Fig. 43. The $RMS_{hist,o}$ and $RMS_{pred,o}$ are summarized in Fig. 44. The RMS results for the observations, both during the history or prediction period, are mostly smaller when applying the two types of localization schemes. The RMS values are generally smaller for the adapt_sigm case than for the non_adapt_00 case. The exception occurs in the WWCT observation during the history, where the non-adaptive scheme is overperforming the adaptive scheme. A possible reason for this exception could be that the WWCT is very sensitive to the update in the region with flows and the non-adaptive localization mainly focus and update the region with flows. Another reason could be that during the history matching (three years), the producer wells have late or no water breakthrough, which can impact the history matching quality for WWCT, because there are few data different to zero for conditioning. An opportunity to improve the history matching for WWCT could be to increase the history matching period and include more observations for WWCT after water have broken through in the wells. However, during the prediction of WWCT, in Fig. 44, the $RMS_{pred,o}$ of the non_adapt_00 and adapt_sigm cases are alike. This is observed in Fig. 44 by that the adapt_sigm case overperforms subtly the non_adapt_00 case with smaller $RMS_{pred,o}$ deviations against the Truth.

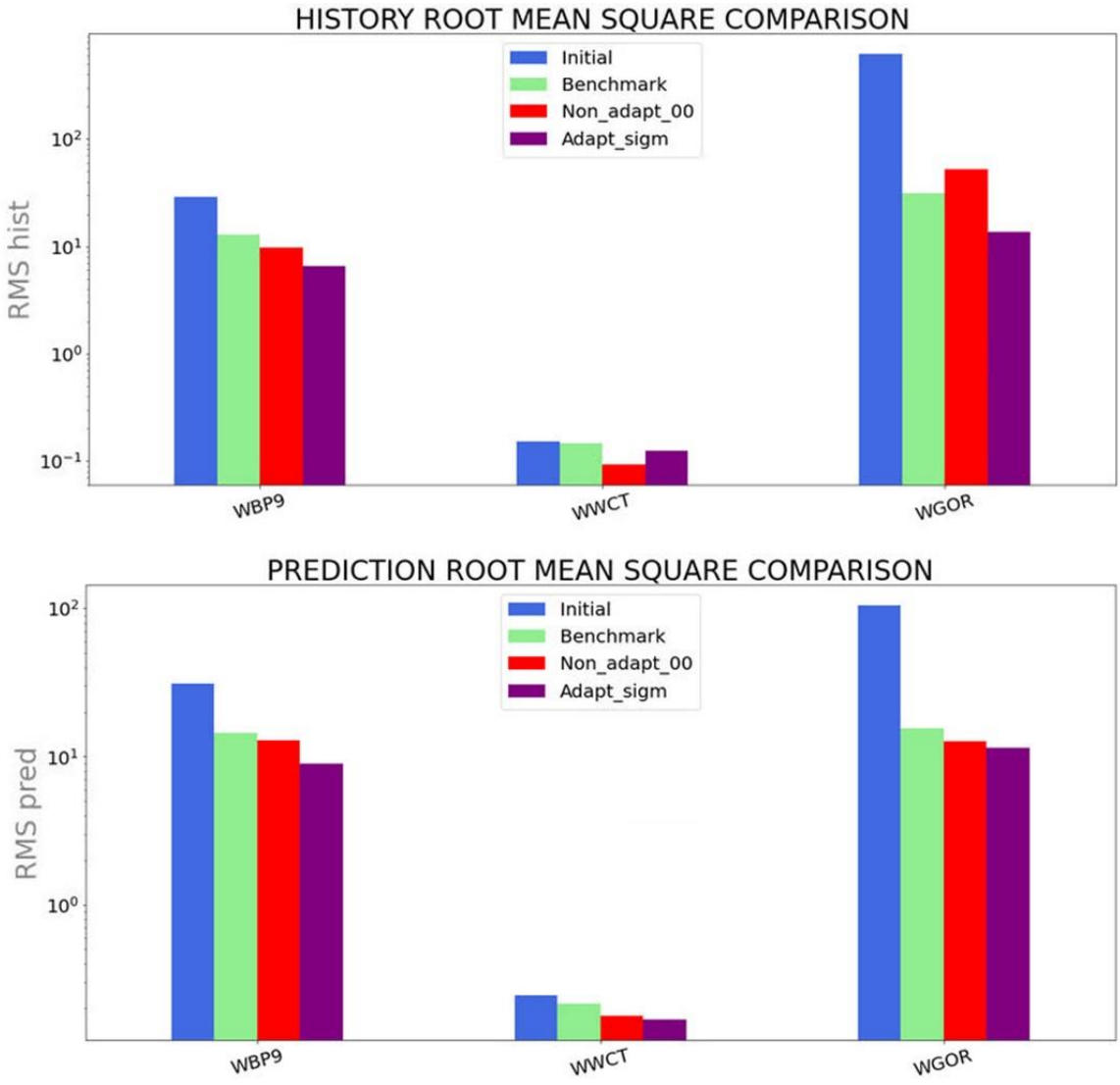

Fig. 44 Observations RMS comparative analysis of the updated ensembles

The RMS_{hist,r_v} and RMS_{pred,r_v} of the production data are outlined in Fig. 45. In this thesis, as introduced in Chapter 3, section 3.5, the production data (WWPR, WOPR, WGPR, WWPT, WOPT, and WGPT) are different than the observations (WBP9, WWCT, WGOR). In this thesis, what is called as the production data are not used for conditioning the history matching. Based on the RMS criterion, the adaptive localization scheme is overperforming benchmark and non-adaptive localization cases with smaller RMS values for all type of production data during history and prediction periods (Fig. 45). The non-adaptive localization scheme is performing like the benchmark for oil and

gas production rate and accumulated volumes, and the non-adaptive localization scheme is underperforming the benchmark case for water production rate and accumulated volumes. The non_adapt_00 case history matches better the WWCT observations than the adapt_sigm case does, Fig. 44, but the non_adapt_00 case underperforms the history matching of the WWPR and WWPT production data in comparison with the adapt_sigm case, Fig. 45. This means that ultimately the adapt_sigm case is more reliable for history matching water production volumes, even though it has larger RMS values for history matching the water cut observations.

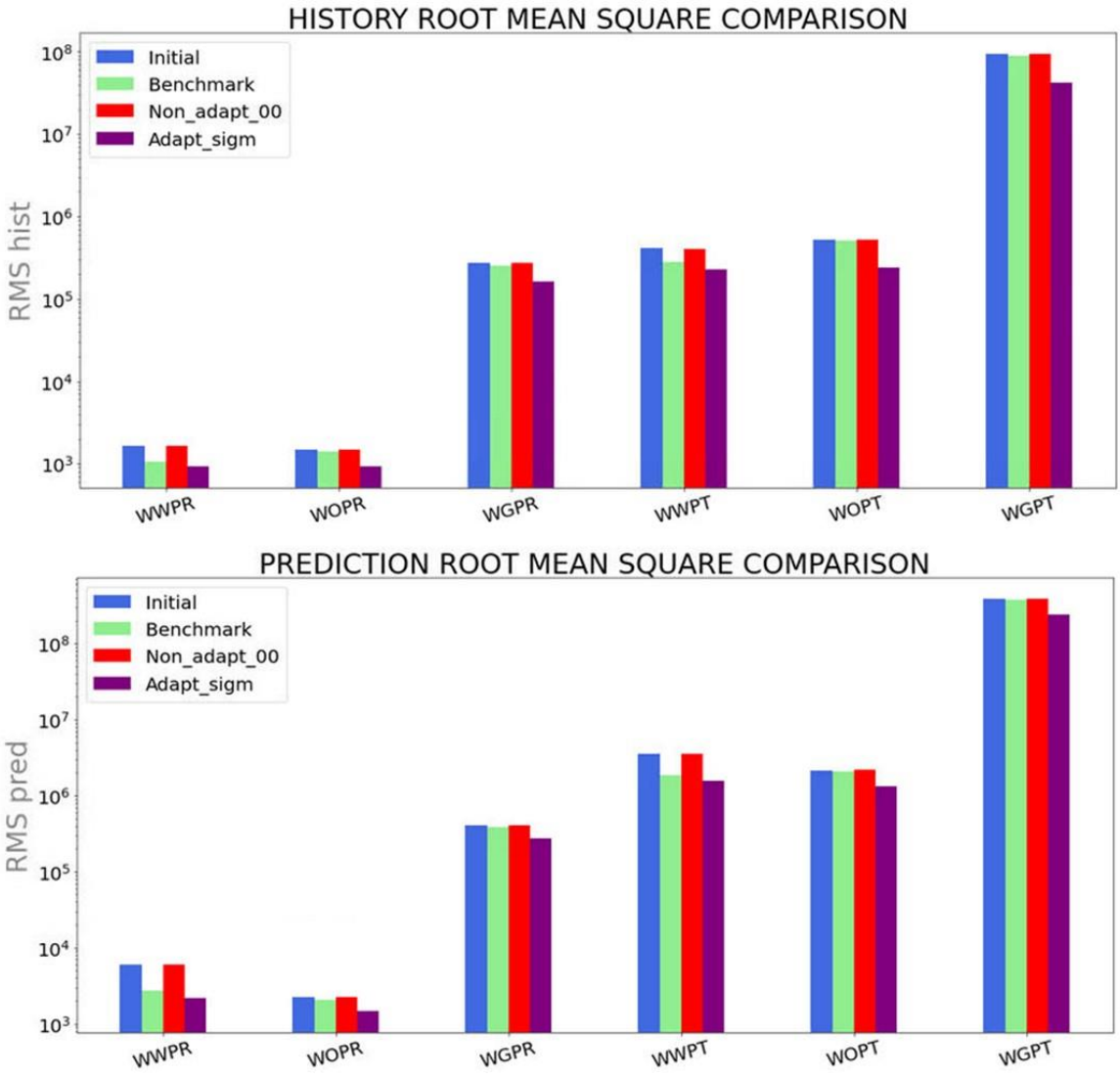

Fig. 45 Production RMS comparative analysis of the updated ensembles.

Updated ensemble RMS values against the initial ensemble

In Fig. 46, the $RMS_{i,j,initial}$ maps indicate the areas that have been updated during history matching. Areas that have not being changed from the initial ensemble are colored in magenta. Areas with stronger changes are colored in yellowish and reddish colors, and areas with moderate changes are colored in light bluish and greenish colors. The benchmark case updates the initial ensemble in the entire model space because there are no magenta areas in its $RMS_{i,j,initial}$ map. Based on the discussed property $mean_{i,j}$ pattern in Fig. 41 and $RMS_{i,j}$ results in Fig. 43, the benchmark case diverges, making property field updates with a different spatial distribution than the Truth, which was qualitative observed in Fig. 41, and quantitative analyzed with the calculation of the $RMS_{i,j}$ in Fig. 43. The non_adapt_00 case localizes the updates by only updating the properties in the regions where the streamlines among injectors and producers occupy. Therefore, the non_adapt_00 case performs most of the update in the nearby of the producer and injectors wells. Unlike the benchmark case, the non_adapt_00 case performs subtle changes to the initial ensemble along the edges of the reservoir model, and areas without streamline flows will get minor or none updates, such as the magenta area in the central panel of Fig. 46. The magenta area represents a hanging wall block of fault F2 that is poorly connected with streamlines to the rest of the reservoir. Thus, the non_adapt_00 case considers that the properties in the magenta area are irrelevant to the observations. The adapt_sigm case changes the initial ensemble in the entire space of the model in different way as benchmark and non_adapt_00 cases did. The adapt_sigm case is a correlation-based approach that tends to honor the spatial property correlations in the reservoir model. The adapt_sigm case differs from the non_adapt_00 case by performing updates towards the edge of the model (including the magenta area in the non_adapt_00

$RMS_{i,j}$ map), which means that these areas might not have significant streamline flows but are still spatially correlated to the areas that have stronger streamline flows. The adapt_sigm case differs from the benchmark case by performing updates in the entire model but driven by physical correlations. The inclusion of the physical correlations in the update of the model parameters solves the benchmark case divergence and make the adapt_sigm case to change assertively the initial ensemble. The adapt_sigm case achieved a property $mean_{i,j}$ spatial distribution closer to the Truth, Fig. 41, and smaller $RMS_{i,j}$, Fig. 43, against the Truth. The adaptive localization scheme proves to be more assertive in terms of accuracy for history matching and prediction in the Reek field.

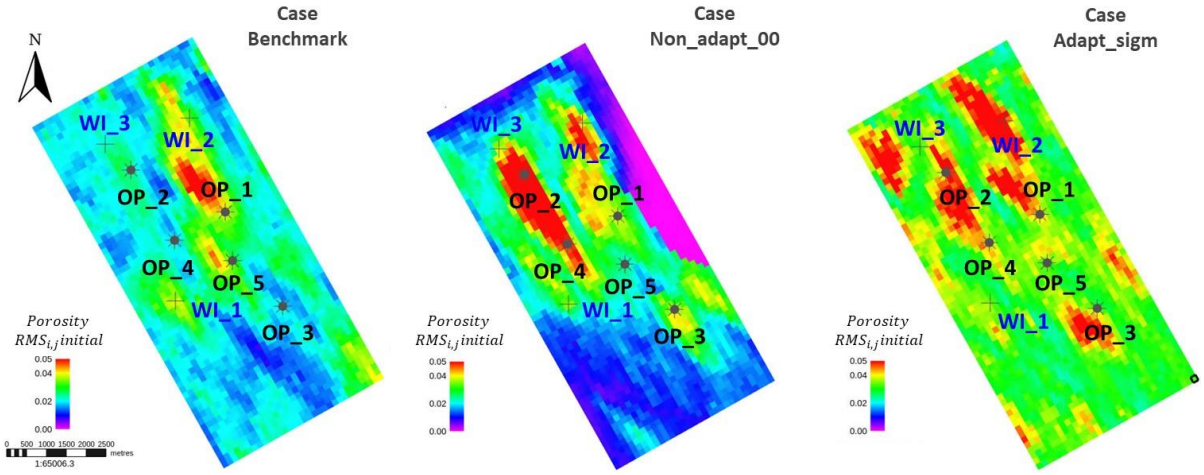

Fig. 46 Comparative analysis of the RMS between Initial and updated ensembles for porosity

Updated ensemble coverage of observations and measurement errors

The non-adaptive and adaptive localization scheme generate an updated ensemble spread narrower than the benchmark ensemble does for simulated observables. The adaptive localization scheme has a similar or better observation coverage and predicting power than the non-adaptive localization scheme. A good observation coverage occurs when the spread of the updated ensemble gets narrower than the spread of the initial ensemble, it is covering the observations and their error bars during the entire history, and

the updated ensemble mean is closer to the observations. In the same way, a good predicting power occurs when the spread of the updated ensemble gets narrower than the spread of the initial ensemble, it is covering the predictions, and the updated ensemble mean is closer to the predictions. In Fig. 47, Fig. 48, and Fig. 49, the non-adaptive and adaptive localization results are illustrated with three dotted lines in red and purple colors, respectively. In each figure, the lower, middle, and upper dotted lines for each localization scheme represent the min, mean, and max values at each time step, respectively. In Fig. 47, for wells OP_1 and OP_2, the WBP9 ensemble spread for initial, and the updated ensembles are shown. The updated WBP9 ensemble results, for both localization schemes, are similar for these two wells. There are none significant differences regarding updated ensemble spread, coverage of observations and measurement error range. However, the non-adaptive localization ensemble mean predicts better in OP_1 and the adaptive localization ensemble mean predicts better in OP_2. In Fig. 48, the updated WBP9 ensemble results for wells OP_3 and OP_5 are illustrated. For these wells, the adaptive localization generates an updated ensemble with a narrower spread than the non-adaptive localization does that still covers the observations and the measurement error range. The mean of the adaptive ensemble matches better the observations during history matching and gets closer to the predictions. For OP_3 and OP_5, the adaptive localization performs a better history matching and prediction than the non-adaptive localization does. In section 4.2, in Fig. 25, for WWCT and WGOR in well OP_3, it was observed an increment of the benchmark updated ensemble spread in comparison with the initial ensemble. In Fig. 49, non-adaptive and adaptive updated ensemble results are added to Fig. 25 to illustrate that both localization schemes solves the observed increment of the benchmark ensemble spread for WWCT and WGOR, in OP_3, which was an indication of ensemble filter divergence. Therefore, the non-adaptive and adaptive localization

results are closer to the observations and predictions than the benchmark case are in Fig. 49. (See Appendix E for visualizing the initial and updated ensembles plots for all wells and all type of observations). The general observations from these plots are that both non-adaptive and adaptive localization tend to show a narrower ensemble spread than the benchmark does for the simulated observables, with better coverage of observations and measurement error bars; and in most of the cases, the adaptive localization performs equally or better than the non-adaptive localization does.

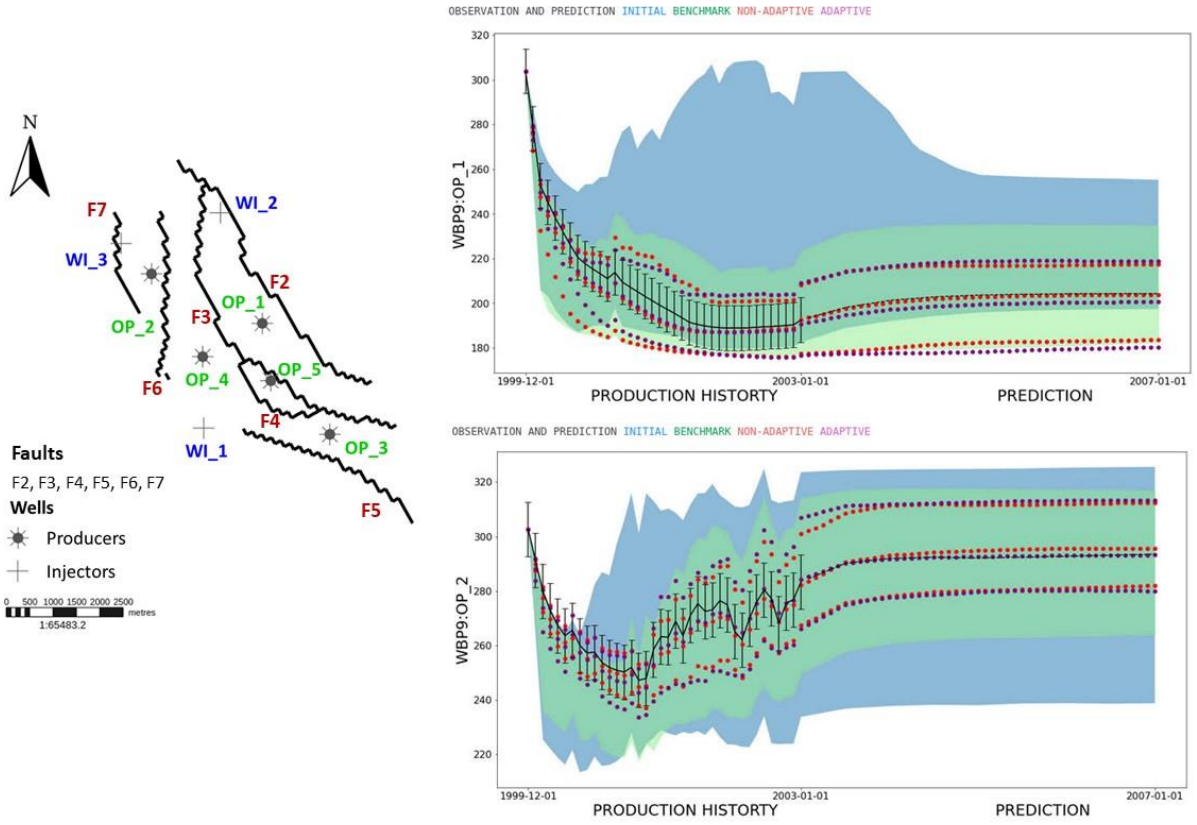

Fig. 47 Coverage comparative analysis: initial and updated ensembles over WBP9 (wells OP_1 and OP_2).

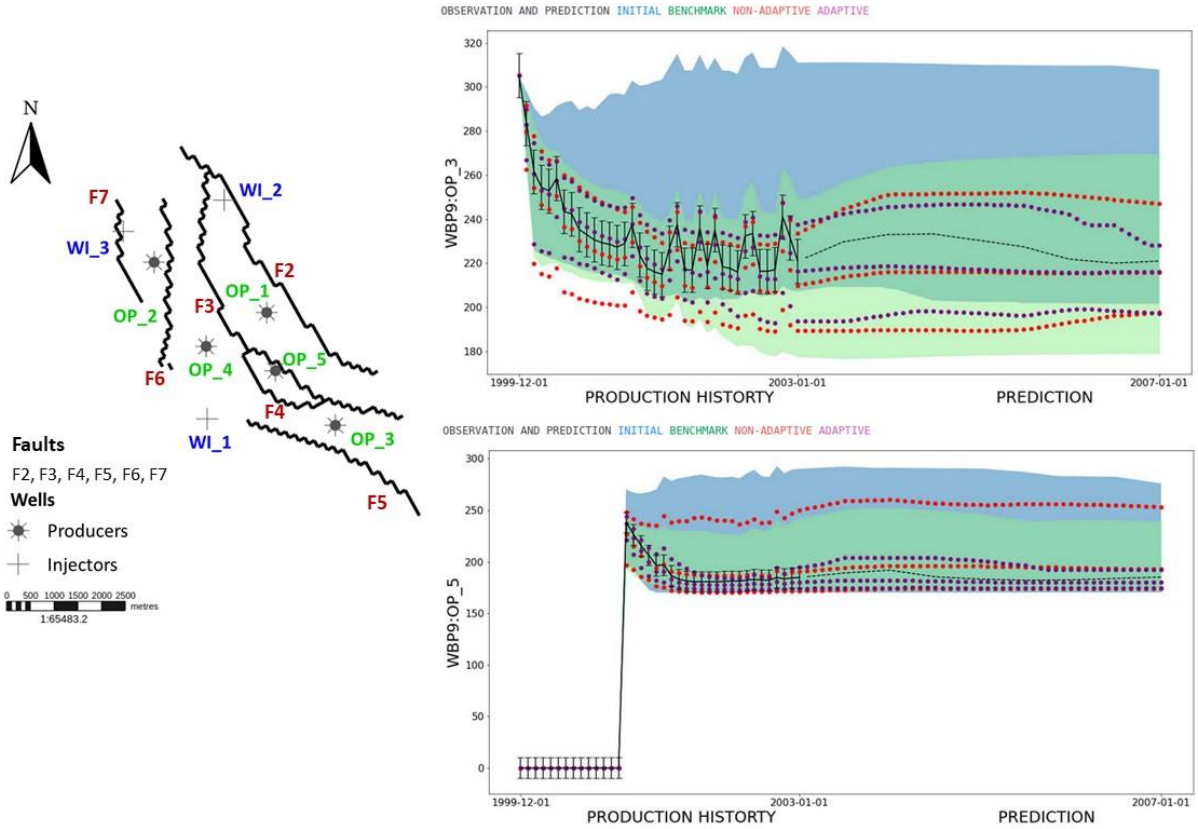

Fig. 48 Coverage comparative analysis: initial and updated ensembles over WBP9 (wells OP_3 and OP_5).

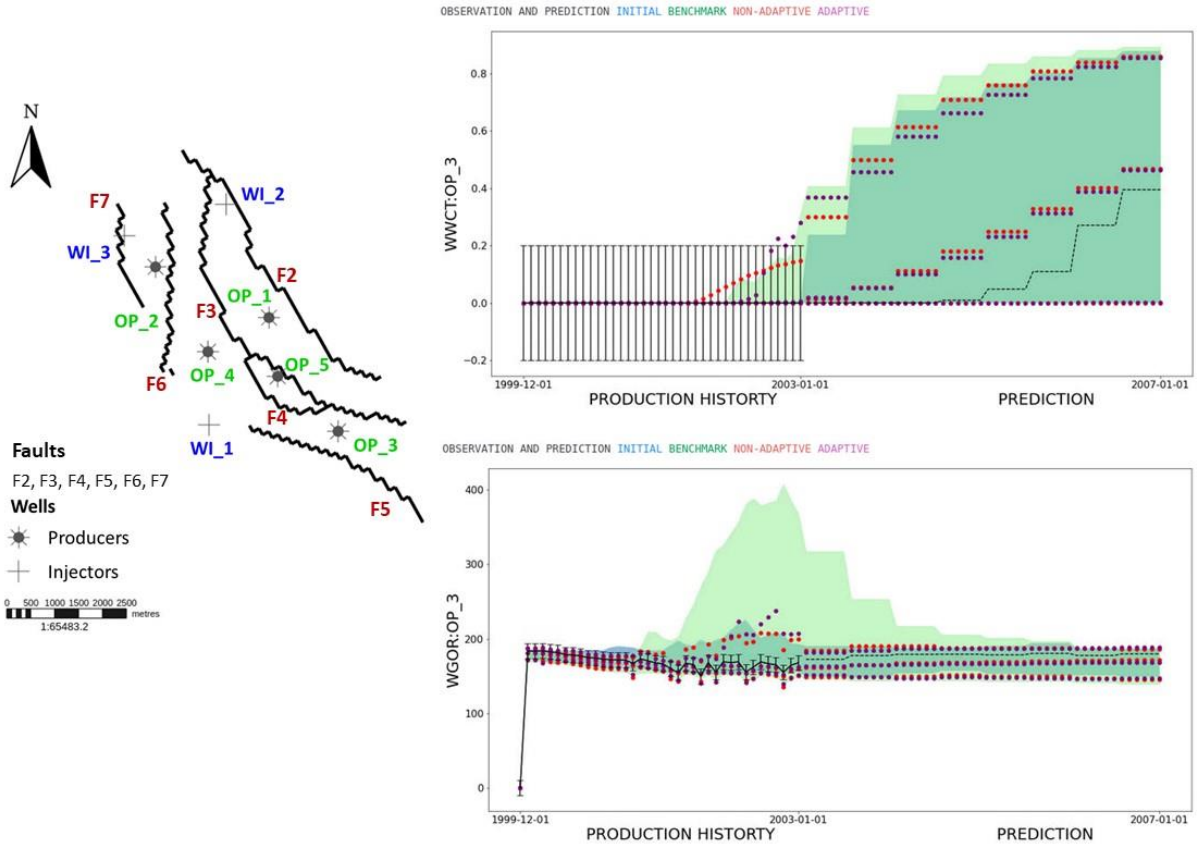

Fig. 49 Coverage comparative analysis: initial and updated ensembles over WWCT, WGOR (well OP_3).

Updated ensemble free parameter distribution

The fault multiplier distributions for the initial and updated ensembles are summarized in Fig. 50 and Fig. 51, and they are compared to the fault multiplier value of the Truth for each fault. In summary, the adaptive localization scheme produces better uncertainty quantification for the seven fault multipliers than the non-adaptive localization does and solves ensemble filter divergence and spurious correlation observed in benchmark case. A good uncertainty quantification of the fault multipliers means that the updated distribution gets narrower, and the updated ensemble median (it is used the median instead of the mean, because the fault multipliers distribution is modelled using a lognormal uniform distribution) gets closer to the Truth. For fault F2, the benchmark and the non_adapt_00 cases reduce incorrectly the ensemble spread by making the ensemble median farther from the Truth. The adapt_sigm case solves the divergence suffered by the benchmark and the non_adapt_00 cases in this fault. The adapt_sigm case median is closer to the Truth. For fault F3, both the adaptive and non-adaptive localization cases overperform the benchmark case. The benchmark ensemble median gets closer to the truth than the initial ensemble, but its ensemble spread is larger than the initial ensemble. This means that the benchmark case suffers of filter divergence. Both localization schemes reduce assertively the fault multiplier standard deviation and generate an updated fault multiplier distribution closer to the Truth. However, the adapt_sigm case overperforms the non_adapt_00 case. For fault F4, the non_adapt_00 and adapt_sigm cases reduce the initial ensemble spread and generate an updated distribution which medians are closer to the Truth than the benchmark median is. The benchmark reduces the ensemble spread of the initial ensemble, but its means is farther from the Truth than the initial ensemble median is. The adaptive localization case overperforms the non-adaptive localization and the benchmark cases. For fault F5, both localization scheme

quantifies similarly the fault multiplier uncertainty, being both better approaches than the benchmark case that diverges to make an ensemble median closer to zero, being the Truth's value equal to 0.3. For fault F6, both localization schemes solve the filter divergence observed in benchmark case, which ensemble spread is wider than the initial ensemble spread. The adaptive localization scheme overperforms the non-adaptive localization scheme because the adaptive updated distribution is narrower, and its ensemble median is closer to the Truth. For F7, both the benchmark case and the non_adapt_00 cases suffer of filter divergence. The benchmark case generates an ensemble spread wider than the initial ensemble, even though its ensemble median is closer to the Truth. The non_adapt_00 case diverges by reducing abruptly the ensemble spread, making the ensemble median closer to zero, which is farther from the Truth. The adaptive localization overperforms benchmark and the non_adapt_00 cases, making the ensemble median closer to the Truth.

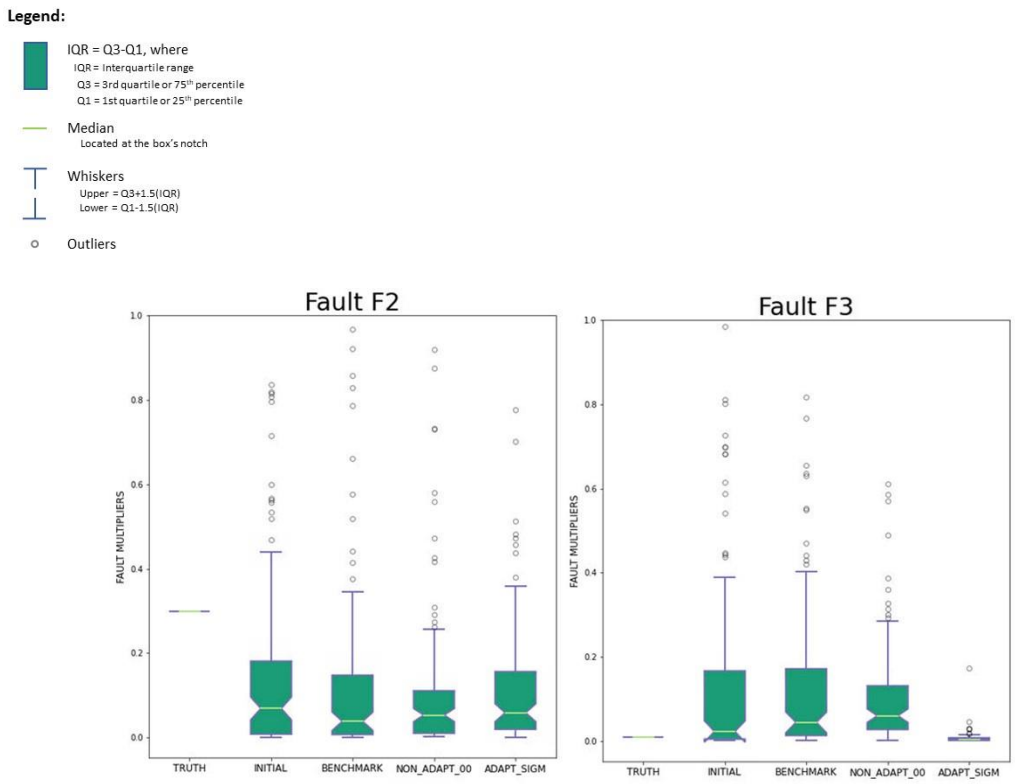

Fig. 50 Fault multiplier distribution comparative analysis among Truth, initial and updated ensembles for F2, F3.

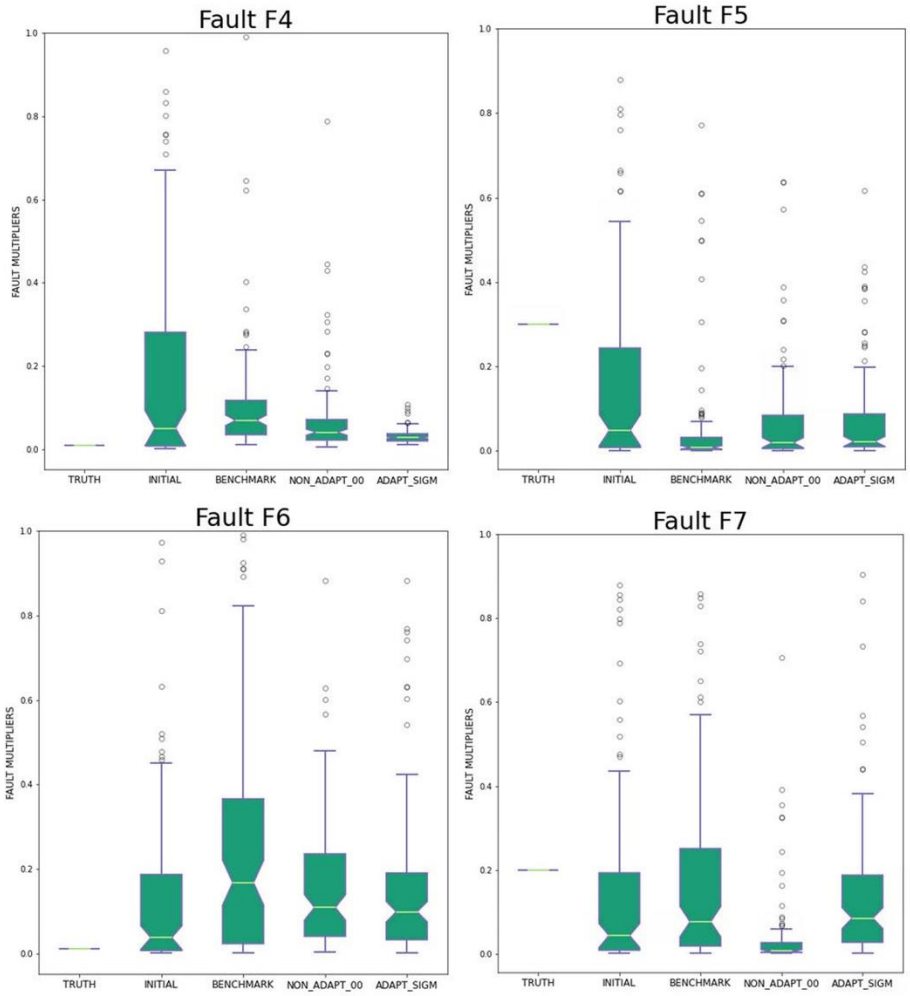

Fig. 51 Fault multiplier distribution comparative analysis among Truth, initial and updated ensembles, other faults.

5. DISCUSSION AND CONCLUSIONS

5.1. Discussion with respect to research questions

Does the application of localization techniques achieve a better history matching than the case without applying any localization techniques in ensemble-based history matching for the Reek Field?

Yes, the application of localization techniques achieved a better history matching for the Reek Field. The benchmark case, the non_adapt_00 and the adapt_sigm history matching results were compared in Chapter 4, section 4.5. Both non-adaptive and adaptive localization schemes generated an updated knowledge closer to the Truth than the benchmark case (i.e., without localization) did. The answer is based on:

- ✓ Both localization techniques achieved closer Truth representation of the field property maps than Benchmark case did (Fig. 41, Fig. E- 1)
- ✓ Both localization techniques achieved smaller root mean squared deviations between the Truth and the updated model parameters than benchmark case did (Fig. 43, Fig. E-3).
- ✓ Both localization techniques achieved smaller root mean squared deviations between the simulated observables and the observations (WBP9, WWCT) than benchmark case did during history period (Fig. 44, upper panel).
- ✓ Both localization techniques achieved better predictivity power than benchmark case did for estimating WBP9, WWCT and WGOR (Fig. 44, lower panel).
- ✓ Both localization techniques achieved better history match and prediction than Benchmark did for WBP9 in OP_3 (Fig. 48, upper panel).

- ✓ Both localization techniques corrected the observed filter divergence in Benchmark case for WWCT and WGOR simulated observables in wells OP_3 (Fig. 49).
- ✓ Both localization techniques solved observed benchmark filter divergence in faults F3, F4, F5, and F6 multiplier distributions (Fig. 50 and Fig. 51). For fault F7, only the adaptive localization scheme solved the benchmark case divergence.

Does the adaptive localization scheme enhance history matching over the non-adaptive localization schemes for the Reek Field?

Yes, the adaptive localization scheme enhanced ensemble-based history matching over the non-adaptive localization scheme for the Reek Field. The adapt_sigm case overperformed the non_adapt_00 case in all the comparative analysis criteria, explained in Chapter 4, section 4.5. The answer is based on:

- ✓ The adaptive localization scheme achieved closer Truth representation of the field property maps than the non-adaptive localization did (Fig. 41, Fig. E- 1)
- ✓ The adaptive localization scheme achieved smaller root mean squared deviations between the Truth and the updated model parameters than the non-adaptive localization did (Fig. 43, Fig. E- 3).
- ✓ The adaptive localization scheme achieved smaller root mean squared deviations between the simulated observables and the observations than the non-adaptive localization did, during history for WBP9 and WGOR (Fig. 44, upper panel).
- ✓ The adaptive localization scheme achieved better predictivity power than the non-adaptive localization did for WBP9, WWCT and WGOR (Fig. 44, lower panel).
- ✓ The adaptive localization scheme achieved better history matching and predictivity of the production data (WWPR, WOPR, WGPR, WWPT, WOPT, WGPT) than the non-adaptive localization did, (Fig. 45, upper and lower panel). In this thesis, the

production data were different than the observations (WBP9, WWCT, WGOR). The production data were not used for conditioning the ensembles.

- ✓ The adaptive localization scheme performed better than the non-adaptive localization scheme for simulating observables closer to the Truth. Fig. 48 shows that the adaptive updated min-max ensemble interval is closer to the Truth than the non-adaptive interval for WWCT and WGOR in well OP_3. Fig. 48 shows that the adaptive updated min-max ensemble interval is closer to the Truth than the non-adaptive interval for WBP9 in wells OP_3 and OP_5.
- ✓ The adaptive localization scheme achieved fault multiplier distributions closer to the Truth than the non-adaptive localization did for all the six faults, Fig. 50 and Fig. 51.

What are the advantages and limitation of using non-adaptive and adaptive localization scheme in practice?

In practice, the adaptive localization scheme brings more advantages than the non-adaptive localization scheme. The advantages of the adaptive localization scheme are the limitations of the non-adaptive localization scheme, and vices versa. The adaptive and non-adaptive localization scheme practical advantages are summarized in Fig. 52. The adaptive localization scheme practical advantages are explained as follows:

- ✓ **Tend to honor reservoir dynamics**: The adaptive localization generates sensitive tapering maps for governing observation influence degree over model parameter updates. The adaptive tapering maps show sensitivity to different correlations among simulated observables and model parameter types, and their variation in time. The sensitive tapering maps in the adaptive localization is an advantage over non-adaptive localization scheme, which uses the same tapering maps in time. Therefore, the adaptive localization tends to honor better the reservoir dynamics.

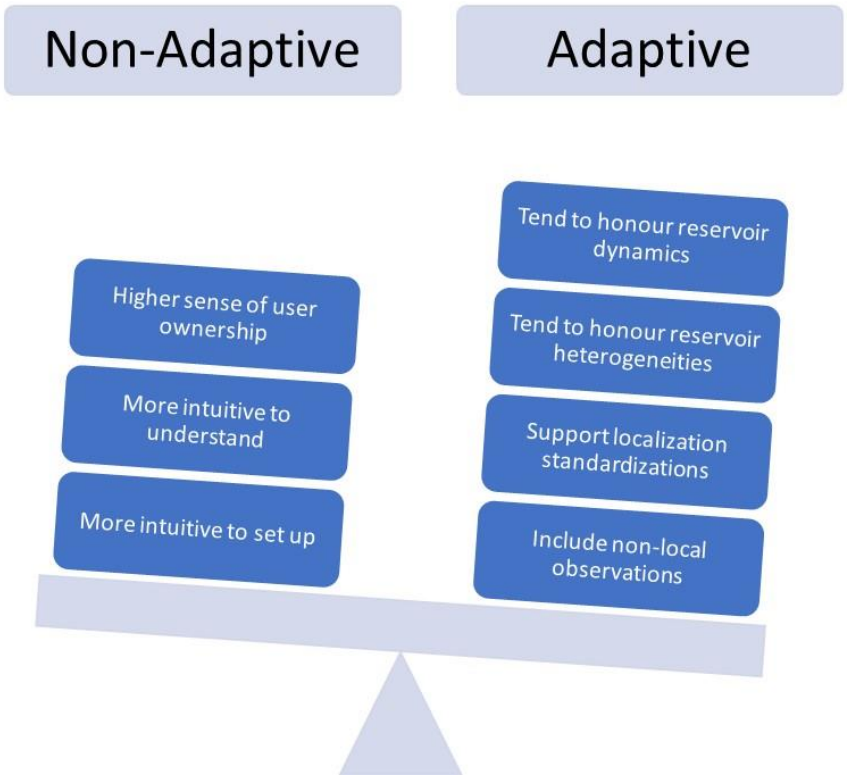

Fig. 52 Advantages of using non/adaptive and adaptive localization scheme in practice.

- ✓ **Tend to honor better reservoir heterogeneities:** In the adaptive localization scheme, the computed tapering coefficients, to relate observations and model parameters, have multimodal distributions (Fig. 31, Fig. 32, Fig. 33, Fig. 34, Fig. 35, Fig. 36) that tend to honor better the geological anisotropies in the reservoir. The non-adaptive localization scheme consists of tapering coefficients with unimodal distribution (Fig. 26, Fig. C- 1, Fig. C- 2, Fig. C- 3, Fig. C- 4) that weights observations influence degree in proportion to closeness of the model parameters to the location of observations. Therefore, the update step in the adaptive localization scheme suits better the reservoir model heterogeneities than the non-adaptive localization scheme does.
- ✓ **Support localization standardization:** The adaptive localization scheme defines the tapering maps for governing observation influence degree over model parameter

updates with an automated process, in which users just need to indicate the model parameters to be updated. This automation in generating the adaptive tapering maps brings the advantage of supporting less experienced users and avoid differences between users. Unlike the adaptive localization scheme, the non-adaptive localization scheme depends on the user's preference to calculate the distance-based regions. Therefore, the adaptive localization scheme supports standardization in the implementation of localization in ensemble-based history matching.

- ✓ **Include non-local observations:** In the thesis, the observations are local, and therefore, they have a 3D coordinate in the reservoir model. However, non-local observations are used in other modern applications as mentioned in Chapter 2, section 2.2. The possibility to include non-local observations is an advantage that adaptive localization scheme has over non-adaptive localization scheme.

The non-adaptive localization scheme practical advantages in Fig. 52 are:

- ✓ **Higher sense of user ownership:** The non-adaptive localization scheme easily allows the user to make changes to the tapering maps for governing observation influence degree over model parameter updates based on user-reservoir dynamics knowledge. The user-interaction to adjust the tapering maps creates a sense of user ownership in the history matching. In the adaptive localization scheme, the tapering maps are generated automatically, internally by the software, and they are not straight forward visualized, interpreted and edited by the user. If the user wants, the adaptive tapering maps can be exported from the software for visualization, interpretation, and edition. However, the exporting step has not being yet implemented in a straightforward and user-friendly way. If the adaptive localization scheme is implemented fully automatically, it will become a black box, and the user will lose

their understanding of the tapering map changes to govern the observation influence degree over model parameters. In practice, the sense of user ownership is an advantage of non-adaptive localization scheme over the adaptive localization scheme, if the latter is used as a black box.

- ✓ **More intuitive to understand:** In the non-adaptive localization scheme, the tapering maps to govern the observations-model parameters influence degree are based on a user pre-study on model reservoir dynamics. In the adaptive localization scheme, the tapering maps are based on correlations among observations and model parameters. The spatial regions for updating of the non-adaptive localization scheme are more intuitive to most engineers than correlations. Although correlations of the adaptive localization scheme embed reservoir dynamics, the understanding and interpretation of the correlations are not as straightforward as spatial regions are.
- ✓ **More intuitive to set up:** The non-adaptive localization scheme allows the user to set up the observation-model parameter influence degree, just based on classical reservoir engineering knowledge (e.g., drainage areas, streamline flows, compartmentalization, vertical connectivity). The adaptive localization scheme is automated, but still requires the user to choose the most efficient tapering rule (soft, sigm, hard) and to tune the threshold values to improve history matching. The learning process for choosing the tuning factor and its meaning is less intuitive for most engineers and requires building a learning curve of the methodology proposed by Luo and Bhakta (2019), explained in Chapter 3, section 3.4.

The adaptive localization scheme has been demonstrated to be a better approach to guide the model parameter updates than the non-adaptive localization scheme. The adaptive localization scheme tends to honor better the reservoir dynamics and heterogeneities. However, the adaptive localization scheme requires to create tools for facilitating the user

learning curve of the method's theory and the adaptive correlation coefficient sensitivities, and ultimately for developing user history matching ownership when implementing adaptive localization.

What are the recommended practices of implementing non-adaptive and adaptive localization schemes?

In practice, the general workflow explained in Chapter 3, section 3.5 could be applied as follow:

Section i. **Generation of the initial ensemble:** Collect the prior knowledge of the sensible model parameters for the reservoir modelling and their uncertainties from a multidisciplinary team. The initial ensemble should consider wide ranges of possible values of the model parameters and cover the selected observations and their measurement error bars, for avoiding over-confidence (i.e., too narrow ranges of possible values of the model parameters).

Section ii. **Development of history matching without localization:** Perform the history matching case without localization with Workflow 1. Evaluate the history matching results by observing and interpreting the updated model parameters distribution and the updated ensemble simulated observables (e.g., property $mean_{i,j}$ in Fig. 22, property $Std_{i,j}$ in Fig. 42, changes in the initial ensemble in Fig. 46, property distribution box plots in Fig. 23, updated ensemble coverage and spread in Fig. 24 and Fig. 25, data match quality with $RMS_{hist,o}$ and $RMS_{pred,o}$ in Fig. 30. Identify the presence of ensemble-based history matching challenges: ensemble collapse, spurious correlation, or filter divergence. The ensemble collapse is identified when

the ensemble spread reduces to zero for the model parameter's distribution or simulated observables' forecast. Spurious correlation and filter divergence can be identified when model parameters which are not physically related to observations get updated, or when the updated ensemble shows good observation coverage and small $RMS_{hist,o}$ and $RMS_{pred,o}$ in some wells, but bad observation coverage and large $RMS_{hist,o}$ and $RMS_{pred,o}$ in other wells of the field. If the ensemble-based history matching results show indication of ensemble collapse, filter divergence or spurious correlation, then apply localization schemes.

Section iii. **Selection of the best non-adaptive localization case:** Perform a multidisciplinary brainstorming for defining the non-adaptive cases. The thesis work proposes as reference Workflow 3 for defining the tapering maps based on streamlines simulation. In practice, the approach for defining the non-adaptive localization regions is tailored to each application. For example, if reservoir compartmentalization exits and isolated blocks have been proven in the field, then the distanced-based localization region could be the compartment area. Another example can be, if layers are not connected vertically in the field, then the distance-based localization can be to make that those observations related to a layer should only update model parameters in this layer of the field. As proposed in Workflow 3, streamline simulations are useful in waterflooding fields, with which the localization regions will be based on the flows among injectors and producers. Perform the non-adaptive localization history matching following Workflow 2. Select the best non-adaptive case comparing the results of the ensemble mean $mean_{i,j}$ (Fig. 27), standard

deviation $Std_{i,j}$ (Fig. 28), root mean square deviations $RMS_{i,j}$ (Fig. 29), the root mean square deviation during history $RMS_{hist,o}$ and the root mean square deviation in prediction $RMS_{pred,o}$ (Fig. 30), the root mean square deviation against the initial ensemble $RMS_{i,j,initial}$ (Fig. 46). When working with a real field, the property $RMS_{i,j}$ cannot be defined as did in the thesis, where Truth porosities and permeabilities were known. In real application, property RMS comparison can be calculated against measured property data (e.g., core data, well log data). In the thesis, $RMS_{pred,o}$ was calculated using the Truth model predictions. In real applications, $RMS_{pred,o}$ could be computed for a period in the history not used for conditioning.

Section iv. **Selection of the best adaptive localization case:** The thesis proposes Workflow 4 for computing the tapering maps based on Luo and Bhakta (2019). Observe and interpret the changes in the adaptive tapering maps. Identify if they tend to honor the reservoir dynamics and heterogeneities in the field. Perform the adaptive localization history matching following Workflow 2. Select the best adaptive case based on the results of the ensemble mean $mean_{i,j}$ (Fig. 37), standard deviation $Std_{i,j}$ (Fig. 38), vertical average root mean square deviations $RMS_{i,j}$ (Fig. 39), the root mean square deviation during history $RMS_{hist,o}$ and the root mean square deviation in prediction $RMS_{pred,o}$ (Fig. 40). Evaluate if applying tunning factors in the tapering rules could improve the history matching results. In the thesis, the tuning factors used were 0.1, 0.1, and 1 for the adapt_soft, adapt_hard, and adapt_sigm, respectively. When working with a real field,

the property $RMS_{i,j}$ cannot be defined as did in the thesis, where Truth porosities and permeabilities were known. In real application, property RMS comparison can be calculated against measured property data (e.g., core data, well log data). In the thesis, $RMS_{pred,o}$ was calculated using the Truth model predictions. In real applications, $RMS_{pred,o}$ could be computed for a period in the history not used for conditioning.

Section v. **Comparative analysis among updated ensembles:** Perform the comparative analysis among the initial, updated ensembles with and without localization applying Workflow 5. Select the best ensemble-based history matching after the comparative analysis of all the criteria explained in Chapter 3, section 3.5: updated ensemble mean for field properties $mean_{i,j}$ (Fig. 41), updated ensemble standard deviation for field properties $Std_{i,j}$ (Fig. 42), updated ensemble RMS values: $RMS_{i,j}$, $RMS_{hist,o}$, $RMS_{pred,o}$ RMS_{hist,r_v}, RMS_{pred,r_v}, $RMS_{i,j,initial}$ (Fig. 43, Fig. 44, Fig. 45, Fig. 46), updated ensemble coverage of observations and measurement errors (Fig. 47, Fig. 48, Fig. 49), and updated ensemble free parameter distribution (Fig. 50, Fig. 51).

5.2. Conclusions

- ✓ The novelty of the thesis is that it investigated the practical pros and cons of applying the adaptive localization scheme for ensemble-history matching reservoir simulation models and proposed a general workflow to guide localization implementation and evaluation.
- ✓ The general workflow was proposed and elaborated in the five sections: i) Generation of the initial ensemble, ii) Development of the benchmark case, iii) Selection of the

best non-adaptive localization case, iv) Selection of the best adaptive localization case, v) Comparative analysis among updated ensembles. The workflow was implemented on the Reek model, and the results were analyzed and discussed.

- ✓ The benchmark case was the ensemble-based history matching with ES-MDA (three iterations and the inflating factors, $\alpha_{l+1} = 7, 3.5, 1.75$) and without any localization. The non_adapt_00 was the best non-adaptive localization case which was based on non-adaptive studies performed by Devegowda et al.(2007), Arroyo-Negrete et al.(2008), Emerick and Reynolds (2010), and Luo et al. (2019). The adapt_sigm was the best adaptive localization case which was based on the methodology developed by Luo and Bhakta (2019).
- ✓ The thesis demonstrated that the ensemble-based history matching without localization, benchmark case, suffered from filter divergence and spurious correlation for the Reek field.
- ✓ The thesis demonstrated that localization techniques, both the non-adaptive scheme and adaptive scheme, enhanced ensemble-based history matching for the Reek field.
- ✓ The thesis demonstrated that the history matching with the adaptive localization scheme overperformed the history matching with the non-adaptive localization scheme for the Reek field. Therefore, the adaptive localization scheme can contribute to improving uncertainty quantification and eventually decision quality.
- ✓ The workflow developed and proposed in the thesis has been demonstrated to be useful for comparing ensemble-based history matching schemes and results for the Reek field. The workflow is practical and general and thus can be applied for quantitative and qualitative analysis of history matching results for other fields.

5.3. Further work

- ✓ Incorporate the adaptive localization scheme in Equinor's FMU tools.
- ✓ Test and improve the general workflow for non-adaptive and adaptive localization schemes for other cases (e.g., real fields, seismic data assimilation, and facies updating).
- ✓ Develop and implement a practical method to visualize and analyze the changes in the adaptive localization tapering maps during history matching to facilitate understanding and interpretation of the adaptive localization tapering maps and avoid using adaptive localization scheme as a black box.
- ✓ Develop a tutorial on adaptive localization scheme for users to better understand the method's theory and application.

References

Aanonsen, S. I., G. Nævdal, D. S. Oliver, A. C. Reynolds, and B. Vallès, 2009, The Ensemble Kalman Filter in Reservoir Engineering -- a Review: Society of Petroleum Engineers Journal, SPE 117274, v. 14, no. 03, p. 393–412, doi:10.2118/117274-PA.

About us - Norce, n.d.: accessed May 7, 2022, https://www.norceresearch.no/en/about-us.

Arroyo-Negrete, E., D. Devegowda, A. Datta-Gupta, and J. Choe, 2008, Streamline-Assisted Ensemble Kalman Filter for Rapid and Continuous Reservoir Model Updating: SPE Reservoir Evaluation & Engineering, SPE-104255-PA, p. 15, doi:10.2118/104255-PA.

Bianco, A., A. Cominelli, L. Dovera, G. Nævdal, and B. Vallès, 2007, History Matching and Production Forecast Uncertainty by Means of the Ensemble Kalman Filter: A Real Field Application: doi:10.2118/107161-MS.

Chen, Y., and D. S. Oliver, 2011, Ensemble Randomized Maximum Likelihood Method as an Iterative Ensemble Smoother: Mathematical Geosciences, v. 44, no. 1, p. 1–26, doi:10.1007/s11004-011-9376-z.

Chen, Y., and D. S. Oliver, 2013, History Matching Of The Norne Full Field Model Using An Iterative Ensemble Smoother, *in* EAGE Annual Conference & Exhibition incorporating SPE Europec, London, UK: SPE, doi:10.2118/164902-MS.

Chen, Y., and D. S. Oliver, 2017, Localization and regularization for iterative ensemble smoothers: Computational Geosciences, v. 21, no. 1, p. 13–30, doi:10.1007/s10596-016-9599-7.

Devegowda, D., E. Arroyo, A. Datta-Gupta, and S. G. Douma, 2007, Efficient and Robust Reservoir Model Updating Using Ensemble Kalman Filter With Sensitivity-Based Covariance Localization, *in* SPE Reservoir Simulation Symposium: OnePetro, doi:10.2118/106144-MS.

ECLIPSE Industry Reference Reservoir Simulator, n.d.: accessed December 6, 2021, https://www.software.slb.com/products/eclipse.

Emerick, A., and A. Reynolds, 2010, Combining sensitivities and prior information for covariance localization in the ensemble Kalman filter for petroleum reservoir applications: 2011 Computational Geosciences Journal, v. 15, no. 2, p. 251–269, doi:10.1007/s10596-010-9198-y.

Emerick, A. A., and A. C. Reynolds, 2012, Ensemble smoother with multiple data assimilation: Computers & Geosciences, v. 55, p. 3–15, doi:10.1016/j.cageo.2012.03.011.

Emerick, A. A., and A. C. Reynolds, 2013, History-Matching Production and Seismic Data in a Real Field Case Using the Ensemble Smoother with Multiple Data Assimilation, *in* 2013 SPE Reservoir Simulation Symposium, The Woodlands, Texas, USA: Society of Petroleum Engineers Journal, SPE 163675, doi:10.2118/163675-MS.

Evensen, G., 2021, Formulating the history matching problem with consistent error statistics: Computational Geosciences, v. 25, no. 3, p. 945–970, doi:10.1007/s10596-021-10032-7.

Evensen, G., 1994, Inverse Methods and Data Assimilation in Nonlinear Ocean Models: Physica D, in press, p. 23, doi:10.1016/0167-2789(94)90130-9.

Evensen, G., 2003, The Ensemble Kalman Filter: theoretical formulation and practical implementation: Ocean Dynamics, v. 53, no. 4, p. 343–367, doi:10.1007/s10236-003-0036-9.

Evensen, G., J. Hove, H. C. Meisingset, E. Reiso, K. S. Seim, and Ø. Espelid, 2007, Using the EnKF for Assisted History Matching of a North Sea Reservoir Model, *in* 2007 SPE Reservoir Simulation Symposium: Society of Petroleum Engineers Journal, SPE 106184.

Evensen, G., and P. J. van Leeuwen, 2000, An Ensemble Kalman Smoother for Nonlinear Dynamics: Monthly Weather Review Journal, American Meteorological Society, v. 128, no. 6, p. 1852–1867, doi:10.1175/1520-0493(2000)128<1852:AEKSFN>2.0.CO;2.

Gao, G., M. Zafari, and A. C. Reynolds, 2006, Quantifying Uncertainty for the PUNQ-S3 Problem in a Bayesian Setting With RML and EnKF: Society of Petroleum Engineers, 2006 SPE Journal, v. 11, no. 04, p. 506–515, doi:10.2118/93324-PA.

Gaspari, G., and S. E. Cohn, 1999, Construction of correlation functions in two and three dimensions: Quarterly Journal of the Royal Meteorological Society, v. 125, no. 554, p. 723–757, doi:10.1002/qj.49712555417.

Gu, Y., and D. S. Oliver, 2007, An Iterative Ensemble Kalman Filter for Multiphase Fluid Flow Data Assimilation: SPE Journal, v. 12, no. 04, p. 438–446, doi:10.2118/108438-PA.

Gu, Y., and D. S. Oliver, 2004, History Matching of the PUNQ-S3 Reservoir Model Using the Ensemble Kalman Filter: Society of Petroleum Engineers, 2005 SPE Journal, v. 10, no. 02, p. 217–224, doi:10.2118/89942-PA.

von Harten, J., M. de la Varga, M. Hillier, and F. Wellmann, 2021, Informed Local Smoothing in 3D Implicit Geological Modeling, 11: Minerals, v. 11, no. 11, p. 1281, doi:10.3390/min11111281.

Haugen, V., G. Nævdal, L.-J. Natvik, G. Evensen, A. M. Berg, and K. M. Flornes, 2008, History Matching Using the Ensemble Kalman Filter on a North Sea Field Case: SPE Journal, v. 13, no. 04, p. 382–391, doi:10.2118/102430-PA.

Houtekamer, P. L., and H. L. Mitchell, 2001, A Sequential Ensemble Kalman Filter for Atmospheric Data Assimilation: Monthly Weather Review Journal, American Meteorological Society, v. 129, no. 1, p. 123–137, doi:10.1175/1520-0493(2001)129<0123:ASEKFF>2.0.CO;2.

Luo, X., and T. Bhakta, 2019, Automatic and adaptive localization for ensemble-based history matching: Journal of Petroleum Science and Engineering, v. 184, p. 106559, doi:10.1016/j.petrol.2019.106559.

Luo, X., T. Bhakta, and G. Nævdal, 2017, Correlation-Based Adaptive Localization With Applications to Ensemble-Based 4D-Seismic History Matching: Society of Petroleum Engineers Journal, SPE 185936, v. 23, no. 02, p. 396–427, doi:10.2118/185936-PA.

Luo, X., R. J. Lorentzen, R. Valestrand, and G. Evensen, 2019, Correlation-Based Adaptive Localization for Ensemble-Based History Matching: Applied to the Norne Field Case Study: Society of Petroleum Engineers Journal, 2019 SPE reservoir evaluation & engineering, v. 22, no. 3, p. 1084–1109, doi:10.2118/191305-PA.

Nævdal, G., L. M. Johnsen, S. I. Aanonsen, and E. H. Vefring, 2003, Reservoir Monitoring and Continuous Model Updating Using Ensemble Kalman Filter: Society of Petroleum Engineers, 2005 SPE Journal, v. 10, no. 01, p. 66–74, doi:10.2118/84372-PA.

Nagle, N. N., 2010, Geostatistical Smoothing of Areal Data: Mapping Employment Density with Factorial Kriging.: Geographical Analysis, v. 42, no. 1, p. 99–117, doi:10.1111/j.1538-4632.2009.00784.x.

Products by Emerson E&P Software, n.d.: accessed December 6, 2021, https://pdgm.com/products/rms.

Sakov, P., and L. Bertino, 2010, Relation between two common localisation methods for the EnKF: 2011 Computational Geosciences Journal, v. 15, no. 2, p. 225–237, doi:10.1007/s10596-010-9202-6.

Silva Neto, G. M., R. V. Soares, G. Evensen, A. Davolio, and D. J. Schiozer, 2021, Subspace Ensemble Randomized Maximum Likelihood with Local Analysis for Time-Lapse-Seismic-Data Assimilation: Society of Petroleum Engineers, 2021 SPE Journal, v. 26, no. 02, p. 1011–1031, doi:10.2118/205029-PA.

Skjervheim, J. A., G. . Evensen, J. . Hove, and J. G. Vabø, 2011, An Ensemble Smoother for assisted History Matching, *in* 2011 SPE Reservoir Simulation Symposium, The Woodlands, Texas, USA: Society of Petroleum Engineers Journal, SPE 141929, doi:10.2118/141929-MS.

Welcome to ERT's documentation! — ERT 2.30.0rc1.dev46+g6ccfc183 documentation, n.d.: accessed December 6, 2021, https://ert.readthedocs.io/en/latest/.

Wen, X.-H., and W. H. Chen, 2005, Real-Time Reservoir Model Updating Using Ensemble Kalman Filter With Confirming Option: Society of Petroleum Engineers, 2006 SPE Journal, v. 11, no. 04, p. 431–442, doi:10.2118/92991-PA.

Whitaker, J. S., and T. M. Hamill, 2002, Ensemble Data Assimilation without Perturbed Observations: Monthly Weather Review Journal, American Meteorological Society, v. 130, no. 7, p. 1913–1924, doi:10.1175/1520-0493(2002)130<1913:EDAWPO>2.0.CO;2.

Zafari, M., and A. C. Reynolds, 2005, Assessing the Uncertainty in Reservoir Description and Performance Predictions With the Ensemble Kalman Filter: Society of Petroleum Engineers, 2007 SPE Journal, v. 12, no. 03, p. 382–391, doi:10.2118/95750-PA.

APPENDIX A

Initial ensemble coverage of observations

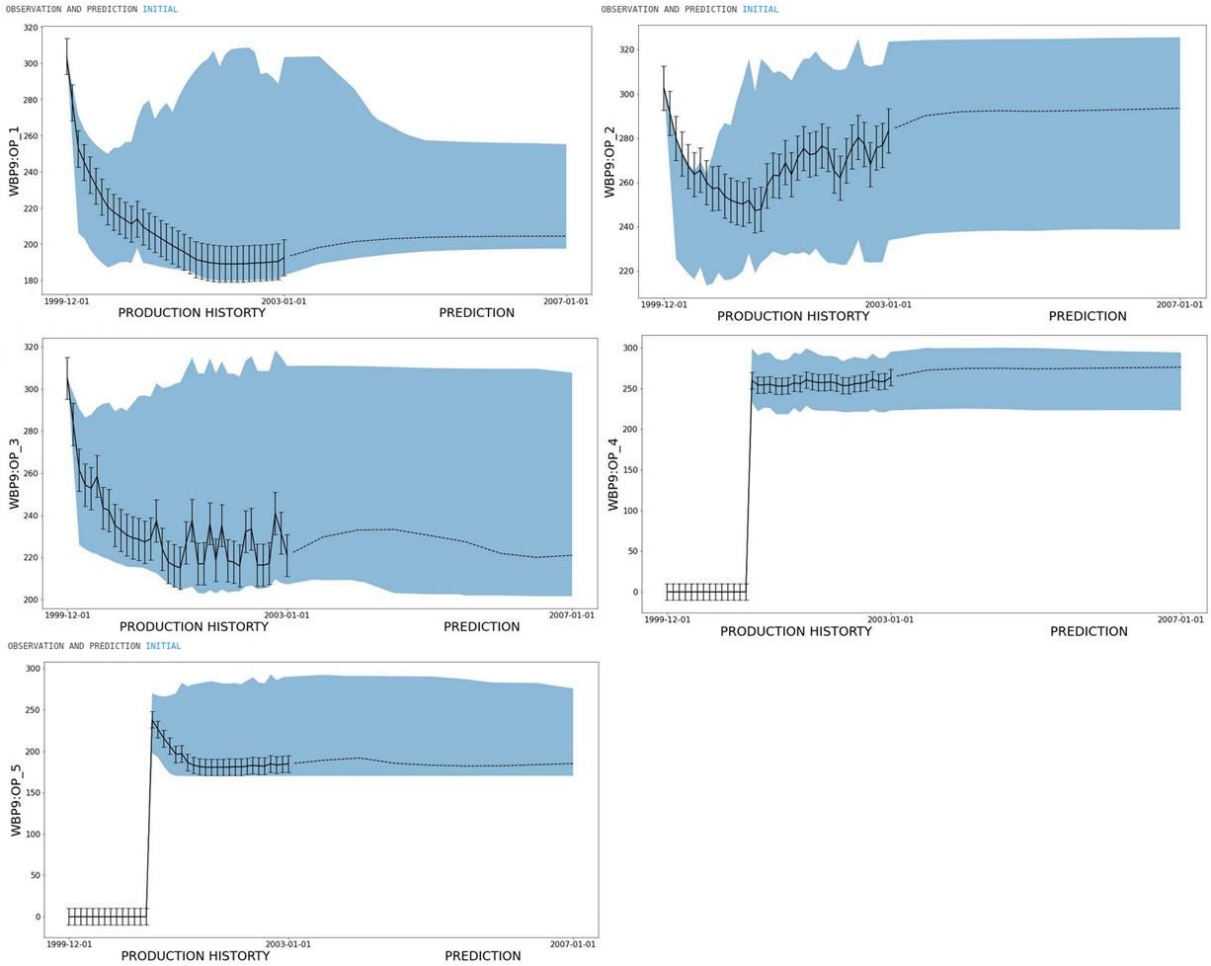

Fig. A- 1 Initial ensemble coverage of WBP9 observations for all producer wells.

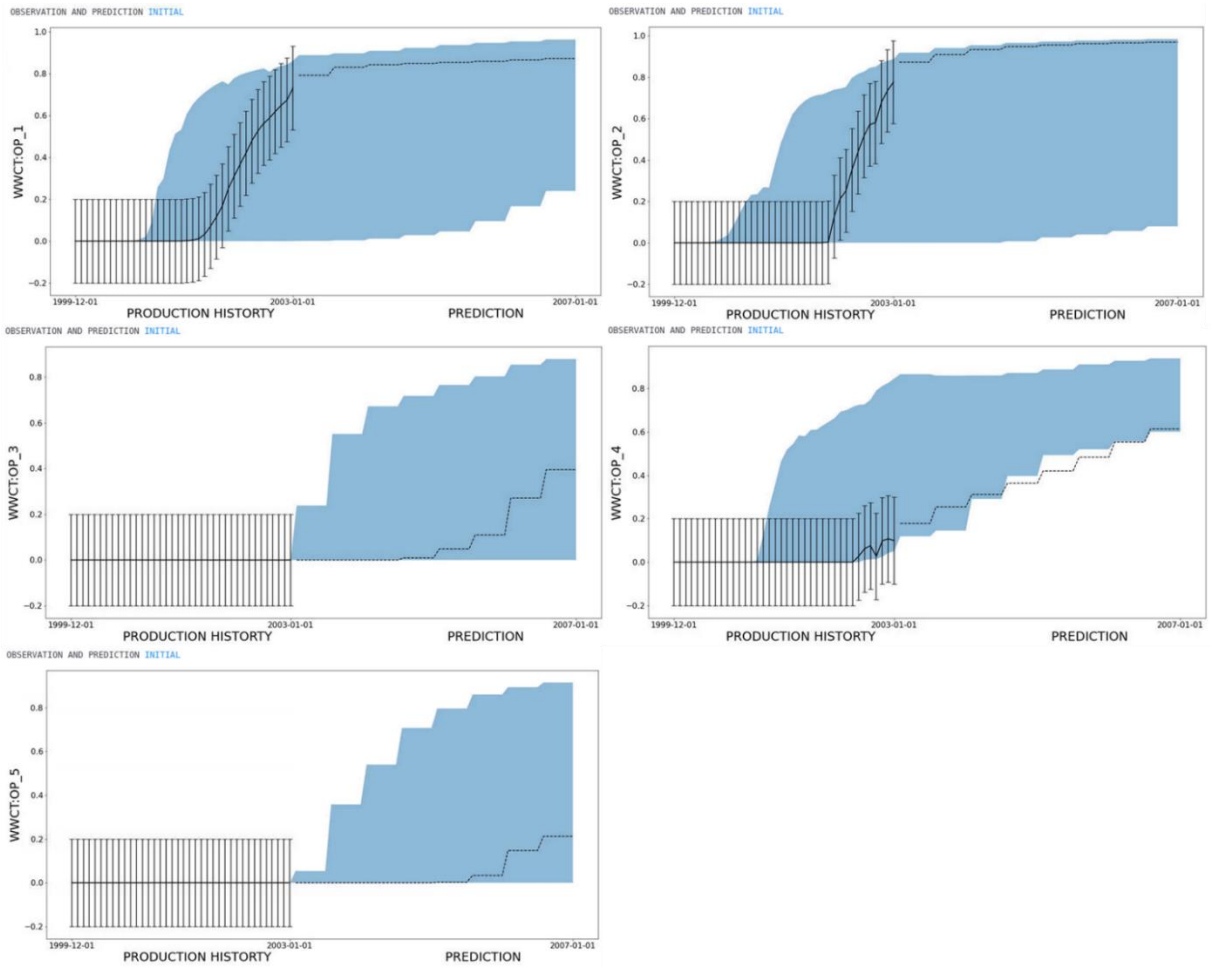

Fig. A- 2 Initial ensemble coverage of WWCT observations for all producer wells.

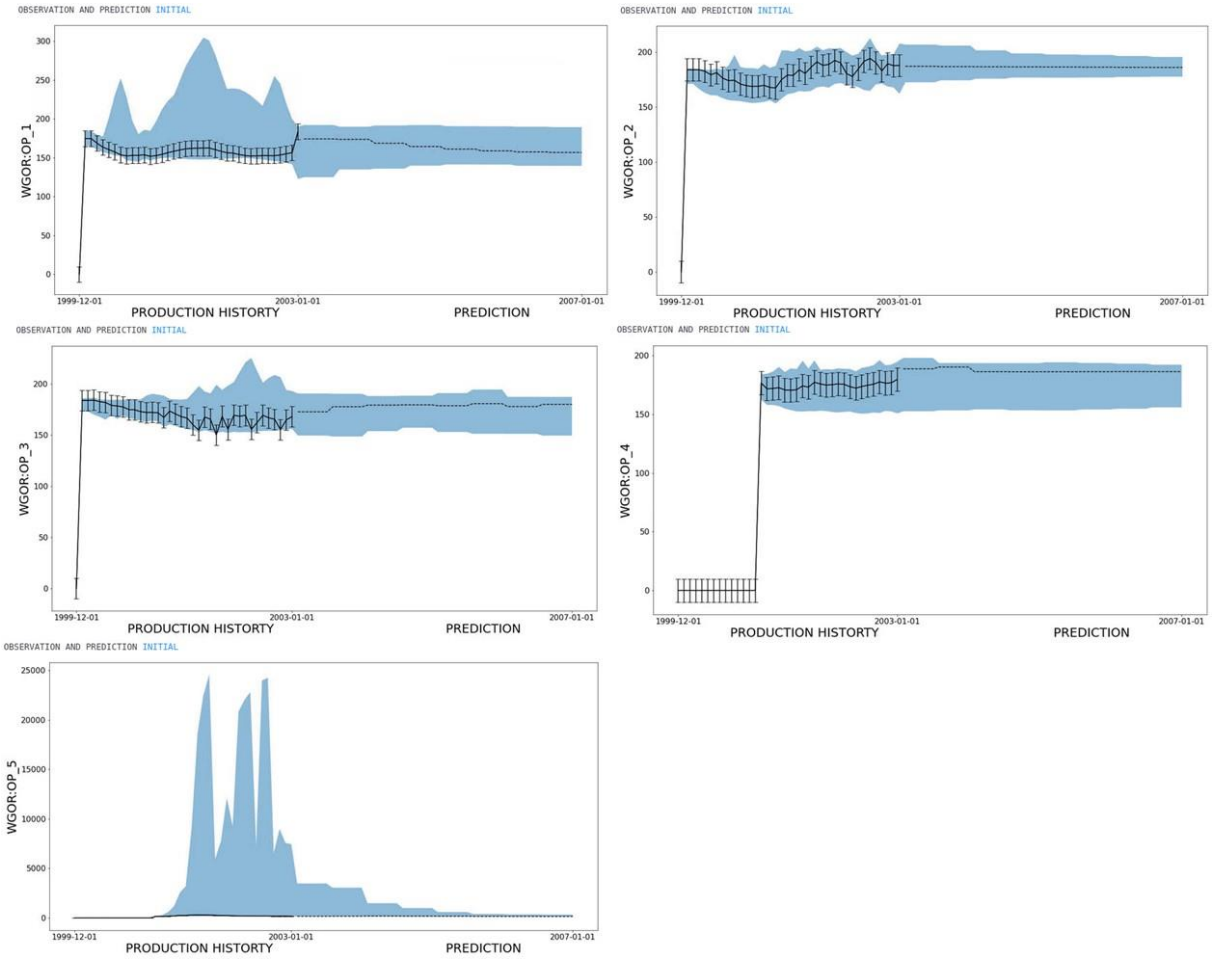

Fig. A- 3 Initial ensemble coverage of WGOR observations for all producer wells.

APPENDIX B

Updated benchmark ensemble coverage of observations

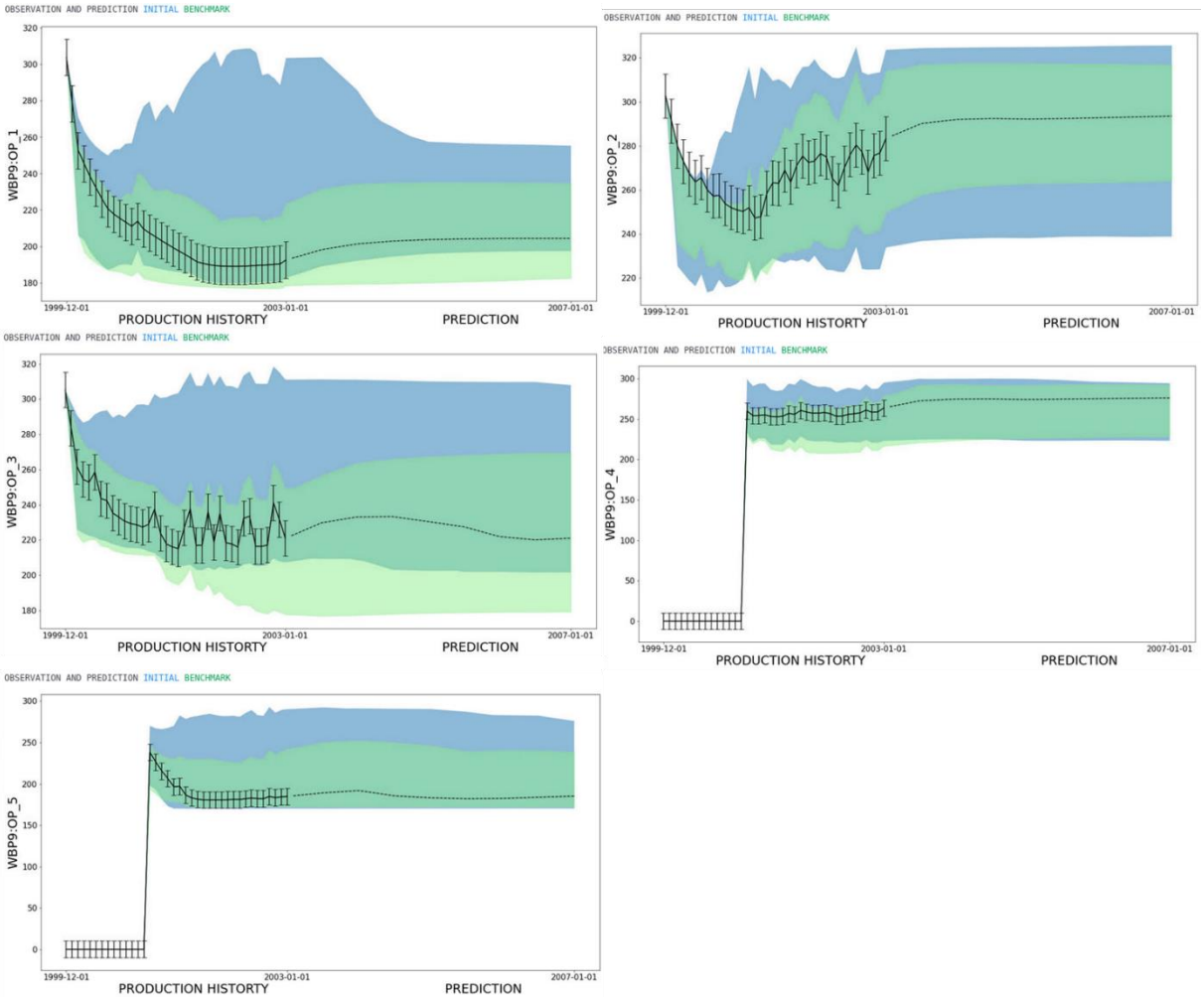

Fig. B- 1 Initial and updated benchmark ensemble coverage of WBP9 observations for all producer wells.

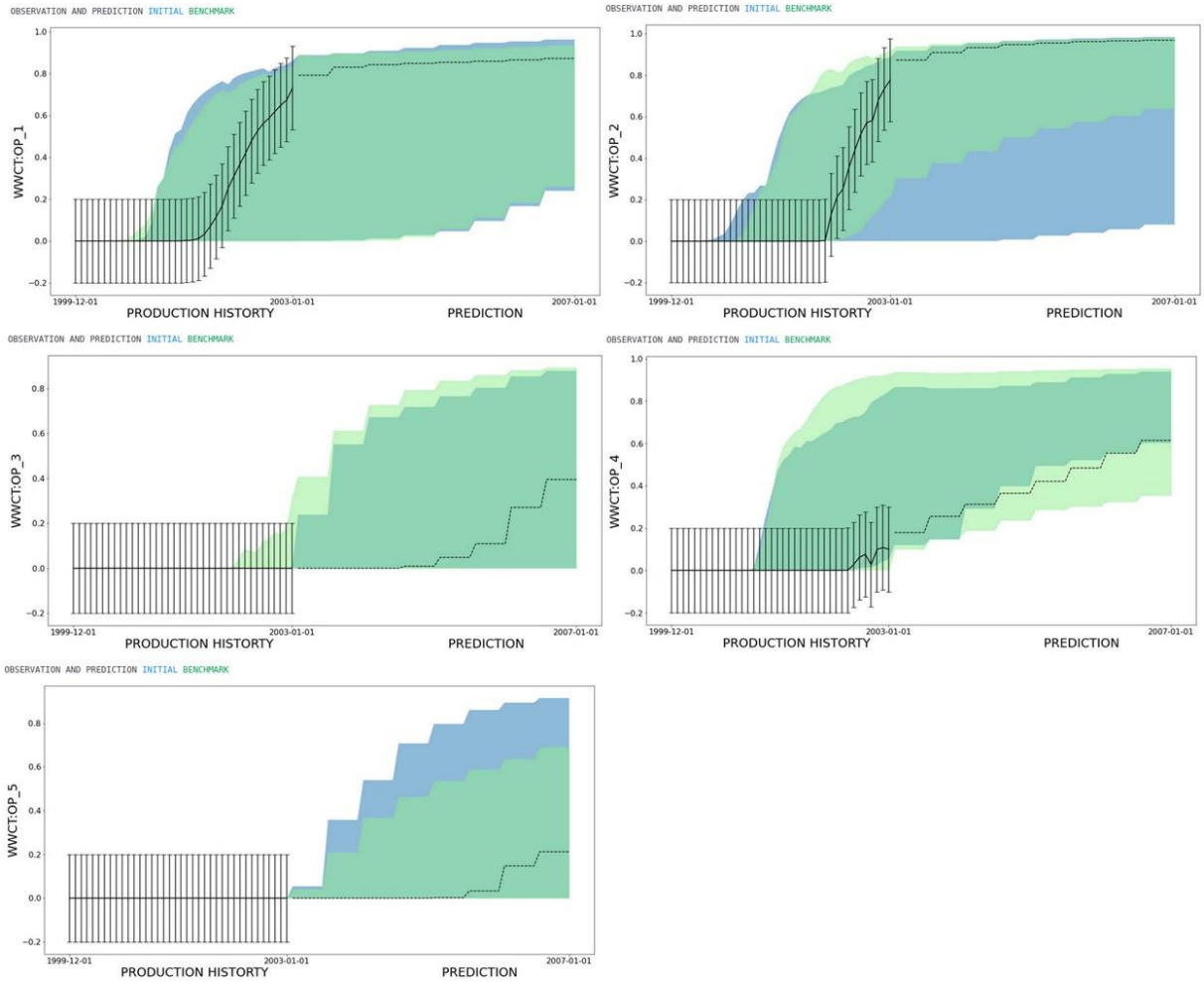

Fig. B- 2 Initial and updated benchmark ensemble coverage of WWCT observations for all producer wells.

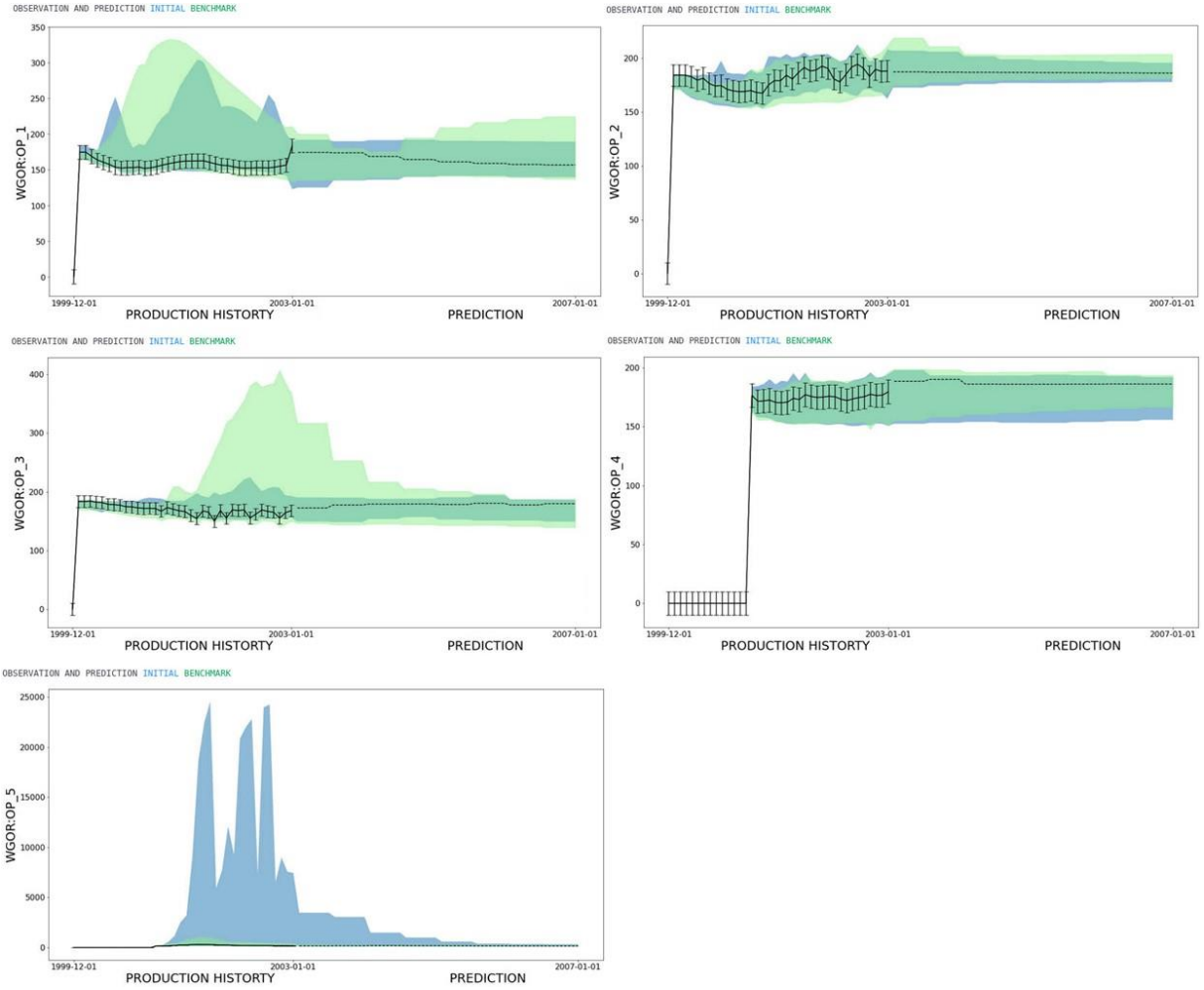

Fig. B- 3 Initial and updated benchmark ensemble coverage of WGOR observations for all producer wells.

APPENDIX C

Non-adaptive localization results

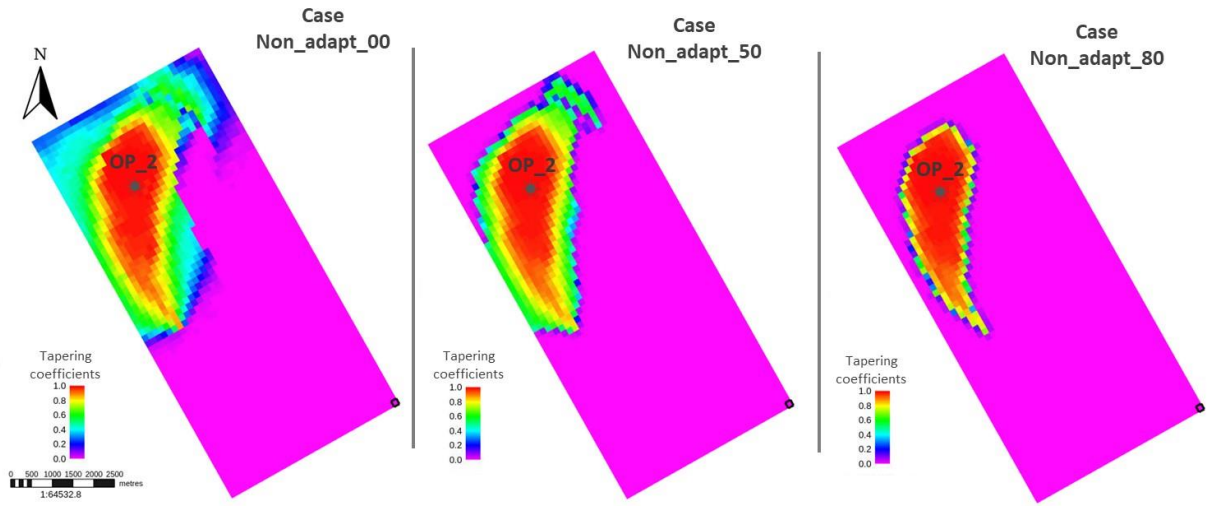

Fig. C- 1 OP_2 observation tapering coefficients for the three non-adaptive cases.

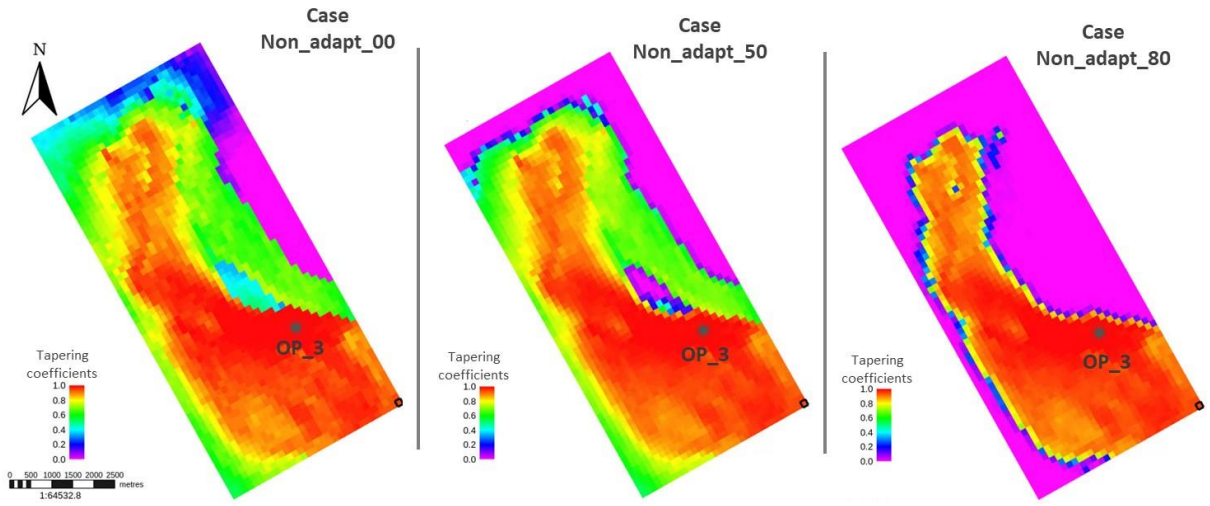

Fig. C- 2 OP_3 observation tapering coefficients for the three non-adaptive cases.

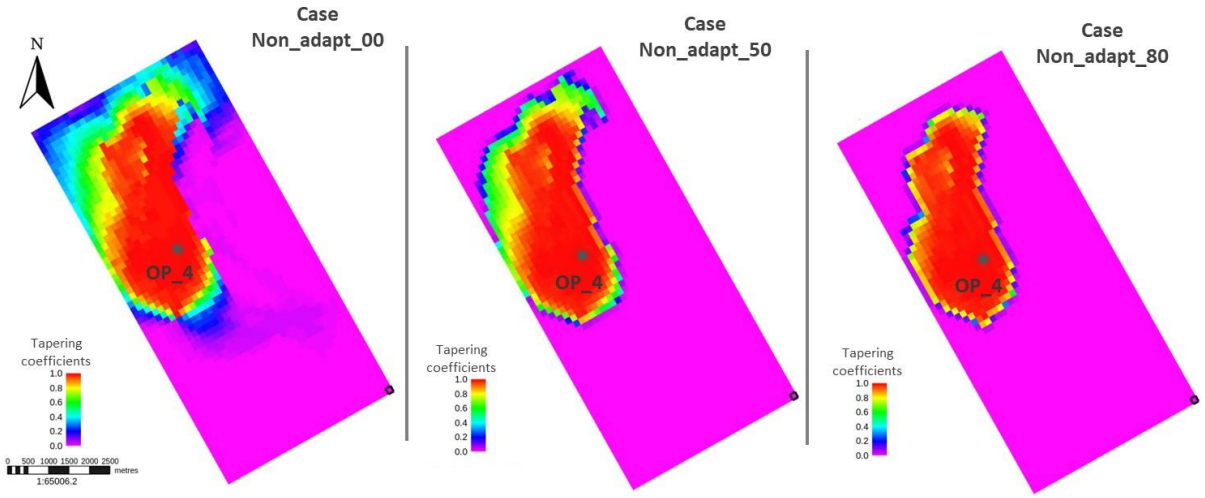

Fig. C- 3 OP_4 observation tapering coefficients for the three non-adaptive cases.

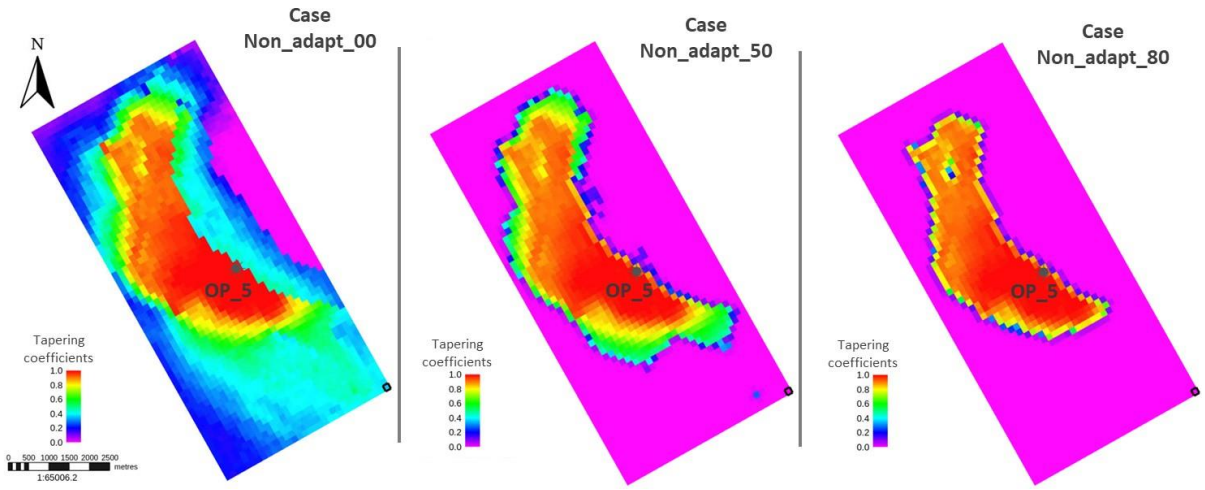

Fig. C- 4 OP_5 observation tapering coefficients for the three non-adaptive cases.

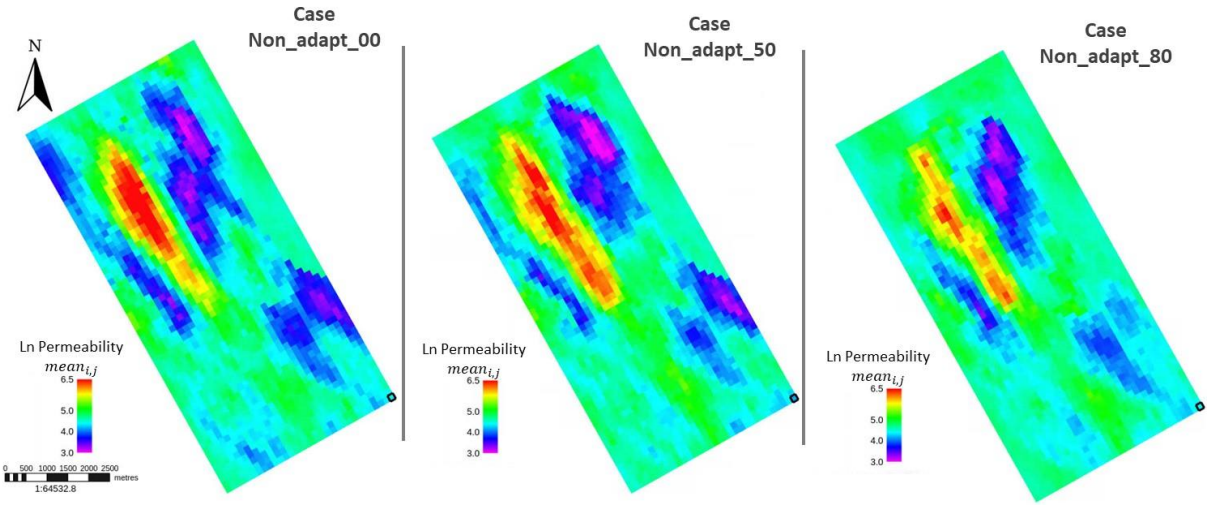

Fig. C- 5 Updated ensemble ln permeability mean for three non-adaptive cases.

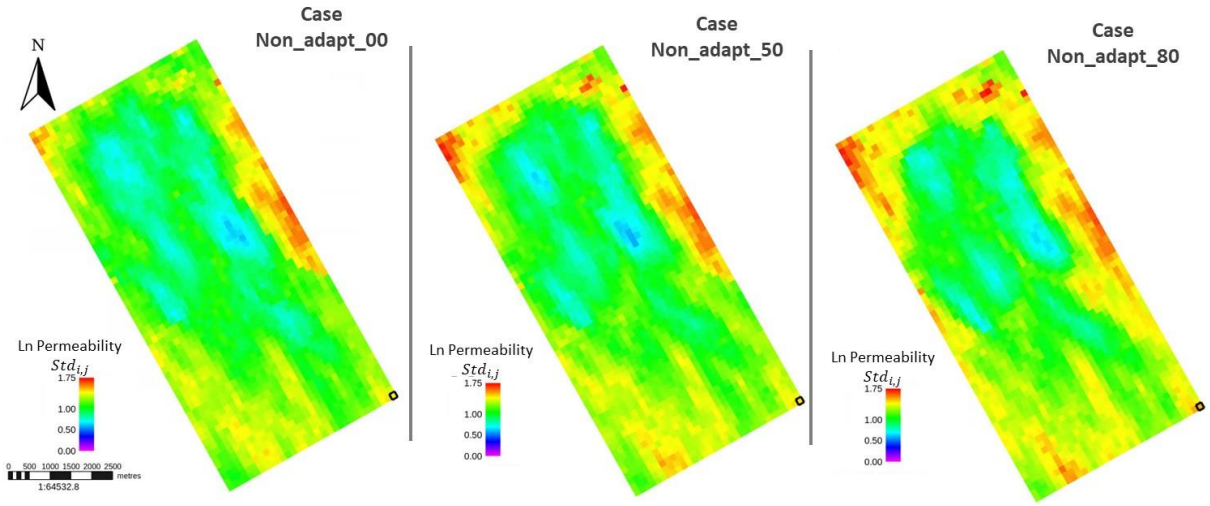

Fig. C- 6 Updated ensemble ln permeability standard deviation for three non-adaptive cases.

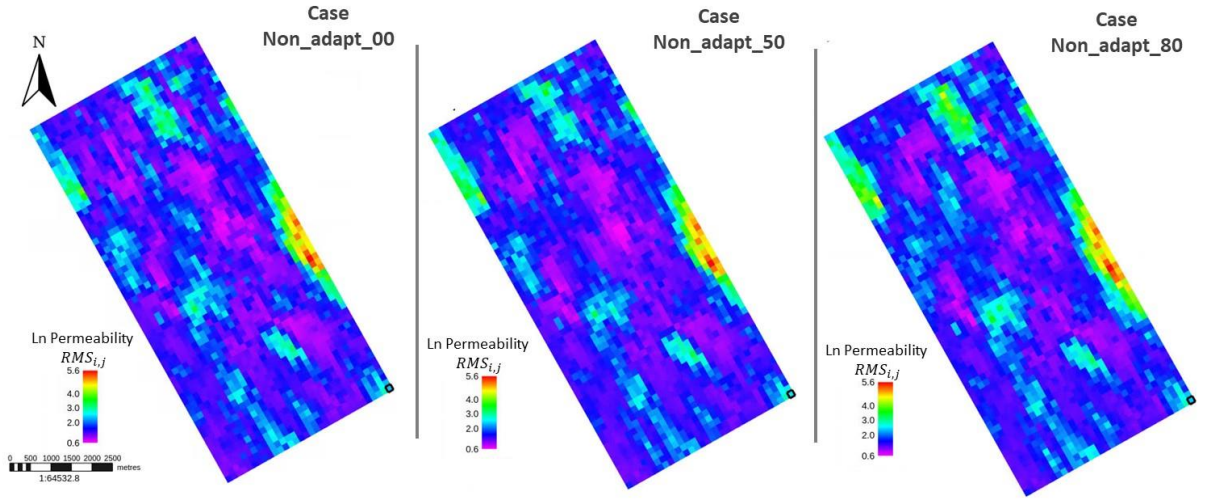

Fig. C- 7 Updated ensemble ln permeability RMS for three non-adaptive cases.

APPENDIX D

Adaptive localization results

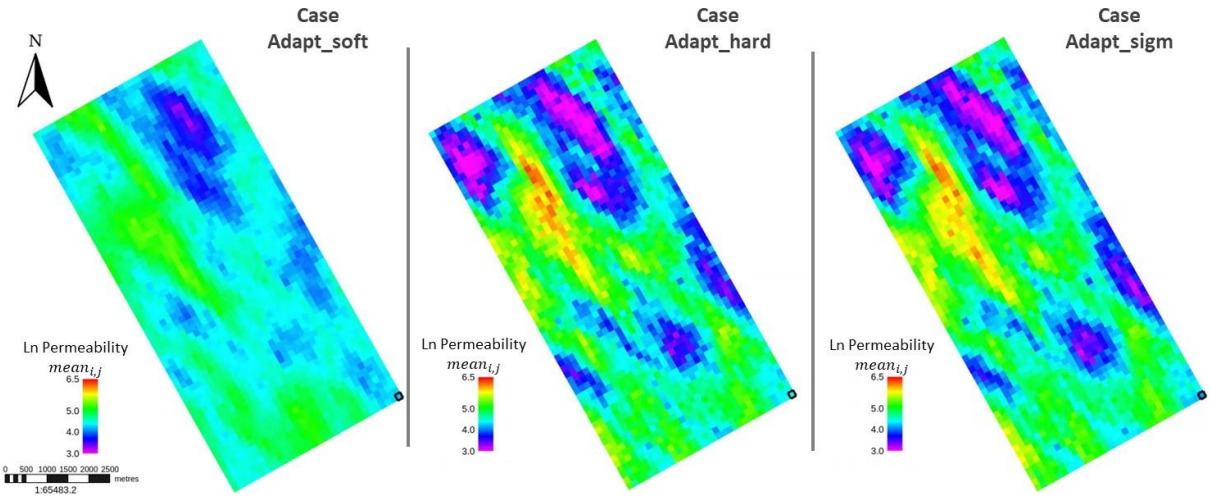

Fig. D- 1 Updated ensemble ln permeability mean for three adaptive cases.

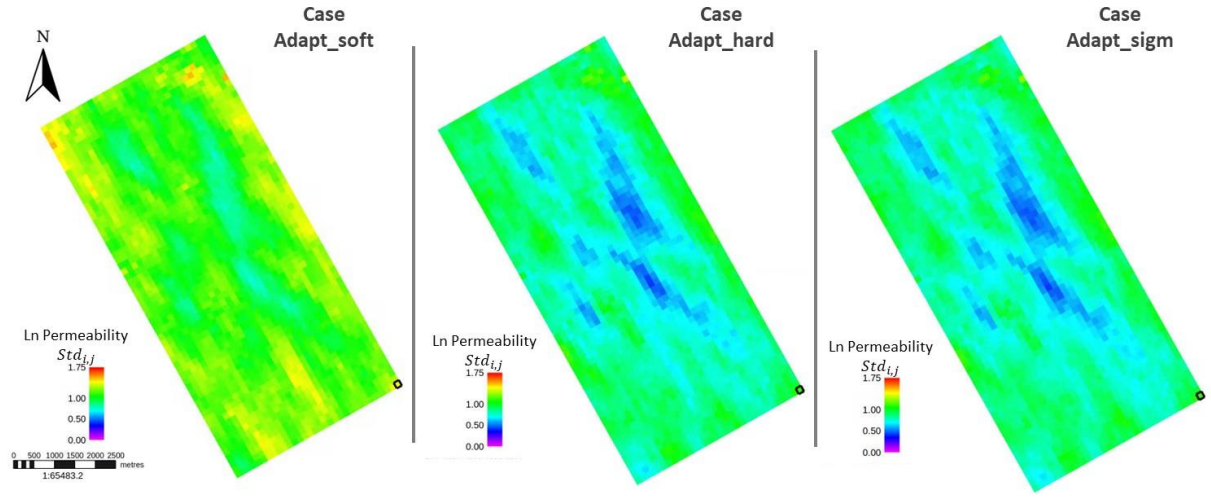

Fig. D- 2 Updated ensemble ln permeability standard deviation for three adaptive cases.

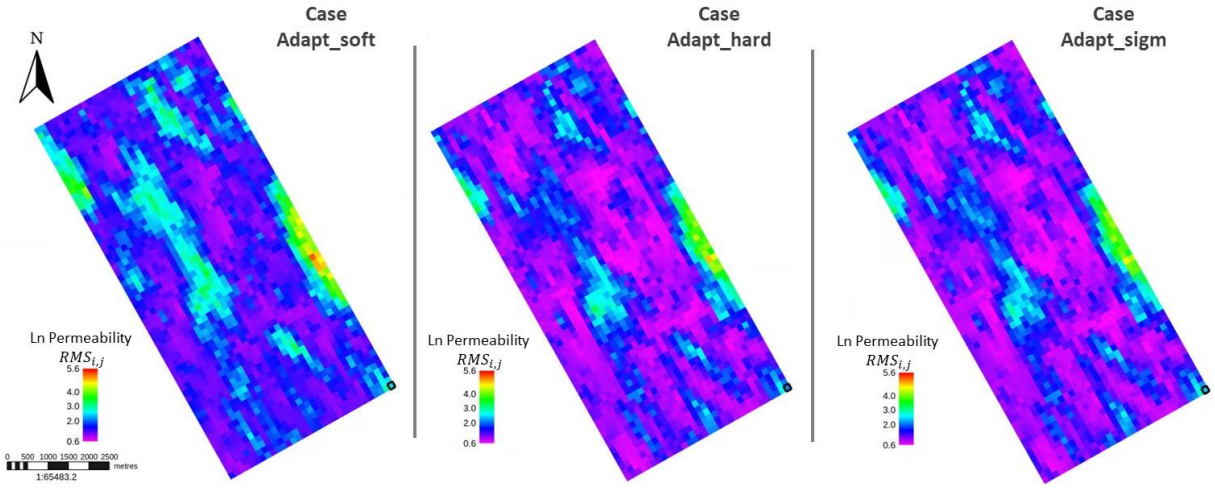

Fig. D- 3 Updated ensemble ln permeability RMS for three adaptive cases.

APPENDIX E

Comparative analysis among updated ensembles

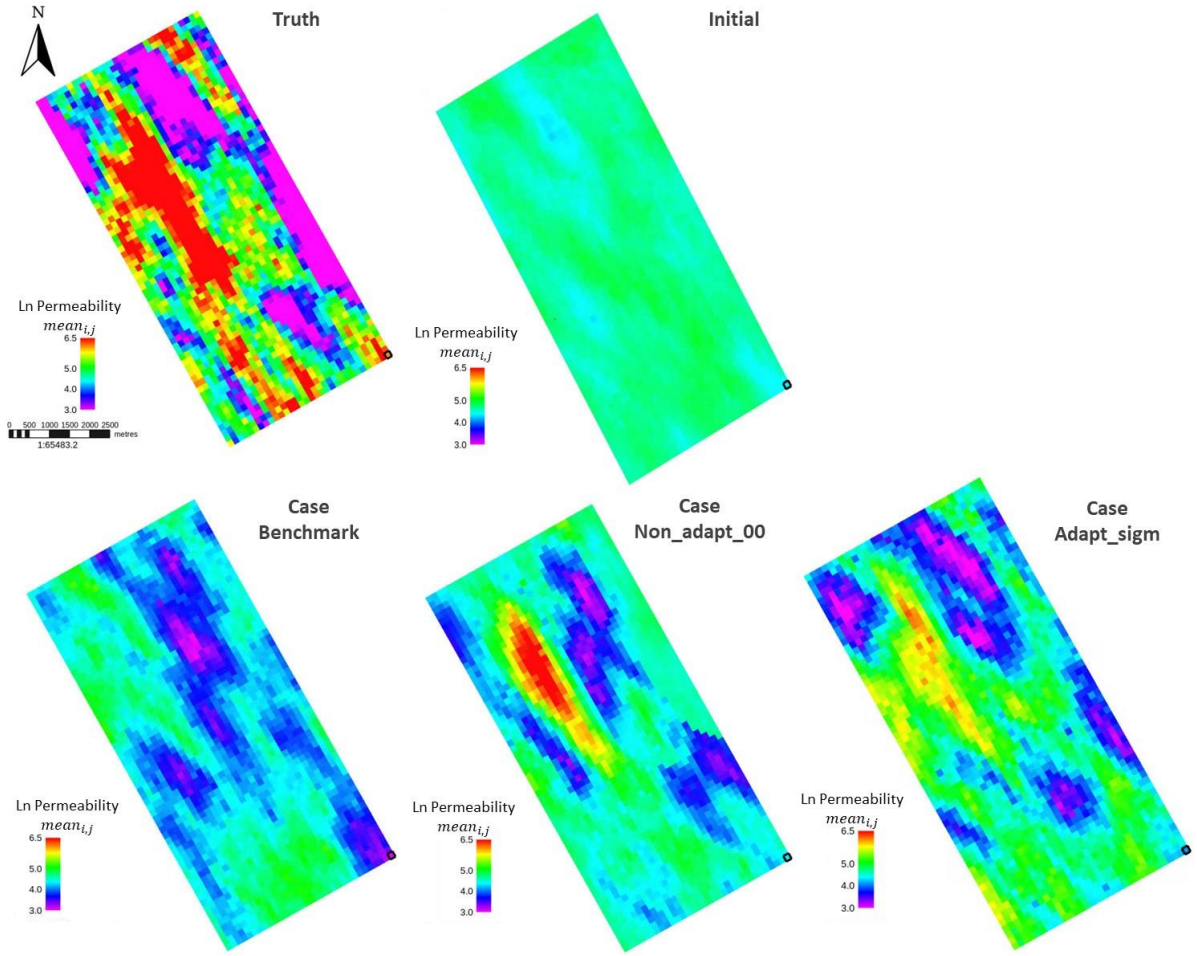

Fig. E- 1 Comparative analysis of the updated ensemble ln permeability mean.

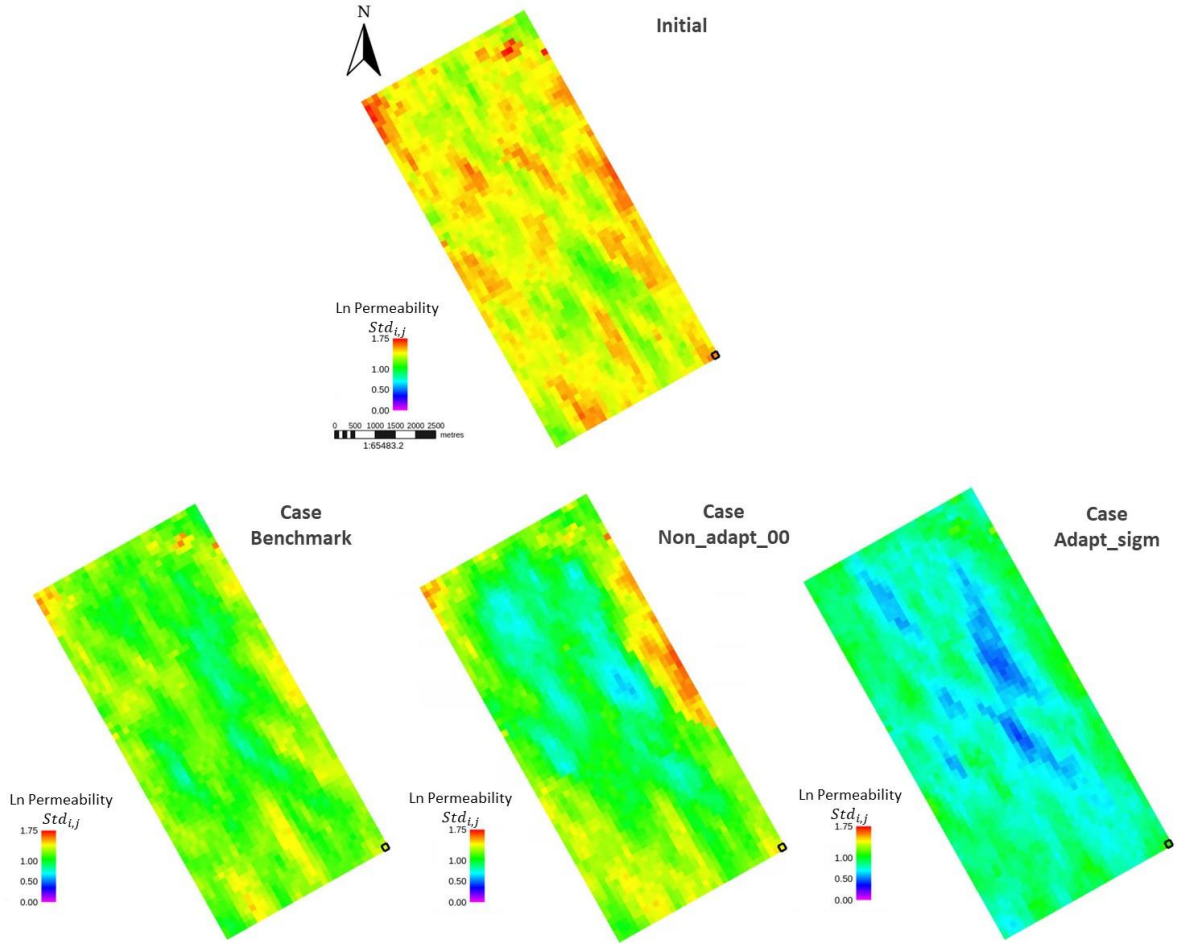

Fig. E- 2 Comparative analysis of the updated ensemble ln permeability standard deviation.

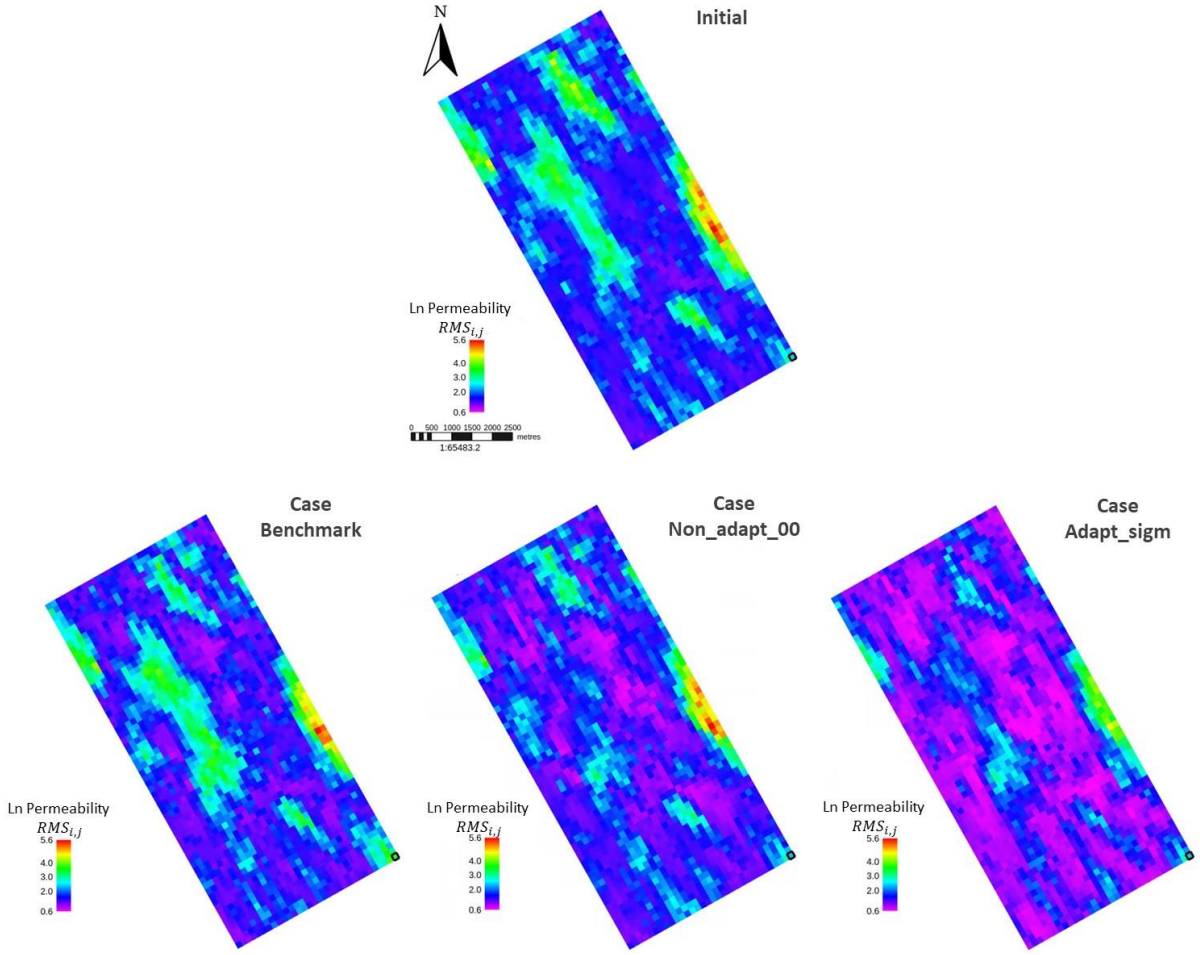

Fig. E- 3 Comparative analysis of the updated ensemble ln permeability RMS.

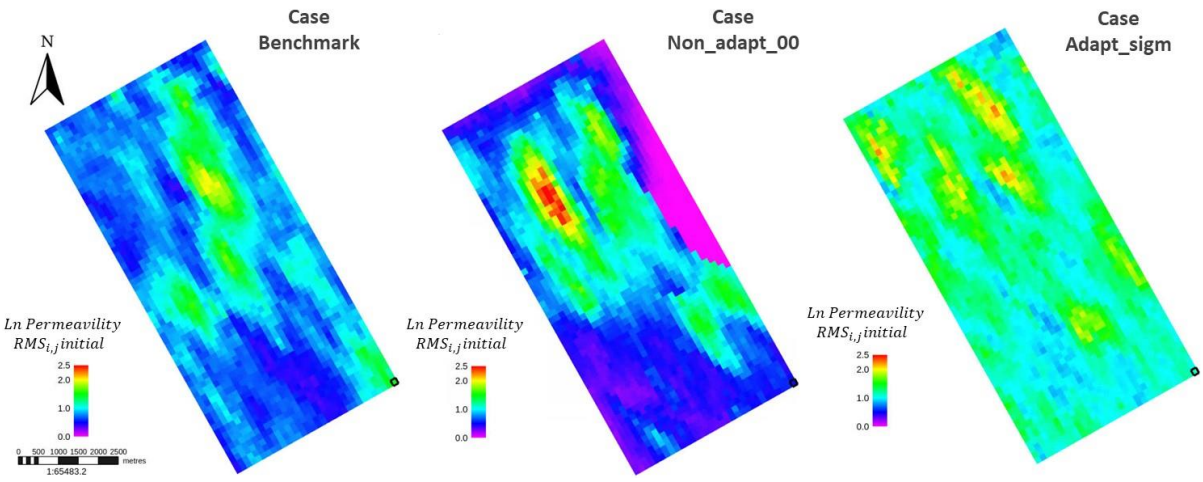

Fig. E- 4 Comparative analysis of the RMS between Initial and updated ensembles for ln permeability.

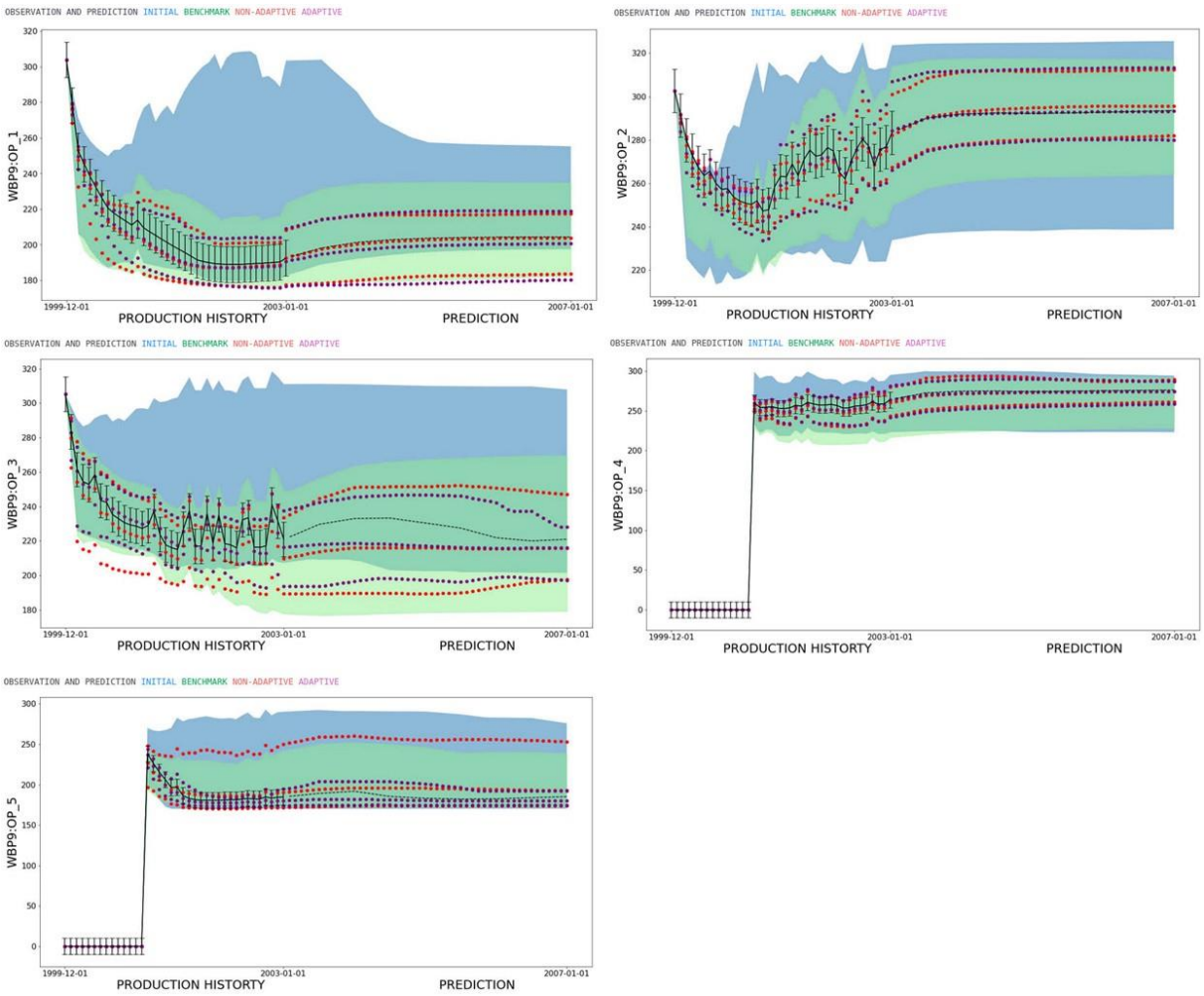

Fig. E- 5 Comparative analysis of initial and updated ensemble coverage over WBP9 observations

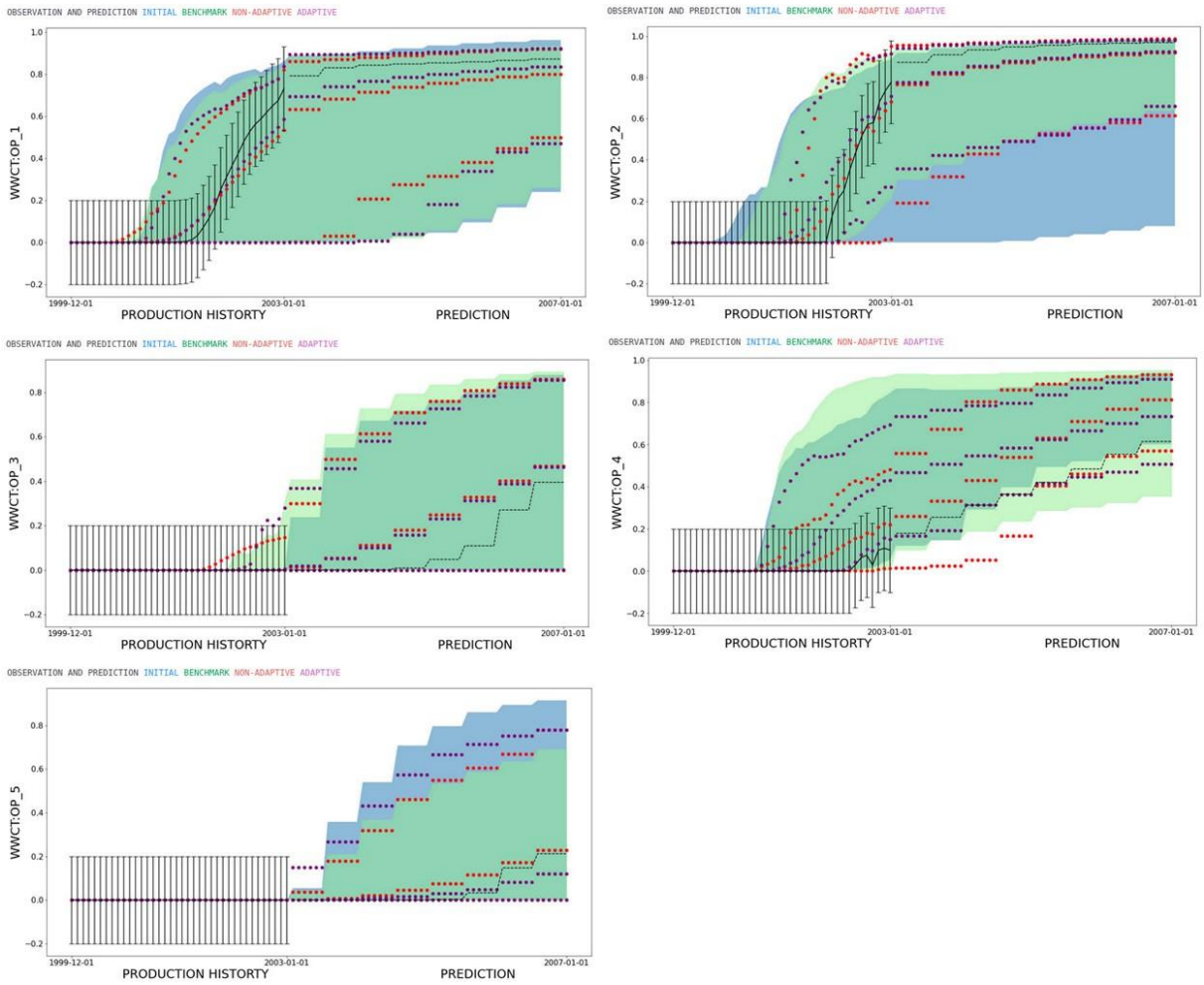

Fig. E- 6 Comparative analysis of initial and updated ensemble coverage over WWCT observations

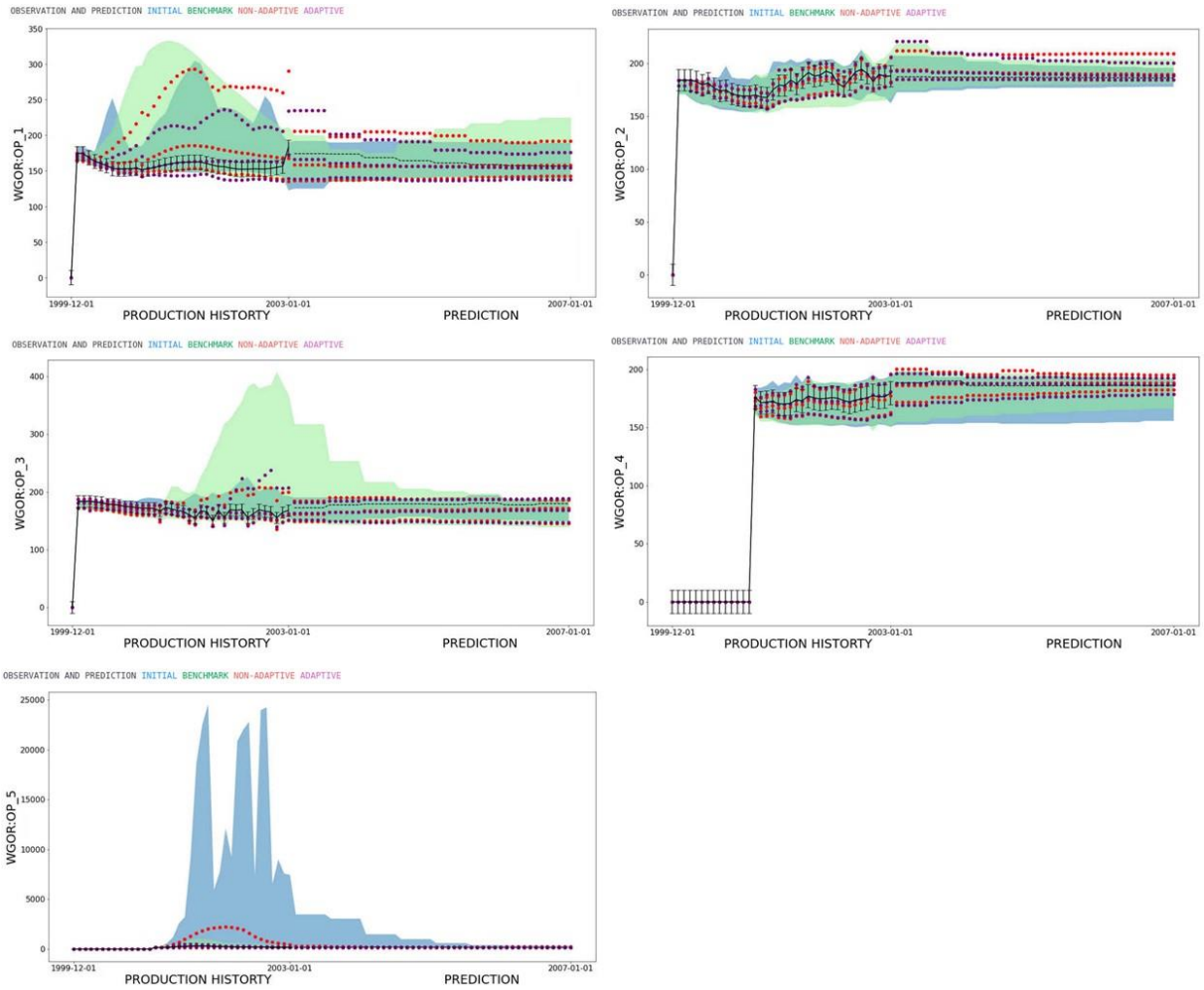

Fig. E- 7 Comparative analysis of initial and updated ensemble coverage over WWGOR observations.